Application of biowaste and nature-inspired (nano) materials in fuel cells

Babak Jaleh, *[a] Atefeh Nasri, [a] Mahtab Eslamipanah, [a] Mahmoud Nasrollahzadeh, *[b] Jacky H. Advani, [c] Paolo Fornasiero [d] and Manoj B. Gawande *[e]

Industrialization and the increasing amount of by-products and residues released from industrial activities have triggered an urgent demand for the development of clean energy storage and conversion systems to eradicate or minimize the use of environmentally noxious matter. In this case, nature-inspired materials present significant potential as catalysts and nanofillers for the preparation of electrodes and nanocomposites for energy storage and conversion. These materials possess extended porous architectures, high surface areas, considerable mechanical and thermal stability, abundant reserves, and low cost. In this review, we summarize the structure and classification of natural materials that make them appropriate for application in energy storage and conversion devices. Furthermore, we focus on the applications and new advancements of nature-inspired materials in fuel cells, given that they enhance the performance of fuel cell technology.

1. Introduction

Science and technology are fundamental to guarantee sustainable development and constant improvement in the quality of life. In this respect, industrialization is desirable but it is commonly accompanied by high-energy consumption and severe environmental deterioration. The deleterious impact of pollution on the atmosphere and earth, arising from by-products of industrial activities, is the main problem currently faced by society. Therefore, it is urgent to develop clean and long-lasting energies such as solar, wind, and tidal energies. However, stable and effective energy storage and conversion systems need to be developed to overcome the issues and difficulties associated with the use of these renewable energies. In this case, secondary batteries, supercapacitors, solar panels, and fuel cells are potent technologies that can be successfully utilized for energy storage and conversion of renewable energy sources. Furthermore, fuel cells can play a significant role in the production of pollutant-free energy sources.

In the 19th century, studies on fuel cells and the direct conversion of fossil fuel chemical energy into electrical energy began.[1] Fuel cells have been described as one of the most capable clean energy technologies, which provide all the essentials for energy security and environmental sustainability, and have been considered as a conceivable replacement for power generation systems.[2] Notably, fuel cells generate electrical energy directly from the chemical energy of the input fuels (hydrogen, hydrocarbons, and oxygen) *via* redox reactions and do not require recharging. The functionality of fuel cells can be utilized in several applications such as medical devices, tissue engineering, stationary, and transportation.[3] The operation of fuel cells is similar to that of electrochemical batteries, with the only difference being that the chemical energy of the former is stored outside the cell, while it is stored in the cell in the latter. The main components of energy storage systems are electrodes, electrolytes, and separators. Eco-friendly fuel cells are classified with respect to the type of fuel and electrolyte used in hydrogen/hydrocarbon fuel cells. The hydrogen fuel cells include PEMFCs, AFCs, and PAFCs. DMFCs, DEFCs, and DFAFCs are included in hydrocarbon fuel cells. SOFCs and MCFCs can operate with both hydrogen and hydrocarbon fuels. Biofuel cells, namely MFCs and EFCs, are also attractive and considerable eco-friendly fuel cells.[4–7] This classification is presented in Fig. 1.

Despite the high conductivity of conventional liquid electrolytes, the risk of their permeance and corrosion cannot be ignored. There are safety concerns about electrical systems and

[a]*Department of Physics, Faculty of Science, Bu-Ali Sina University, 65174, Hamedan, Iran. E-mail: jaleh@basu.ac.ir*

[b]*Department of Chemistry, Faculty of Science, University of Qom, Qom 3716146611, Iran. E-mail: mahmoudnasr81@gmail.com*

[c]*Nanotechnology Centre, CEET, VŠB-Technical University of Ostrava, 17 Listopadu 2172/15, Ostrava-Poruba 708 00, Czech Republic*

[d]*Department of Chemical and Pharmaceutical Sciences, Center for Energy, Environment and Transport Giacomo Ciamician, INSTM Trieste Research Unit and ICCOM-CNR Trieste Research Unit, University of Trieste, via L. Giorgieri 1, I-34127, Trieste, Italy*

[e]*Department of Industrial and Engineering Chemistry, Institute of Chemical Technology, Mumbai-Marathwada Campus, Jalna 431203, Maharashtra, India. E-mail: mb.gawande@marj.ictmumbai.edu.in; mbgawande@gmail.com*

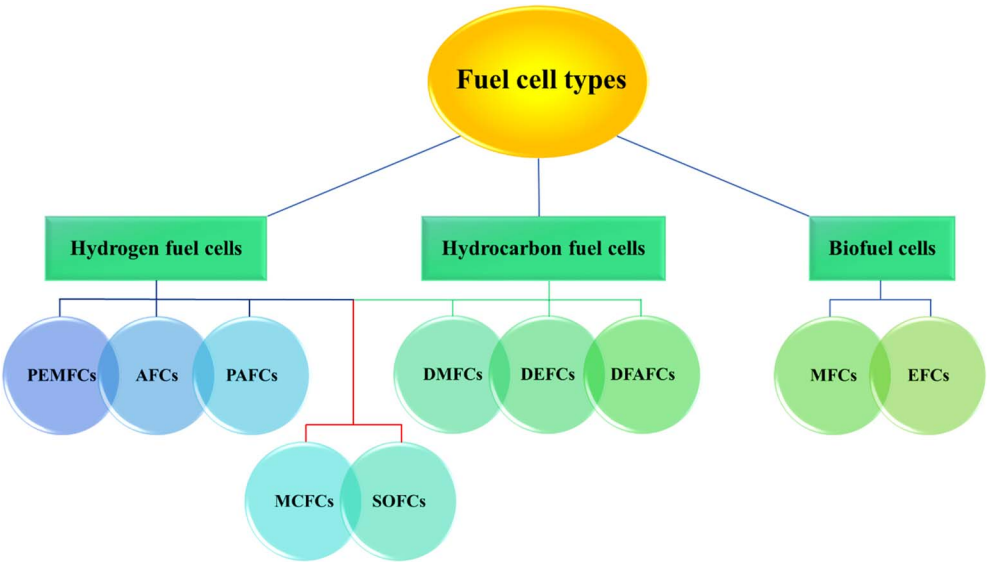

Fig. 1 Presentation of fuel cell types.

their short-circuiting and the possiblility of skin contact with liquid electrolytes. Thus, to overcome the issues associated with liquid electrolytes, solid-state and gel-type polymeric electrolytes have been developed.[8–10] One of the main benefits of the PEM is that it controls the water, which is a challenge for polymeric electrolyte membranes because the final products are liquid and the ensuing water makes the electrolyte flow. The generated water in the electrode declines the desired surface to separate hydrogen or stabilize the water. Thus, the generated water in the cathode should be controlled by the methods of retention or elimination. Also, there is a probability of water permeation in the anode due to the fact that the electrodes are thin, which can be desirable if its exact value is maintained.[11] Furthermore, the development of electrocatalysts has attracted significant interest owing to their effects on the functionality and average life of fuel cells by the acceleration of the electrochemical reaction kinetics at the electrode–electrolyte interface.[12]

Due to the vast energy applications, there is a high demand for energy, and hence it is important to boost the preparation of cost-effective, abundant, and efficient materials.[13,14] In the last few decades, nature-inspired materials have been considerably used as renewable, nontoxic, and risk-free sources in research and industrial activities to synthesize inexpensive and environment-friendly nanocomposites and nanocatalytic systems.[15] Natural materials are a good option for the stabilization of NPs, and consequently the preparation of catalytic structure.[16–19] Furthermore, they can be incorporated in polymers to improve the combustibility, mechanical and chemical properties, hydrophilicity, and ionic conductivity of polymeric nanocomposites as fillers. Simultaneously, the improvement in these properties can have a relevant impact on materials that are highly desirable in industry.

Nature-inspired materials have displayed remarkable examples of utilization efficiency in energy storage and conversion based on their improved electrochemical properties. Herein, we review the literature focusing on the application of nature-based materials to improve the performance of fuel cell technologies in the last two decades. In the second section, the working principles of different types of fuel cells utilizing nature-inspired materials are described. The features of nature-based materials are explained in the third section, and the application of nature-based materials in fuel cell systems is discussed in detail. Finally, in the last section, the current challenges and anticipated future outlooks are discussed. Given that these affordable natural materials exhibit unique features, namely, high specific surface area, porous structure, and biocompatibility, their effects on the performance of fuel cells were studied to overcome the challenges associated with the well-known Pt/carbon catalysts. In addition, the effect of nature-based material-supported, low-cost metallic compounds and modified natural materials on the efficiency of fuel cells is evaluated and compared with that of common Pt/carbon compounds. This review aims to provide a perspective on nature-based clean energy materials.

2. Fuel cell types and mechanisms

2.1 PEMFCs

One of the most powerful fuel cells is PEMFCs, which are extensively used, lightweight, well-set, and economically manufactured.[20] PEMFCs with a flexible electrolyte operate almost at low temperatures with high outputs and 40% to 50% efficiency, which make them appropriate for use at homes and in vehicles.[21–23] However, the disadvantages of this type of fuel cell include their intolerance to CO in impure H_2 and high cost.[22] The components of the typical PEMFCs and their working principle are schematically presented in Fig. 2. An MEA, which is made of advanced thin plastic, is set at the core of the fuel cell, between two anode and cathode electrodes as a PEM to

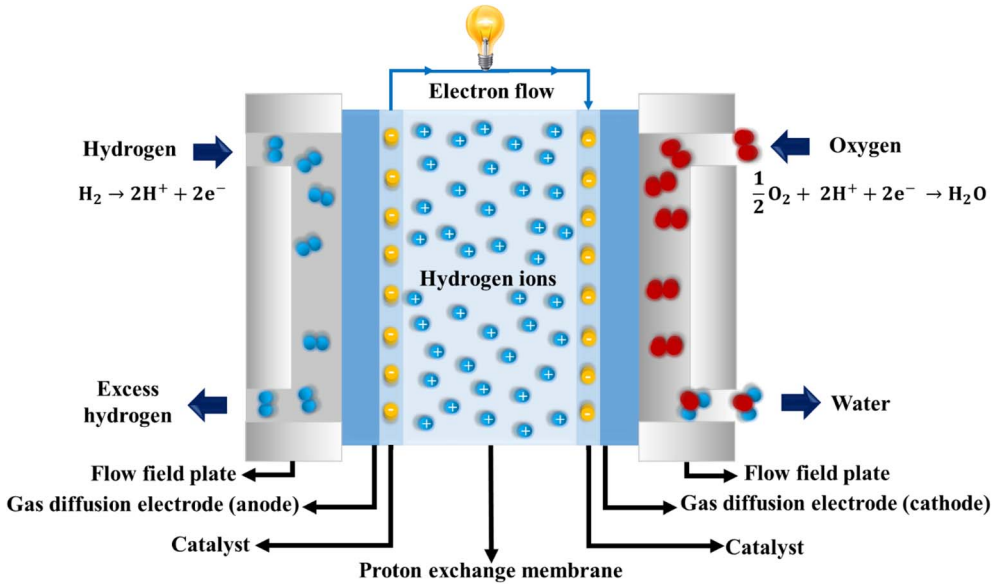

Fig. 2 Schematic representation of the working principle of PEMFCs. Modified from ref. 27.

exchange protons from the anode to the cathode by separating the fuel (hydrogen) from the oxidant (oxygen). Generally, a Pt catalyst is utilized on both sides of the membrane as an electrode, accelerating the reaction.[24,25] In PEMFCs, the HOR happens electrochemically on the anode, conforming to eqn (1). PEMs conduct hydrogen ions towards the cathode and prevent the transition of electrons and heavier gases between electrodes or catalyst layers. The electrons transfer from the anode to the cathode by an external electric circuit and provide electrical energy. The electrochemical ORR happens on the cathode electrode (eqn (2)) to combine oxygen with hydrogen ions, generating water and heat.[26–30]

$$H_2 \rightarrow 2H^+ + 2e^- \text{ (anode reaction)} \quad (1)$$

$$\tfrac{1}{2}O_2 + 2H^+ + 2e^- \rightarrow H_2O \text{ (cathode reaction)} \quad (2)$$

$$H_2 + \tfrac{1}{2}O_2 \rightarrow H_2O \text{ (overall cell reaction)} \quad (3)$$

The catalyst is commonly supported by high-surface area carbons such as porous carbon and hollow graphitic particles. Carbon-based Pt catalysts are mostly used for PEMFCs due to the best electrocatalytic performance of Pt in the ORR at the cathode and HOR at the anode.[25] However, the high cost of PEMFCs containing Pt make their commercialization challenging. Alternatively, Nafion is the most reported membrane material to be used as a PEM due to its proton conductivity, cation selectivity, excellent chemical stability, and mechanical strength. However, it is expensive to produce and has limitations such as being environmentally unfriendly, permeable, and requiring a high operating temperature. Also, the fuel efficiency is decreased by the crossover of the hydrogen from the anode to the cathode, reducing the fuel cell OCV. Besides, Nafion restricts the operation of PEMFCs at low temperatures because it requires hydration and permanent gas humidification to guarantee high proton conductivity. The water affinity and mechanical stability of Nafion is diminished at temperatures over 100 °C.[24] Presently, the commercialization of PEMFCs is close to being realized owing to the effective research effort using eco-friendly and cost-effective materials.

2.2 DMFCs

The comparative ease of methanol (CH_3OH) oxidation at the anode to release electrons and protons makes it an appealing fuel for the fuel cell technologies. DMFCs, a type of PEMFC with liquid fuel, are more beneficial than PEMFCs due their greater accessibility, lower cost, easy storage, low operating temperature (25–40 °C), no requirement of humidification equipment, high power density, and simple design without a separate hydrogen production system.[31–33] However, fuel crossover and poisonous byproducts are the two disadvantages of DMFCs. This type of fuel cell is appropriate for vehicles and small portable devices.[22] DMFCs operate by reforming and oxidizing a solution of water and methanol at the anode (MOR) to release electrons and protons and the ORR at the cathode, at low temperatures. The reactions are as follows:[34,35]

$$CH_3OH + H_2O \rightarrow CO_2 + 6H^+ + 6e^- \text{ (anode reaction)} \quad (4)$$

$$\tfrac{3}{2}O_2 + 6H^+ + 6e^- \rightarrow 3H_2O \text{ (cathode reaction)} \quad (5)$$

$$CH_3OH + \tfrac{3}{2}O_2 \rightarrow CO_2 + 2H_2O \text{ (overall cell reaction)} \quad (6)$$

The working principle of DMFCs is schematically shown in Fig. 3. The membrane and the electrocatalyst are two key components that affect the performance of DMFCs. In addition, they are associated with the main challenges of the DMFCs, namely, fuel crossover and slow anode kinetics. These challenges can be addressed by developing new membranes and

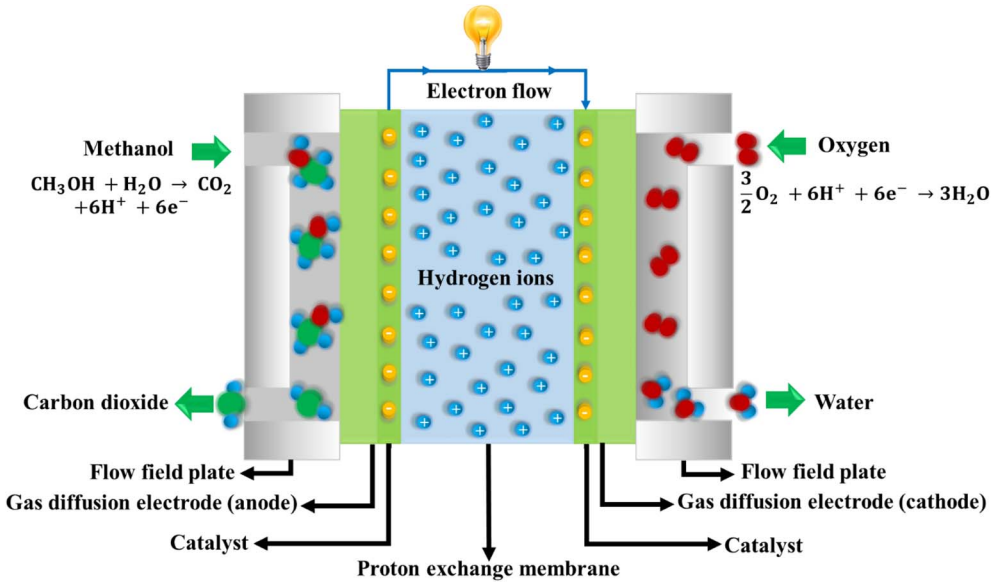

Fig. 3 Schematic representation of the working principle of DMFCs. Modified from ref. 35.

new catalysts. Fuel crossover is a serious problem in DMFCs given that methanol is readily transferred together with the solvent protons through the membrane, causing a decline in the fuel cell performance. Also, key problems such as activity, durability, and cost-effectiveness of the catalysts motivate the researchers to fabricate new membranes with high proton conductivity and low methanol permeability at high operating temperatures and catalysts with high potential efficiency using natural materials.

2.3 DEFCs

DEFCs operate *via* identical principles to DMFCs with a similar cell system with the only difference being the type of fuel source used in these fuel cells. Specifically, they utilize the less toxic and cheaper ethanol (C_2H_5OH) as fuel instead of methanol. Theoretically, the energy density generated by a DEFC is higher than that of DMFCs.[36–38] In DEFCs, ethanol is converted to CO_2 by the oxidation reaction with the generation of 12 electrons per complete reaction, which is twice that generated in DMFCs. However, DEFCs suffer from some problems related to the complete oxidation of C_2H_5OH to CO_2 and demonstrate a lower complete oxidation reaction rate in comparison with DMFCs. The C–C bonds cannot be simply broken at low temperatures.[36,39] The reactions that occur in a DEFC are described as follows:[40]

$$C_2H_5OH + 3H_2O \rightarrow 2CO_2 + 12H^+ + 12e^- \text{ (anode reaction)} \quad (7)$$

$$3O_2 + 12H^+ + 12e^- \rightarrow 6H_2O \text{ (cathode reaction)} \quad (8)$$

$$C_2H_5OH + 3O_2 \rightarrow 2CO_2 + 3H_2O \text{ (overall cell reaction)} \quad (9)$$

2.4 MFCs

At the beginning of the 19th century, Potter suggested the use of microbial cells to produce electricity for the first time.[41] This awesome idea was disregarded up to 1931. However, it was revived by Cohen after researchers demonstrated the oxidation of food by the enzymes present in bacteria.[42] MFCs are bio-electrochemical converters for turning chemical energy (produced by microbial metabolism of organic substrates) into electrical energy. There are two main types of MFCs. The first is single-chamber MFCs, which have a simple anaerobic anode chamber with no distinct cathode chamber and may not possess a PEM. The second is two-chamber MFCs, comprising an anaerobic anode and cathode (aerobic/anaerobic), arranged in aqueous solutions in two chambers, separated by a PEM (Fig. 4).[43–45] The unique feature of MFCs is the utilization of bacteria or microorganisms as biocatalysts to accelerate the oxidation of organic and inorganic compounds. Heterotrophic bacteria release energy during the oxidation of organic and inorganic materials, which is known as catabolism.[7] In this process, the electrons are captured from microbial cells and transferred to an electron acceptor (anode electrode) in the anode chamber. The transition of electrons between bacteria/microorganisms and the electrode can be performed without any external assistance (direct, mediator-less MFC) from the outer membrane of bacteria to the anode surface or by the acceptance of electrons from the electrode surfaces (indirect, mediator MFC). Generally, they are named exoelectrogens, in which electrons are transferred by self-produced redox mediators or by exogenous mediators. In an external electrical circuit, electrons flow from the anode to the cathode as the final electron acceptor to form an electrical current. The protons are also transferred by the membrane. The reduction of oxidant (oxygen) occurs on the cathode *via* the reaction of electrons and protons,

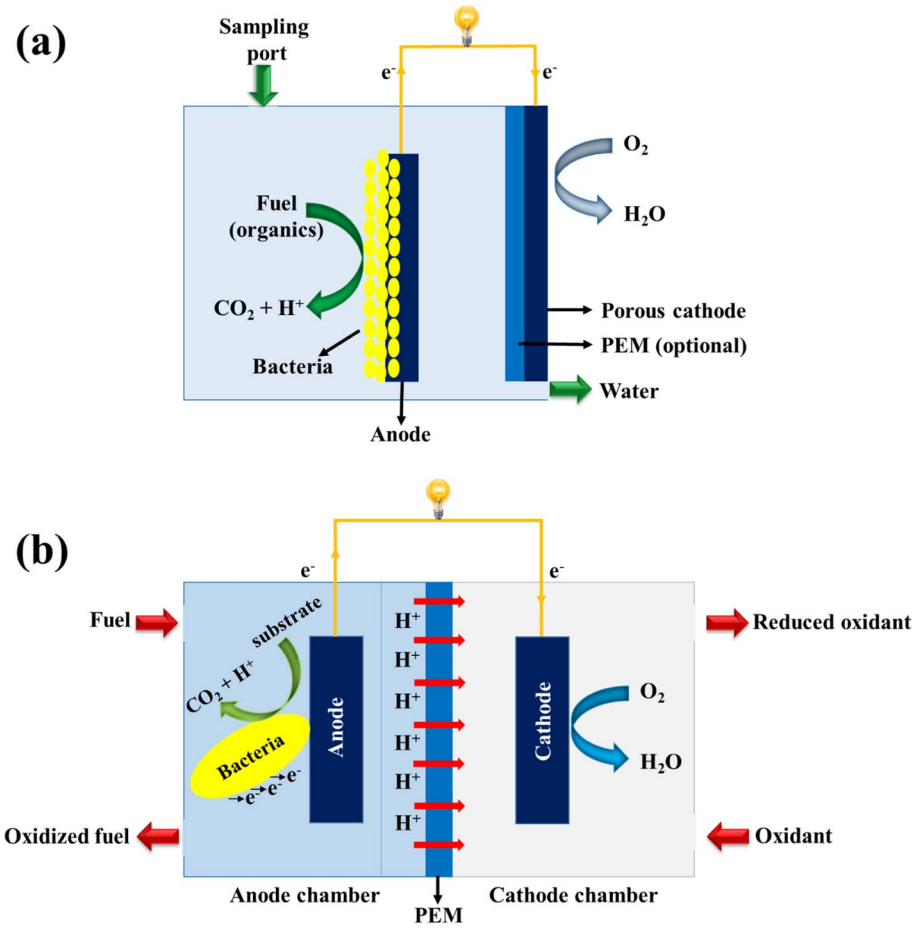

Fig. 4 Schematic of the principle of (a) single-chamber MFC and (b) two-chamber MFC. Modified from ref. 43 and 45, respectively.

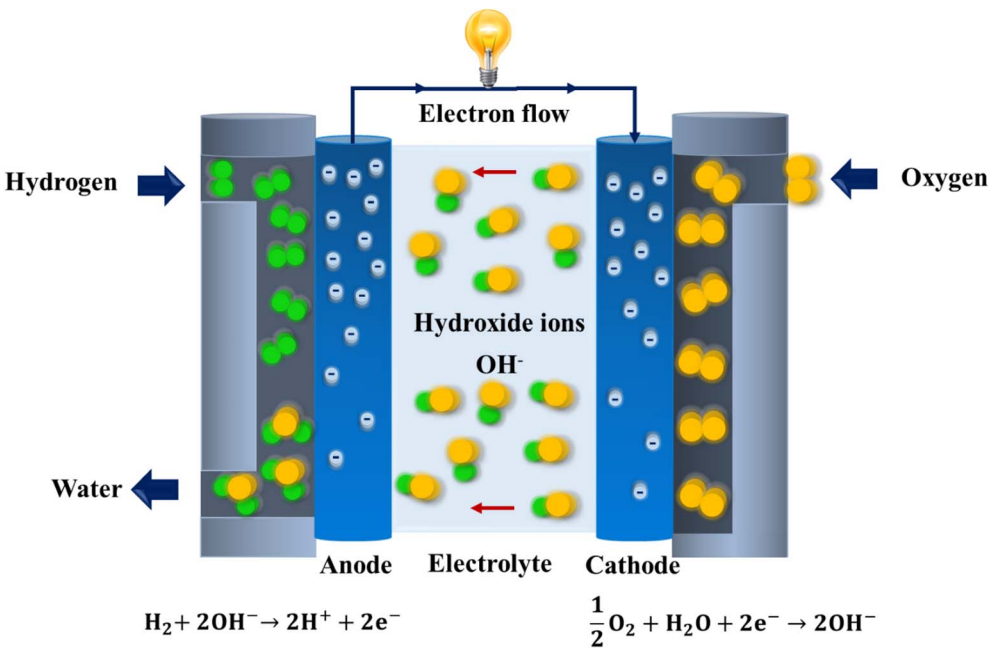

Fig. 5 Schematic of the operating principle of AFCs. Modified from ref. 25.

thereby generating water and electricity.[45,46] The oxidative catabolism and reduction reaction are defined as follows:

$$\text{Fuel (substrate)} \rightarrow CO_2 + H^+ + e^- \text{ (anode reaction)} \quad (10)$$

$$H^+ + e^- + O_2 \rightarrow H_2O \text{ (cathode reaction)} \quad (11)$$

MFCs can be applied in electricity generation, biodegradation of heavy metals/toxic compounds, and wastewater treatment. The efficiency of MFCs is commonly assessed based on energetic parameters, namely, power density, current density, potential difference, cell internal resistance, and biological treatment performance (COD removal). The CE is a noteworthy parameter that combines the two former ones, *i.e.*, the ratio of electron quantity that creates a current, obtained from the oxidation of the organic substrates to the total stored electron in the substrate.[47,48] Thus far, many efforts have been devoted to improving the output power in MFCs. Modifying the anode and cathode surfaces or membranes with nanomaterials is the most common approach to achieve this objective. The electrodes play a fundamental role in assisting exoelectrogenic biofilm formation and electrochemical reactions. In this case, nature-inspired materials can be a promising option to improve the functionality of MFCs.

2.5 AFCs

AFCs work with an alkaline electrolyte, typically a KOH solution, at low temperatures (50–70 °C). According to Fig. 5, hydroxide ions (OH^-) move through the electrolyte from the cathode to the anode, and then react with hydrogen at the anode to generate water and release electrons. The released electrons produce electrical power to an external circuit and move to the cathode. At the cathode, electrons combine with oxygen and water to generate more hydroxide ions, which diffuse into the electrolyte.[11,22,25] However, the need for pure hydrogen as a fuel is a major setback for AFCs given that the formation of carbonate occurs in the presence of CO_2, slowing the operation of AFCs. Nevertheless, the efficiency of AFCs is nearly 70%, making them a suitable option for spaceships given that they not only produce electric power but also produce drinkable water as a by-product for spacemen. NASA employed AFCs on Project Apollo and the Space Shuttle.[22,34] The working principle of AFCs is given by the following reactions:[49]

$$H_2 + 2OH^- \rightarrow 2H^+ + 2e^- \text{ (anode reaction)} \quad (12)$$

$$\tfrac{1}{2}O_2 + H_2O + 2e^- \rightarrow 2OH^- \text{ (cathode reaction)} \quad (13)$$

$$\tfrac{1}{2}O_2 + H_2 \rightarrow H_2O \text{ (overall cell reaction)} \quad (14)$$

2.6 SOFCs

SOFCs are the most applicable environmentally friendly fuel cells to realize large-scale stationary power generators with close to 60% efficiency and are capable of supplying electricity for factories and cities. Generally, SOFCs operate with a ceramic inorganic oxide such as calcium oxide or zirconium oxide as the electrolyte at approximately 600–1000 °C. At these high temperatures, the reactions are feasible at higher rates in the absence of the costly platinum catalysts, given that sufficient vapor and oxygen are supplied for complete oxidation. Also, natural gas can be utilized directly as fuel inside the fuel cell with no separate processing unit and has gained remarkable

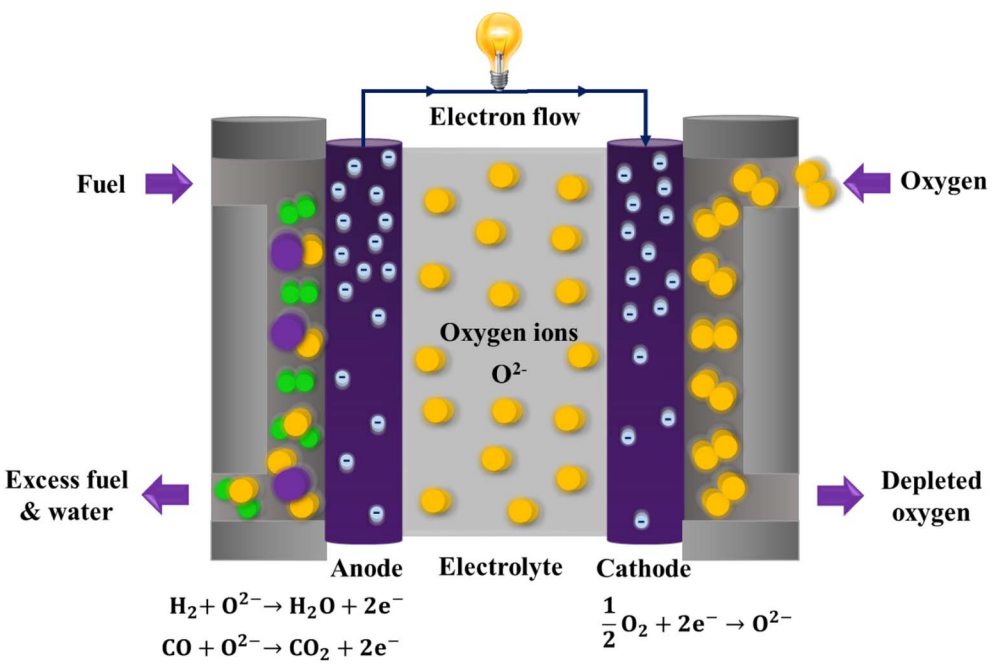

Fig. 6 Schematic illustration of the working principle of SOFCs. Modified from ref. 25 and 52.

interest for use in a wide variety of SOFCs, owing to its abundance.[25,50–52] SOFCs utilize rather low-cost ceramic materials compared to other fuel cells, which use noble metal catalysts. The cell of SOFCs has two porous electrodes (cathode and anode), and a solid electrolyte between the two electrodes to connect them. As shown in Fig. 6, at elevated temperatures, oxygen ions pass through the ceramic electrolyte from the cathode to the anode. They oxidize the fuel gas or hydrocarbon fuel including hydrogen and carbon monoxide that is generated during steam reforming, producing water and carbon dioxide at the anode (eqn (15a) and (15b), respectively). The electrons generated on the anode flow through an external circuit to the cathode, providing electricity along the way. Generally, oxygen is obtained from the air at the cathode and reacts with electrons to generate oxygen ions according to eqn (16).[52–54]

$$H_2 + O^{2-} \rightarrow H_2O + 2e^- \quad (15a)$$

$$CO + O^{2-} \rightarrow CO_2 + 2e^- \text{ (anode reactions)} \quad (15b)$$

$$\tfrac{1}{2}O_2 + 2e^- \rightarrow O^{2-} \text{ (cathode reaction)} \quad (16)$$

$$H_2 + CO + O_2 \rightarrow H_2O + CO_2 \text{ (overall cell reaction)} \quad (17)$$

3. Application of nature-inspired materials in fuel cells

The beneficial properties of nature-inspired materials make them potential candidates for the synthesis of efficient heterogeneous catalysts or to be used to make appropriate membranes for fuel cell applications. Herein, the description of nature-inspired materials namely clays, zeolites, and biomass is summarized, and subsequently their application in different type of fuel cells is discussed.

3.1 Natural aluminosilicates

The large abundance of natural aluminosilicates (clays and zeolites) makes them cost-effective. These materials, in raw and modified forms, possess moderate to high specific surface area and porous structure, making them promising materials in the energy and environmental fields, for instance, in energy storage and conversion applications.[19,55–57]

3.1.1 Clays. Natural clays, hydrous aluminosilicates, and family members of minerals that are obtained naturally from the Earth's surface have nearly the same elemental combinations and crystalline structures with a particle size of less than 2 μm. The size and unique crystal structure provide special features such as cation exchange capabilities, plastic behavior when wet, catalytic abilities, swelling behavior, and low permeability. These physical and chemical features define the possibility of using them in industrial processes. The formation of clay materials is dependent on the environment, and usually formed in environments of soil horizons, continental and marine sediments, geothermal fields, volcanic deposits, and weathered rock formations. Hence, the properties of clay materials are influenced by the environment. For instance, the ion exchange capability of clay appears due to the reaction of clay to erosion, transport, and deposition, which generally occur in the environment.[58] Generally, clays are available either in their formation location (denoted as primary clays) or a location where they were transported after their formation (denoted as secondary clays). Primary clay formation occurs when rock is chemically attacked by water. The mineral compounds and the impurities of the resulting clays are determined by the composition of the parent rock, the degree of completion of the reaction, and impurities introduced during or after their formation. The remaining primary clays produced from feldspar convention usually consist of silica and mica impurities. Cations such as sodium, potassium, and calcium are removed during or after the formation of these clays. Iron-based compounds are another impurity for primary clays. The white clays, well known as kaolin, seem to have less iron-based impurities, while the "China clay" is used as iron-free primary clays. The main industrial primary clay is majorly found in North Carolina in the United States and minor deposits in Pennsylvania, California, and Missouri, while China clay is found in Cornwall and England. For secondary clays, the mineral impurities such as mica and quartz are mostly removed. However, some impurities such as TiO_2 and iron-based compounds (Fe_3O_4) often remain during transfer. These clays include a wide range of clays. The secondary China clays are found in Georgia, Florida, South Carolina, Alabama, and Tennessee. The primary clays are white to ivory in color, while the secondary clays can be red or brown in color due to the presence of other impurities.[59] Therefore, it is important where the clay is sourced. Recently, the purification of clays has been considered an important challenge in industrial applications. To extract the clay mineral species (montmorillonite, kaolinite, illite, *etc.*), some approaches such as mechanical processing, sedimentation and centrifugation, elimination of organic matter, and elimination of carbonates are usually employed.[60] Alumina and silica are the major elements of clay, while magnesium, calcium, iron, potassium, and sodium oxides are minor elements of various types of clays.[61] According to the first classification of clay minerals, named the 'Grim classification', the clay minerals were divided into 3 main categories, namely, kaolinite, montmorillonite, and illite, and all other clays are made of one or more components of these three categories, which are briefly mentioned in Fig. 7.[61,62]

Raw kaolin and halloysite materials are mainly formed by kaolinite and halloysite, respectively. Among the clays, kaolins have the highest surface area, and great chemical and thermal stability.[64] Cornwall in England and Georgia in the USA are well-known established sources of kaolin. Also, Brazil and Australia have wide resources of high-quality kaolin. Asia, China, Japan, and India have several centers for kaolin production.[65] Kaolinites, the dioctahedric phyllosilicates (1 : 1) with the chemical formula of $Al_2Si_2O_5(OH)_4$, are organized as hexagonal to pseudohexagonal planes with periodic alumina octahedral and silica tetrahedral layers, known as platelet-like particles.[64] Halloysite clays ($Al_2Si_2O_5(OH)_4 \cdot nH_2O$) have the composition of kaolinite having water monolayer with a tube-shape structure and are

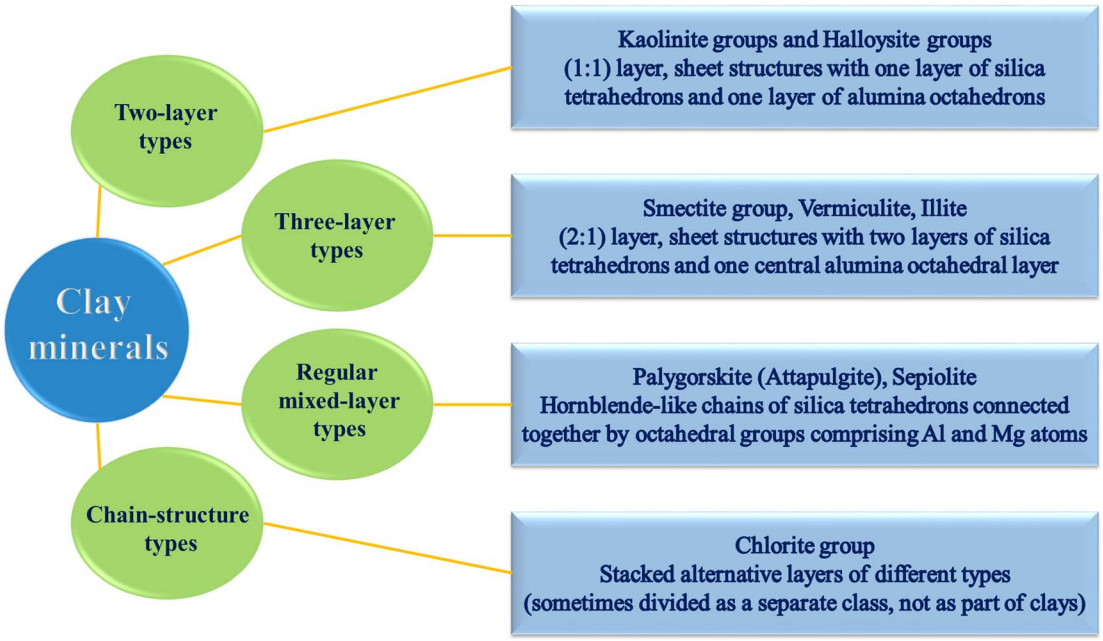

Fig. 7 Grim classification of clays. Modified from ref. 61 and 63.

commonly recognized as HNTs with a two-layer structure (1 : 1) having opened ends and internal lumen. The halloysite interlayer includes Al–OH nanosheets and is covered with Si–O nanosheets and its outer surface possess primarily Si–O–Si and Si–OH groups.[66] Halloysite is the prevailing kaolin mineral instead of kaolinite in many countries of the Pacific Rim. In addition, the Northland halloysite deposits in New Zealand are due to the rapid alteration of glassy rhyolites at low temperatures.[65]

Smectite groups (montmorillonite, talc, pyrophyllite, and saponite) with the chemical formula of (Na, Ca, H) (Al, Mg, Fe, Zn)$_2$((Si,Al)$_4$O$_{10}$)(OH)$_2\cdot n$H$_2$O have three (2 : 1) layers, *i.e.*, alumina octahedral nanosheets sandwiched between two silica tetrahedral nanosheets. The nanosheets aggregate into a plane surface and possess a high surface area. The layers are weakly bonded to each other to facilitate ion transfer between the interlayers, leading to desirable properties.[63,67] Bentonite, as an impure mineral, is considered a member of the smectite group and a montmorillonite-based clay mineral with additional crystalline structures and has high capacity for water absorption.[68,69] It is abundantly found in China, Indonesia, Russia, Chile, and India.[65] The illite group is the only common clay type representing the mineral illite. It is well-known as one of the phyllosilicates, or layered alumino-silicates with the general formula of (K,H)Al$_2$(Si,Al)$_4$O$_{10}$(OH)$_2\cdot n$H$_2$O. They have a similar structure to smectite layers.[63] Vermiculite clays with the typical chemical formula of $M_{0.75}^{+}Al_2(Si_{3.25}Al_{0.75})O_{10}(OH)_2$ have layered structure (2 : 1 type structure) and high pore volume. The shrinking and expansion of their interlayers lead to great cation-exchange capacity. It is well known that two-dimensional materials can diminish the ion diffusion route.[70]

Palygorskite (also called attapulgite) clays are accumulated irregular fibrous nanorods with the chemical formula of ((Mg,Al)$_2$Si$_4$O$_{10}$(OH)$\cdot$4(H$_2$O)), which possess a porous structure, non-expandable layers, enlarged surface area, and high thermal and chemical stability. Hence, palygorskite can absorb more electrolyte and enhance the safety of energy devices.[71,72] Sepiolite (Mg$_8$Si$_{12}$O$_{30}$(OH)$_4$(OH$_2$)$_4\cdot$8H$_2$O) clays are built of blocks consisting of two tetrahedral silica sheets and a central octahedral sheet with magnesium, showing a sandwich structure. The blocks are connected along their linear edges and possess a vein-like network of parallel channels, expanding in parallel directions of the fiber length.[73] Spain dominates in the production of sepiolite, while Southern Georgia is the main reserve for the production of palygorskite. Additionally, a considerable amount of palygorskite is produced in Senegal, Spain, India, Turkey, Ukraine, Australia, South Africa, and the Peoples Republic of China.[65]

Besides, the cost-effectiveness and natural abundance of natural clays, their thermal and mechanical stability, and fire-resistant properties make them potential materials for large-scale usage. Among the natural clays, kaolin and montmorillonite show the highest surface area of 359 m^2 g^{-1} and 249 m^2 g^{-1}, respectively.[19] The porous architecture and high surface area of clays facilitate fast ion diffusion, high ionic conductivity, and excellent hydrophilicity, which are worthwhile properties for solid-state electrolytes or separators in the field of fuel cells. Moreover, due to their superior porosity, they can absorb more electrolyte and keep enough charge carriers between the electrodes, resulting in an improvement in the stability of interfaces and nanostructures and enhancing the diffusion of electrons and ions. However, they possess low electronic conductivity, preventing the fast transfer of electrons when used as electrode materials. Furthermore, natural clays possess inherent impurities, including metal oxides, silts, and quartz.[19,74–76] Due to the aforementioned deficiencies of clays, several modification

methods such as acid treatment, cationic exchange, expansion of interlayer spacing, calcination treatment, modification with a pore-forming agent, and wettability modification can be suitably used to enhance the properties of clays in fuel cell applications. Expanding the interlayer spacing *via* the exfoliation of natural clays leads to a weak structure, improving the fast ion diffusion, and porosity, thus enhancing the electrolyte uptake.[77] Incorporating clays in a polymer matrix outstandingly promotes their mechanical properties and thermal properties. The cationic exchange reaction, which is attributed to the electrostatic absorption between the negatively charged surface of clays and cationic surfactants, enhances the mechanical and thermal properties of natural clays and an expanded interspace. The cationic parts expand the interlayer spacing of the clay and convert the hydrophilic clays into organoclays. Modifying natural clays with hydrophilic polymers increases their hydrophilic properties.[78–80] Generally, calcination treatment is performed to eradicate the organic phases or impurities of natural clays. Moreover, this process can provide more adsorption sites.[81] Also, modification with a pore-forming agent considerably increases the specific surface area of natural clays.[82]

Montmorillonite, bentonite, kaolinite, halloysite, sepiolite, and palygorskite are the most popular natural nanoclay minerals utilized in energy and environmental applications. These clay minerals have a porous structure, remarkable surface area, high chemical and thermal stability, and mechanical strength, which can be employed in polymeric matrixes to produce fuel cell membranes with good proton conductivity and high thermal stability. The improvement in the proton conductivity can be attributed to the presence of water in the clay particles. The water uptake is enhanced when clay minerals are used in fuel cell membranes, facilitating proton transferring. In addition, ceramic membranes fabricated by different clay minerals can be introduced as affordable alternatives to polymeric membranes.[83–85] Montmorillonite is possibly one of the most widely used natural mineral clays due to its outstanding features of swelling, ion proton exchange ability, and facile modification. The ionic conductivity of montmorillonite is dependent on the interlayer water molecule content.[85,86] Bentonite with a high surface area and lamellar structure is another interesting clay, which can be used as an ion exchanger in polymeric membranes for different types of fuel cells.[87] Kaolinite, a great alternative to montmorillonite, demonstrates high hydrophilicity, and thus can function as a practical filler for improving the mechanical and thermal characteristics of polymeric composites.[88] Halloysite is a cost-efficient and abundant natural aluminosilicate clay with a tube-shaped structure, which can be used to prepare porous catalysts with a high surface area for fuel cells.[89] Also, it can be combined with different polymers to produce membranes with significant proton conductivity at a high temperature operating.[90] Sepiolite and palygorskite, with high hydrophilicity and porous structure, are fibrous mineral clays that can improve the mechanical stability of membranes due to their unique morphology.[91,92] They can also be employed as a catalyst support for enhancing the catalytic activity and durability of materials due to their porous structure and high surface area.[93–95]

3.1.2 Zeolites. Zeolites are another class of aluminosilicates comprised of tetrahedral silicon (Si^{4+}) and aluminum (Al^{3+}).[96] The arrangement of these tetrahedra induces a large pore volume in the crystals. The natural zeolites with honeycomb or cage architecture are proton conductors and hygroscopic materials with a high specific surface area and functional groups. The porosity of zeolites is measured by their crystalline structure, which is in the range of 0.1–0.35 $cm^3\ g^{-1}$.[97] This microporous structure leads to very high internal surface areas in the range of 300 to 700 $m^2\ g^{-1}$.[98,99] Thus, due to these properties, zeolites can form composite materials that provide superior properties for energy conversation applications. However, some metal impurities, especially Fe impurities, also exist in the zeolite structure. For example, waste-derived zeolites consist of different metal impurities, which can affect their catalytic performance. However, it was found that the high metallic impurity values have a positive influence on the catalytic performance of zeolites.[100,101] For example, waste-derived zeolites with metal ions impurity have a positive influence on catalytic stability in the methanol to olefins process.[100] In addition, zeolites possess low toxicity due to the presence of silica.[102] Depending on the arrangement of the tetrahedra, various zeolite frameworks with varying compositions are observed. Aluminum ions can substitute for some silicon ions in the tetrahedral sites, resulting in the $(Si,Al)O_4$ framework having a net negative charge due to the difference in the capacity of the $(AlO_4)^{5-}$ and $(SiO_4)^{4-}$.[70,103,104] Generally, the negative charge is balanced by alkaline or alkaline earth metal cations, which coexist in the channels and pores besides water molecules. Na^+, K^+, Ca^{2+}, Li^+, Mg^{2+}, Sr^{2+} and Ba^{2+} are present in different zeolites.[105] These cations are exchangeable, thereby endowing zeolites with cation exchange properties, similar to phyllosilicates, while the small cations can travel through the pores because of the rigid framework of the tetrahedra in the zeolites. Hence, zeolites are mostly proposed as 'molecular sieves' due to their selective cation exchange properties. The cation exchange capacity of natural zeolites was reported to be 600–4000 meq. kg^{-1}, which is higher than that of natural clays such as kaolinite (100 meq. kg^{-1}) and montmorillonite (1000 meq. kg^{-1}).[106–108] There are 235 various types of natural and synthetic zeolites registered in the International Zeolite Association.[109] Many zeolites are formed naturally as minerals and are widely extracted in many regions of the world especially in soils in arid regions. The general chemical formula of natural zeolites is $[(Li,Na,K)_a(Mg,Ca,Sr,Ba)_d(Al_{(a+2d)}Si_{n-(a+2d)}O_{2n})]\cdot mH_2O$.[104,105,110,111] About 45 different types of natural zeolites exist with different morphologies. The most popular and useful natural zeolites are clinoptilolite, chabazite, analcime, and mordenite. Generally, clinoptilolite is formed as planes or laths with tabular form, represented by the chemical composition of $(Na,K)_6(Si_{30}Al_6O_{72})\cdot 20H_2O$ and Si/Al molar ratio of 4.0–5.7.[103,104] Chabazite possesses a cube-like structure with the chemical formula of $Ca_2(Al_4Si_8O_{24})\cdot 12H_2O$ with the Si/Al molar ratio of 1.4–4.[104] Analcime ($Na_{16}(Al_{16}Si_{32}O_{96})\cdot 16H_2O$) has a low Si/Al molar ratio of 1.8–2.8 and a cubic crystal structure.[112] Mordenite ($Na_2KCa_2(Al_8Si_{40}O_{96})\cdot 28H_2O$) commonly occurs as tiny fibers or fine laths and needles with an Si/Al molar ratio of 4.0–5.7.[104,113]

3.2 Biomass

Organic waste and biomass are other types of nature-inspired materials that have recently received comprehensive interest as perfect and sustainable carbon-based materials owing to their commercial availability, environmental safety, superior biocompatibility, low density, high hydrocarbon content, and corresponding reduced cost.[114–119] The most common sources of biomass are schematically represented in Fig. 8. Biomass consists of the products, by-products, waste, and residues from agriculture processing, industrial and human activities. Green agricultural residues include straw, stover, cane trash, forestry crops, and wastes. Organic uneatable or unneeded components of food materials consist of biowastes such as skins or peels, cores, pips or stones, husks, shells, fish waste, and juice pulp. Also, eco-friendly organic portions of industrial and municipal solid losses (sewage, animal, and human wastes) are considered biowaste. Animal wastes comprise slurries, manures, animal bedding such as broiler litter, and silage grass.[120,121] The lignocellulosic biomass, consisting of three basic components, *i.e.*, lignin, cellulose, and hemicellulose, has variable chemical structures and compositions depending on its sources, climate, age, and the location of the plant.[121,122] The availability and feasibility of organic wastes and biomass for use as a filler or support in polymer composites have achieved considerable interest in the last decade.[123–125] Furthermore, biomass-derived carbonaceous materials have been suggested as an alternative to conventional carbon catalysts for electrochemical applications such as fuel cells due to their intrinsic porous architecture, lower cost, high surface area, excellent biocompatibility, eco-friendly properties, and higher electrochemical activity.[126–129] In the limited-oxygen condition, biomass can be thermochemically converted to biochar, which is different from CB and has more functional groups and stability. Generally, there is around 54–93% carbon in biochars.[130] Biomass materials possess nitrogen and phosphorus, which result in the creation of further active sites in biomass-derived carbon.[130–133] Biomass-derived carbonaceous materials are chemically and physically stable and have various types of surface functional groups rich in oxygen and nitrogen content. However, carbon-based materials contain some metallic impurities even without the direct involvement of metals during their synthesis. Thus, if proper purification is not performed, a large amount of carbon-based materials will remain useless.[134] Furthermore, these impurities can significantly improve or impair the electrochemical performance of carbon-based materials.[135,136] CNTs and graphene are two well-known metal-free catalysts and the presence of impurities is widely investigated. In addition, the application of biomass brings another challenge. One of the significant challenges in the large-scale biochemical application of biomass is the accessibility of their sources. Hence, the

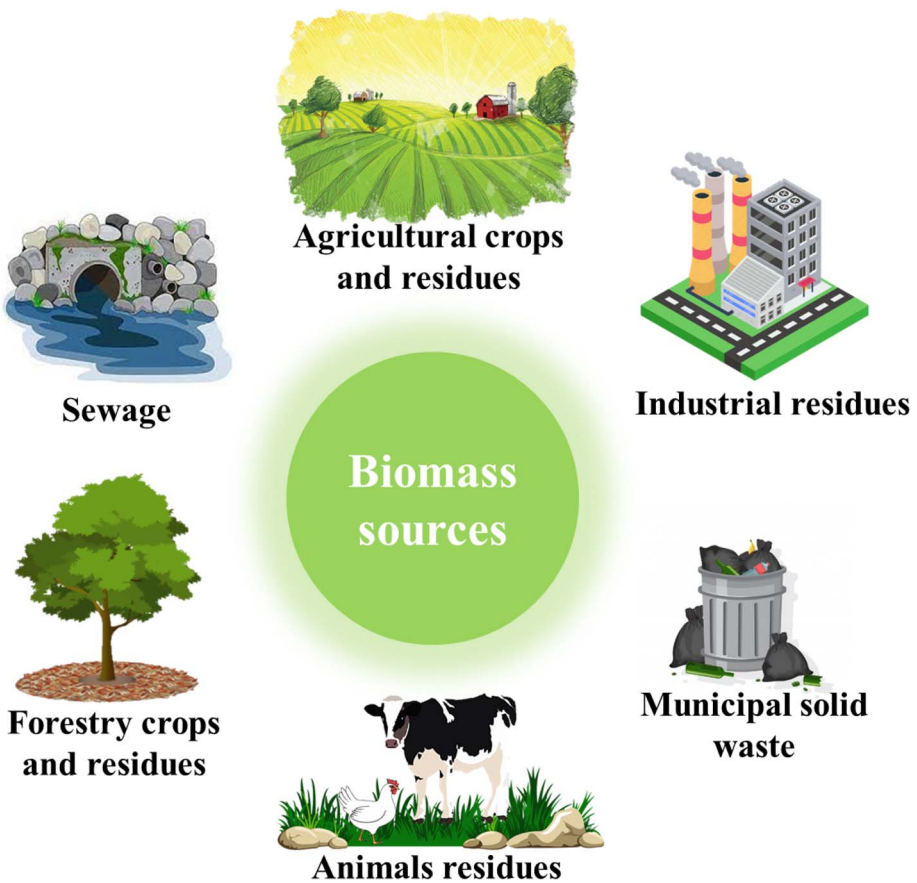

Fig. 8 Schematic of the most common sources of biomass.

excessive use of biomass can damage the environment and ecosystem. Another common disadvantage of biomass is its high moisture content, which varies from 3–63% and can reach up to 90%. This high moisture leads to problems in biomass conversion, as follows: (1) poor combustion, formation of high amount of fumes during its combustion, an increasing unburnt carbon; (2) sedimentation of chlorides, carbonates, sulphates, nitrates and phosphates during its drying; (3) increased washing during its processing and (4) the possibility of reproduction of fungi and mold in biomass. The presence of high contents of alkaline and halogen elements in biomass can result in some environmental problems of enhanced volatilization and releasing dangerous compounds such as Cl_2, HCl and HBr as well as fine particulates. One of the major problems in the conversion of biomass is the existence of some toxic trace elements such as Ag, Be, Cd and Hg, increased volatilization and limited retention and capture performance during biomass combustion as well as washing during biomass processing. The small size and low bulk density of biomass fly ash cause safety risks during its transport, storage, and processing because it result in the release of fine particles. Besides, biomass materials are composed of various components, causing irregular quality of byproducts. However, this diversity leads to the utilization of different biomass conversion approaches, applications of biomass in diverse processes and production of different materials.[134] Biomass conversion *via* supercritical water requires high energy for heating the environment above the critical water point (648 K, 22.0 MPa), which is one of the most significant disadvantages of applying biomass.[137]

Naturally porous and hierarchical networks can boost the approachability of electrolytes to the electrode and shorten the ion transfer routes. These properties make them a preferred choice in several applications, especially in the field of electrocatalysts for fuel cells.[130,131,138] The pyrolysis temperature plays an important role in controlling the textural and physical properties of the resulting carbon materials. The formation of biochar by pyrolysis at low temperatures is not an appropriate method to produce carbon-enriched materials for energy storage and conversion application due to their inferior pore characteristics, low surface area, and poor conductivity.[139] In contrast, the hydrothermal carbonization process at a relatively low temperature is a suitable method to produce hydrochar. Carbohydrate-derived hydrothermal carbons have spherical-shaped particles with different polar functionalities, improving their hydrophilic properties.[133,140] The hydrothermal carbonization process leads to the formation of a relatively homogenized morphology. The particle size differs depending on the time of carbonization and concentration of the precursor.[140,141] Also, it is necessary to modify and activate their surface by suitable physical or chemical activation methods for use as electrochemical energy storage materials with high porosity, enlarged surface area and enhanced content of functional groups.[130]

Food, crops, and their residues (such as eggshells, fruits and vegetables, and their peel, shell, core and stone, rice husk, nut shell, sugar cane, and waste tea), chicken feathers, leaves, sewage sludge, fly ash and human hair are the most common biomass and organic waste used in the field of fuel cells as catalysts or fillers for the polymer matrix.

3.3 Nature-inspired materials as membranes or catalysts for PEMFCs

3.3.1 Aluminosilicate-based (nano)materials

3.3.1.1 Membranes. In 2010, Kongkachuichay and Pimprom prepared Nafion/analcime and Nafion/faujasite composite membranes by incorporating analcime and faujasite in the Nafion polymer matrix.[142] The aluminosilicate powders were dispersed in a Nafion solution *via* ultrasonication. Subsequently, the membranes were cast on glass plates and dried at 50 °C for 2 h. They were compressed using Teflon plates, and finally dried at 160 °C for 30 min. The composite membranes demonstrated an improved performance compared to the pristine Nafion membranes in terms of ion exchange capacity, proton conductivity, water uptake, and hydrogen permeability. Also, the analcime-based membrane exhibited a better performance than the faujasite-based membrane. Among the membranes, the Nafion/analcime (15%) gave the best performance with the optimum proton conductivity as high as 0.4373 S cm^{-1} (6.8-times higher than that of Nafion, *i.e.*, 0.0642 S cm^{-1}) at 80 °C. Similarly, the preparation of a blend membrane consisting of SPEEK and analcime as a proton exchange membrane for PEMFCs was reported in another work.[143] Analcime was modified to the H-form before blending. A reduction in water uptake and IEC was reported for the membranes with increased weight ratios of analcime. Among them, the SPEEK/10% analcime composite was determined to be the best membrane owing to its highest proton conductivity of 0.4016 S cm^{-1} with the activation energy of 15.1 kJ mol^{-1}. The use of analcime in H-form resulted in the creation of a hydrophilic linked 3D channel comprised of protons, thus increasing the conductivity of the membrane. With a high weight ratio of analcime loading, the solid particles aggregated, resulting in a decline in conductivity, which was lower than that of the pure SPEEK. A blend membrane comprised of SPEEK and sodium-rich smectite clay (3 and 6 wt%) was synthesized *via* a solution casting method.[144] The casting process was performed on a plexiglass plate, which was heated at 80 °C for 24 h to completely evaporate the solution. The thickness of the as-prepared membrane was 100 μm. The SPEEK membranes in the presence of smectite clay presented better thermal stability, higher water uptake, lower methanol permeability, and higher conductivity compared to the pure SPEEK membranes. The conductivity of the SPEEK/6 wt% clay membrane increased to 2 $\times$ 10^{-2} S cm^{-1} at 140 °C with excellent dimensional stability, indicating its high efficiency for application in PEMFCs.

3.3.2 PGS (ATP)-based (nano)materials

3.3.2.1 Membranes. To improve the utilization efficiency of Nafion® membranes in PEMFCs, PGS, and 1D hydrophilic mineral NFs were incorporated in the Nafion® matrix.[145] The water retention ability and mechanical performance of Nafion® increased by 10% and 25% in the presence of PGS, respectively. PGS also improved the proton conductivity of Nafion®. The proton conductivity of PGS/NF was reported to be 0.028 S cm^{-1},

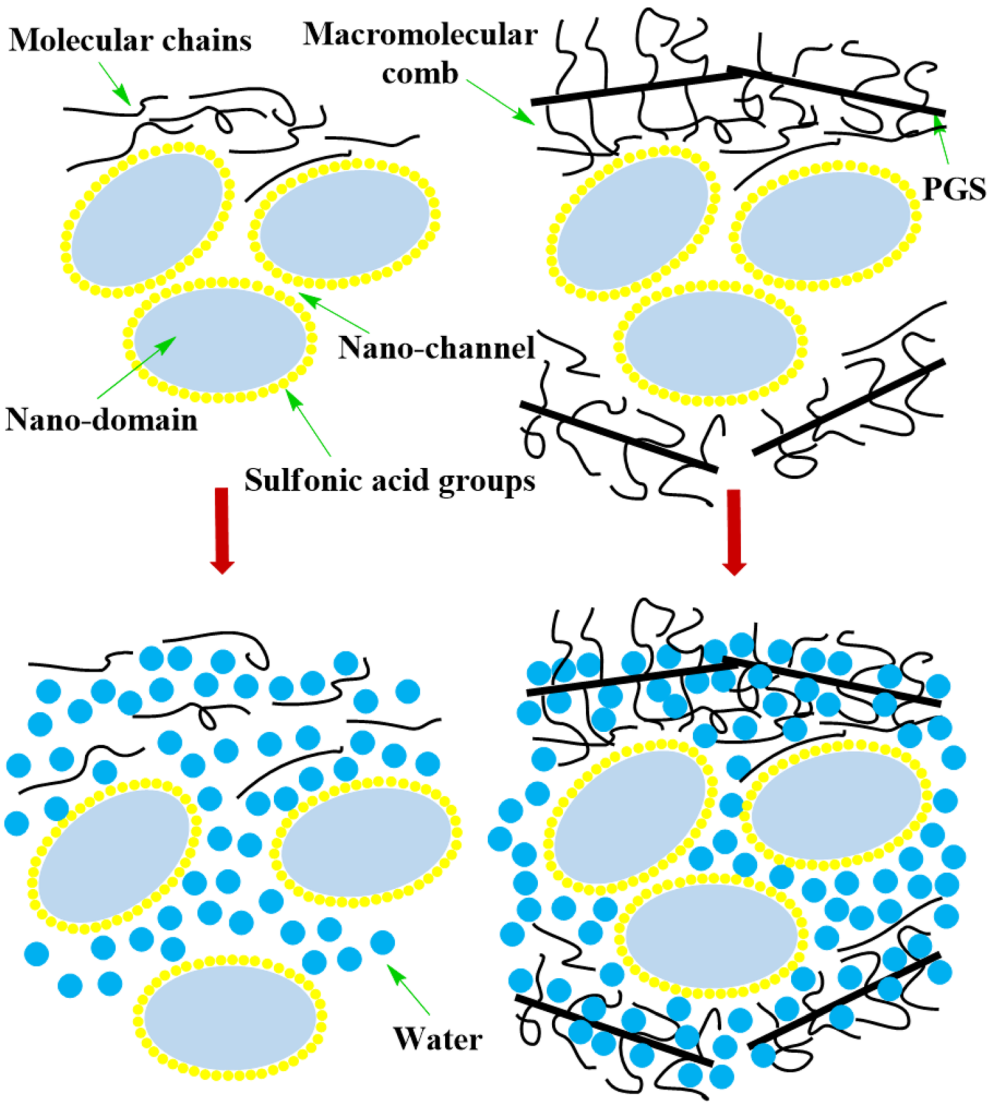

Fig. 9 Schematic representation of NF and PGS/NF structures and their water uptake process. Reprinted with permission from ref. 145. Copyright (2011), Elsevier.

which was 75% greater than that of pure Nafion® (0.016 S cm^{-1}) under 0% RH at 303 K (~30 °C). Fig. 9 schematically displays the accumulation of nano-domains, forming nano-channels in dry Nafion®. The interaction between SO_3^- groups was weakened through the swelling process and diffusion of H_2O molecules. The nano-channels increased in size, leading to the separation of the hydrophobic nano-domains and expansion of the membrane. However, in the composite membrane, the nano-domains were trapped by macromolecular combs and the PGS bundle network, preventing nano-domain separation during the hydrating process. Consequently, the GPS/NF membrane had better stability and proton transfer.

Natural ATP was modified using a silane coupling agent (DC5700) and incorporated in CS as a biopolymer matrix to synthesize a PEM membrane.[146] The mixed solution of CS and organic chains of QATP was cast on the surface of a glass plate and dried in a vacuum oven at 35 °C for 24 h. Subsequently, the membrane was immersed in NaOH solution (5 wt%) for 2 h to remove acetic acid, followed by rinsing with DW. The cross-linked CS/QATP PEM was prepared by immersion in 2 M H_2SO_4 for 24 h, followed by washing with DW. The introduction of QATP increased the interfacial interaction and it served as a bridge between CS and QATP. Hence, the properties of the CS/QATP membrane were improved. The water uptake of the CS/QATP membranes was reduced due to the creation of more hydrophobic regions. The CS/QATP membrane exhibited greater thermal and dimensional stability than the pristine CS membrane. Among them, CS/QATP-2 was found to show the best performance with the proton conductivity of 31.6 mS cm^{-1} at 80 °C and mechanical strength of 43.3 MPa, highlighting its considerable potential for application in PEMFCs.

3.3.3 MMT-based (nano)materials

3.3.3.1 Membranes. A protonated MMT (MMT-H) was prepared *via* stirring in diluted HCl solution under reflux for

24 h and was utilized to synthesize PBI-doped PA membranes (p-PBI).[147] This work indicated that introducing MMT-H can effectively increase the proton conductivity and mechanical stability (over 100%) of p-PBI/MMT-H in comparison with Celtec®-P probably due to the trapping of water and PA by the MMT-H channel. The highest proton conductivity (436 mS cm^{-1}) was observed for p-PBI/MMT-H with 50 wt% MMT-H at 20% relative RH at 160 °C. Therefore, the as-prepared membranes exhibited a great performance in PEMFCs. Also, novel hybrid materials were synthesized using a natural

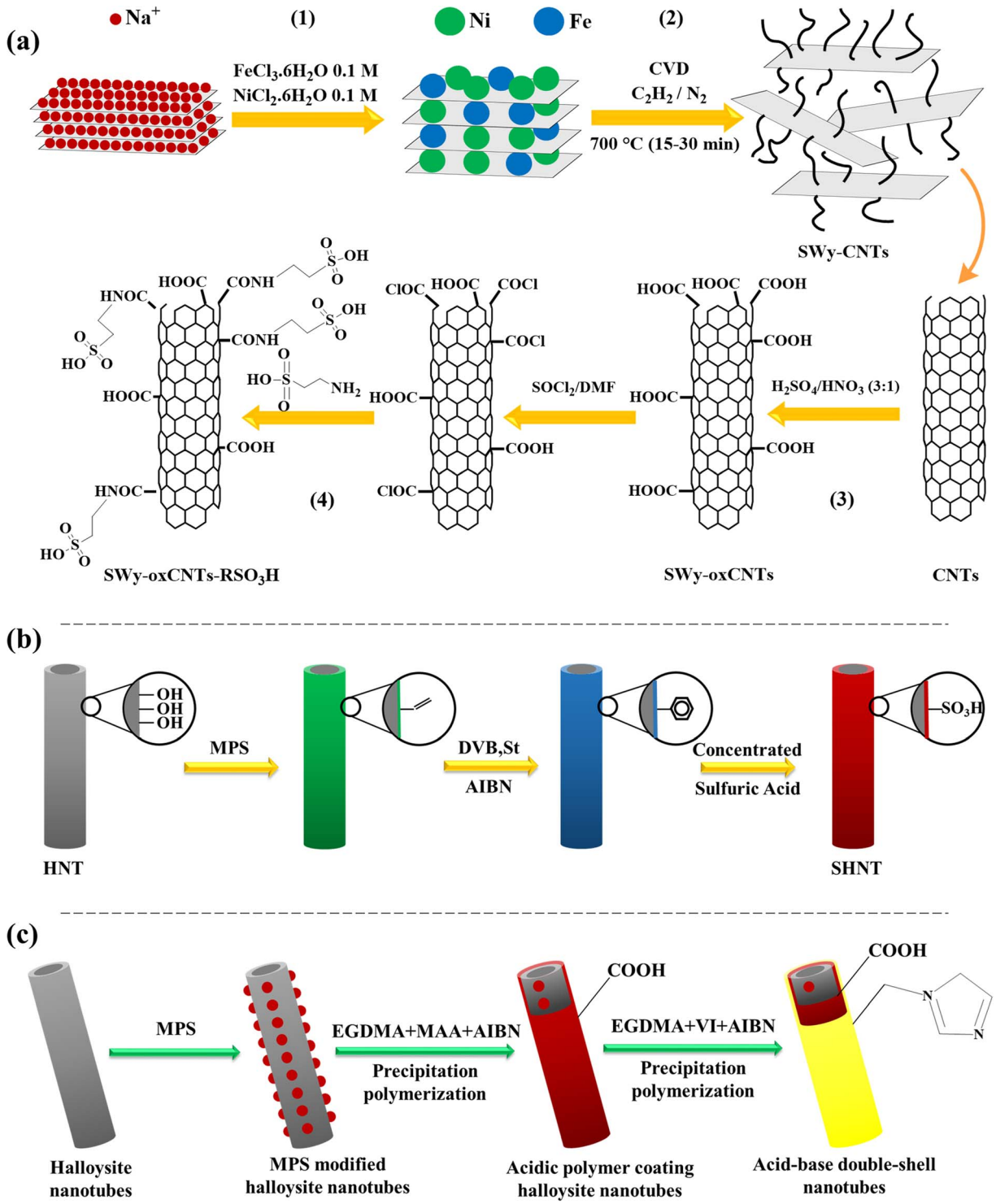

Fig. 10 (a) Fabrication of clay-CNT hybrid materials used as nanoadditives in Nafion polymer. Reprinted with permission from ref. 148. Copyright (2016), the American Chemical Society. (b) Representation of the synthesis process of sulfonated HNTs. Reprinted with permission from ref. 151. Copyright (2014), Elsevier. (c) Preparation of acid–base double-shell polymer nanotubes. Reprinted with permission from ref. 153. Copyright (2020), Elsevier.

smectite MMT clay (SWy-2) as a substrate for the growth of CNTs *via* the catalytic CVD method and a Nafion®-based composite membrane fabricated according to Fig. 10a.[148] Sidewall oxidation and organo-modification of CNTs created an extremely hydrophilic material and improved the proton transportation of the membranes with SWy-oxCNT-RSO_3H, especially at high temperatures (above 100 °C). The water uptake of nanocomposites increased by about 40% more than that of Nafion®. The best proton conductivity (0.07 S cm^{-1} at 120 °C and 30% RH and 0.25 S cm^{-1} at 120 °C and 90% RH) was reported for the N/SWy-oxCNT-RSO_3H(y5) membrane containing 3 wt% filler. A GO-intercalated MMT layered stack was synthesized as a proton carrier for moderating the dependency of Nafion-based PEMs on highly-humid media.[149] The modification of MMT was performed by sulfate-reducing bacteria in the precipitation and respiration of microbial-inducing calcium to obtain the mMMT with enhanced interlayer gaps. Then, the distended MMT could be easily intercalated and destroyed. Thus, the mMMT was interdigitated with GO nanosheets to form layered stack composites (GO@mMMT). The GO@mMMT layered stacks were embedded in a Nafion polymer *via* a normal solution casting method. By inserting GO nanosheets in the mMMT interspaces, a layered stack structure was fabricated with a remarkably increased surface area, leading to an improvement in the water absorption and retention capacity. In addition, GO nanosheets were interdigitated with mMMT lamellae, which resulted in the formation of rapid proton conduction routes along GO and limited presence of water in the slit-like channels between the mMMT and GO layers. The mechanism of proton conduction in GO@mMMT/Nafion PEM was illustrated with three proton transfer channels, as follows: (1) transferring by a large content of free adsorbed water adsorbed on the hydrophilic sulfonic acid ions and GO@mMMT particles in the interchannels of the PEM; (2) transferring by limited water in the sub-nanochannels between GO and mMMT layers; and (3) transferring by the sulfonic acid framework itself. Furthermore, GO can also be placed on the mMMT surface, resulting in the structure of GO–mMMT–GO. Therefore, hydrophilic functional groups of –OH, C–O–C, and –COOH on GO could easily absorb water, facilitating the proton transfer. Hence, the major contributions of proton conduction improvement in a high-humidity medium were associated with its excellent water absorption, while it resulted from its great water retention in a low-humidity medium. The 0.5GO@mMMT/Nafion PEM showed a proton conductivity of 36.4 mS cm^{-1} and 17.3 mS cm^{-1} at 80 °C with 98% and 20% RH, respectively. A peak power density of 546 mW cm^{-2} was obtained for this cell, which is notably higher than that of the recast Nafion PEM and much better than the values reported in many studies.

3.3.3.2 Catalysts. Pai and Tseng treated a carbon support, and then dispersed MMT on it *via* an ultrasonic mixed technique for preparing graphitized carbon-supported Pt oxygen electrodes as a unitized URFC catalyst support.[150] The uniform dispersion of MMT and GC support synergistically address the agglomeration issue of pure graphitized carbon particles. To test the efficiency and performance of the fuel cell, both sides of a PEM (DuPont-Nafion 212) were coated with the synthesized electrocatalyst and placed in a URFC system. The results indicate that the presence of MMT improved the PEMFC performance. The optimal power density and current density of this electrode were reported to be 240 mW cm^{-2} with 690 mA cm^{-2}, which were higher than that of the electrode without MMT (180 mW cm^{-2} and 500 mA cm^{-2}), respectively. The maximum specific charge transfer was reported for electrodes with 20 wt% MMT. The cell potential in the water electrolysis operation and fuel cell operations was 1.67 and 0.6 V at 100 mA cm^{-2}, respectively. In the water electrolysis operation, the rate of hydrogen generation of the URFC was nearly 0.34 mL min^{-1} at 105 mA cm^{-2}. In the fuel cell operation, the URFC exhibited a maximum power density of 190 mW cm^{-2} at a current density of 404 mA cm^{-2}. The energy conversion efficiency of the as-prepared electrode was 37.5%. The energy transfer efficiency could reach up to 50.6% when the produced hydrogen was used to generate electricity.

3.3.4 Halloysite-based (nano)materials

3.3.4.1 Membranes. Sulfonic acid groups were also loaded on tubular HNTs for the synthesis of nanocomposite membranes by incorporating sulfonated HNTs (SHNTs) in SPEEK, as shown in Fig. 10b.[151] The ionic channels in the SPEEK/SHNT membranes provided proton routes and allowed the effective proton transfer through a membrane with low resistance, resulting in increased proton conductivity. SPEEK/S4HNT-10 (containing 10% SHNT, obtained by concentrated sulfuric acid in 4 h) gave the maximum conductivity of 0.0245 S cm^{-1}, which was 61% greater than that of SPEEK at 25 °C and 100% RH. The water uptake of the SPEEK/S4HNT membrane was improved owing to hydrophilic $–SO_3H$ groups of the tubular SHNT. The highest water uptake value of 20.4% was observed for SPEEK/S4HNT-10. The incorporation of HNTs grafted with amino groups and CeO_2 in Aquivion® ionomer was offered for application in PEMFCs as a membrane (Aquivion® + CeO_2@HNT-NH_2).[152] The membranes comprised of 4 wt% CeO_2@HNT-NH_2 showed relatively high proton conductivity of 160 mS cm^{-1} and enhanced stability to radical attack compared to Aquivion® membrane with proton conductivity of 190 mS cm^{-1} at 90 °C and 95% RH. However, it revealed the same tensile properties. Sun *et al.* utilized halloysite nanotube seeds to synthesize an acid–base double-shell nanotube, which was later incorporated in SPEEK (Fig. 10c).[153] The carboxylic internal shell enhanced the combined water amount, endowing SPEEK/DSNT-A@B membranes with higher water retention. The proton conductivity of SPEEK/DSNT-A@B-5 (5 wt% of filler) was found to be 0.336 S cm^{-1} at 80 °C and 100% RH, which was 2-times higher than the pure SPEEK membrane. The water loss of the SPEEK/DSNT-A@B-10 membrane was 54.55% at 40 °C and 20% RH, which was 32.77% less than that of the SPEEK membrane. Hence, it has good potential efficiency for application in PEMFCs at low RH and high temperature.

A novel membrane was fabricated by confining ionogels in the lumen of HNTs with the assistance of $ScCO_2$.[154] ABPBI/IL@HNT composite membranes were synthesized *via in situ* synthesis and doping with low levels of PA, as shown in Fig. 11a. The benefit of this strategy is the utilization of HNTs with

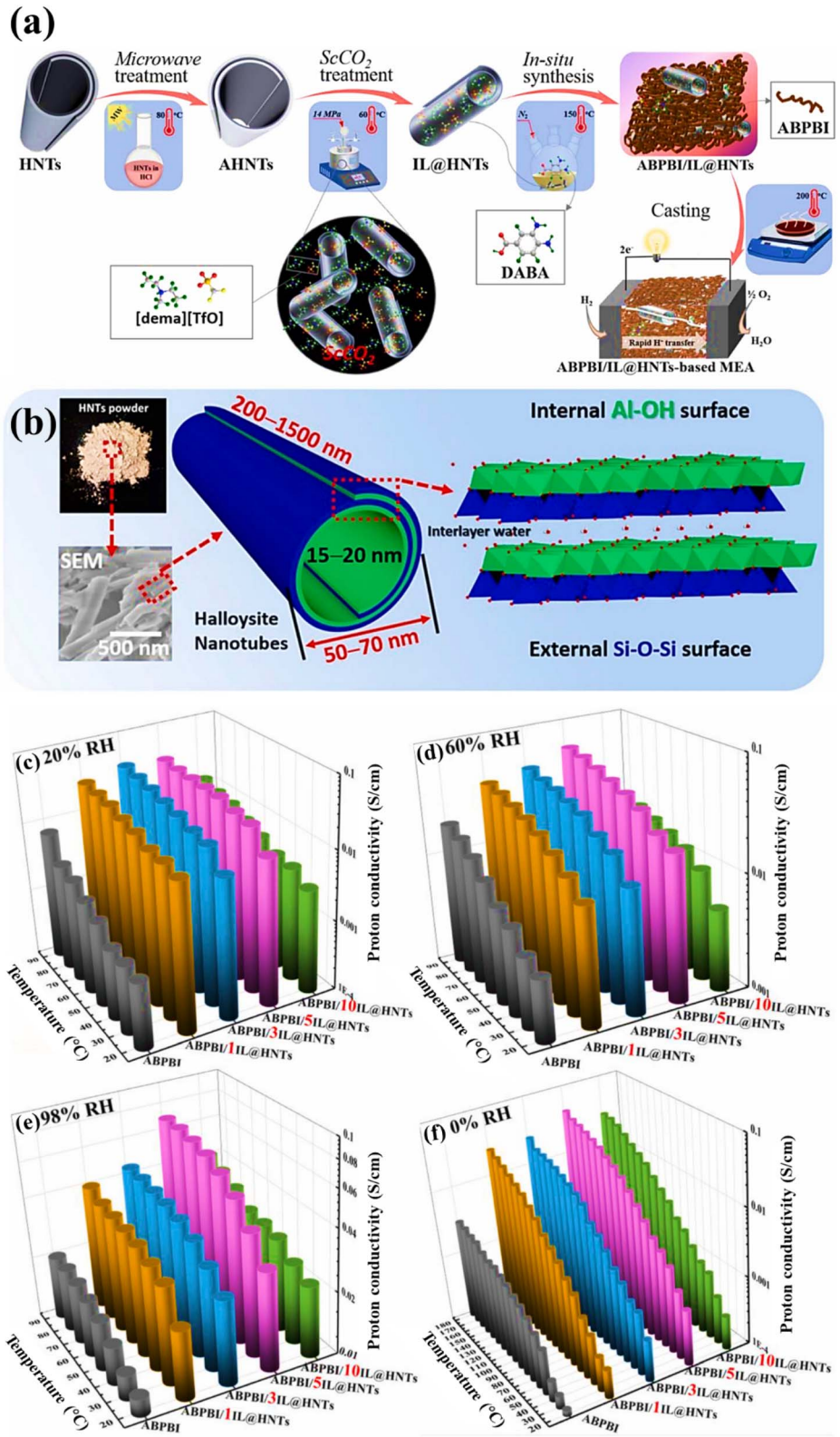

Fig. 11 (a) Schematic representation of IL@HNT and ABPBI/IL@HNT composite membrane preparation, (b) image of HNT powder, SEM image, and structure of HNTs, proton conductivity of PA-ABPBI and PA-ABPBI/IL@HNT membranes at low temperatures (20–90 °C) under (c) 20%, (d) 60%, (e) 98% RH, and (f) low humidity (20–180 °C under 0% RH). Reprinted with permission from ref. 154. Copyright (2023), Elsevier.

a large lumen as the skeleton (Fig. 11b) and $ScCO_2$ to help IL filling, leading to the formation of ionogels with a larger IL loading. The $ScCO_2$-assisted filling led to a high IL loading and maintained the structural integrity of the HNTs, while the ILs were homogeneously dispersed in the lumen of the HNTs in comparison with the conventional methods. This strategy led to the formation of great proton conductivity routes and gave a high performance of composite membranes. The protonic IL ([dema][TfO]), with sufficiently good hydrophilicity, is one of the best ILs with great thermal stability and electrochemical

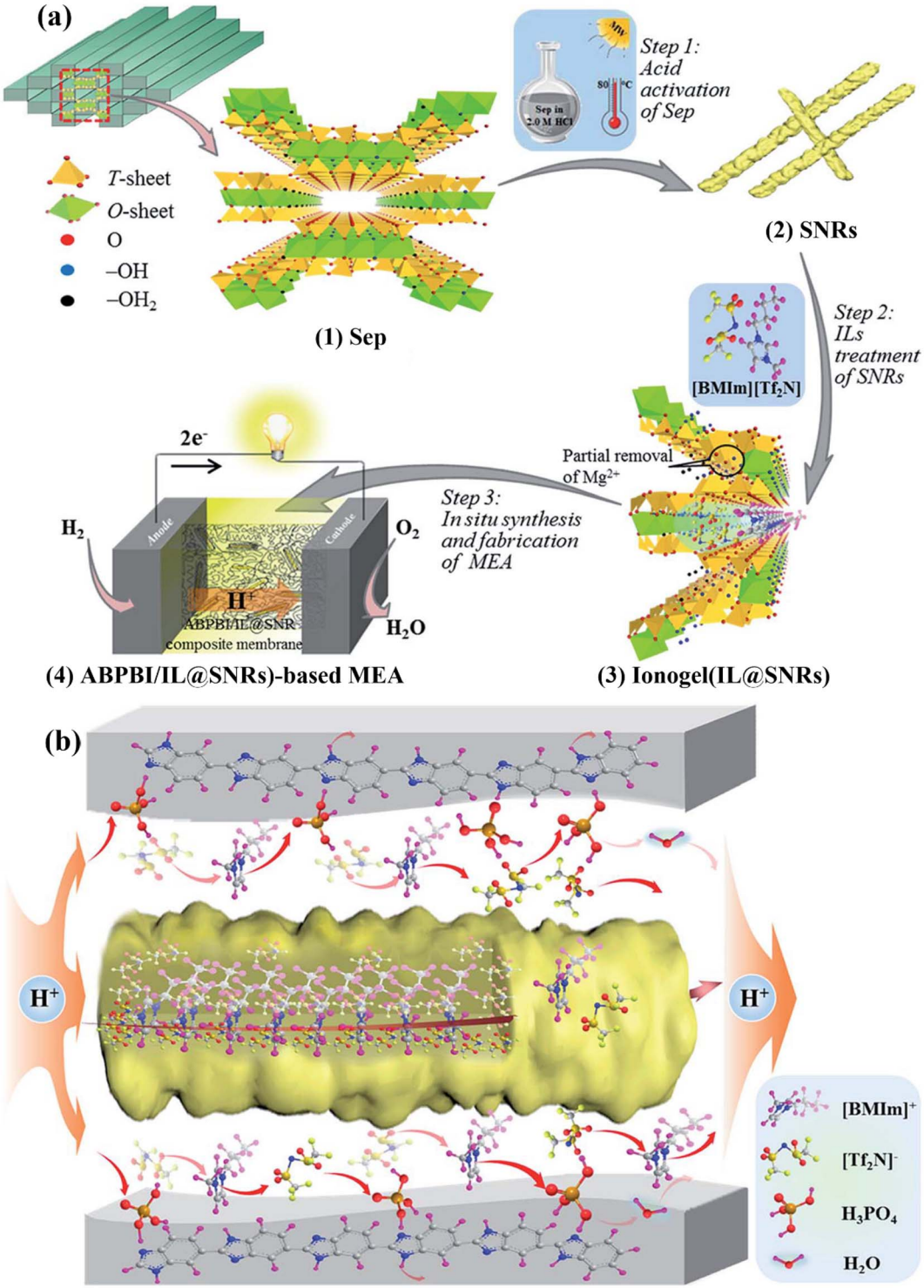

Fig. 12 Schematic images of (a) preparation of IL@SNR ionogel *via* microwave-assisted acid activation treatment and high-vacuum drying upon loading of PA, and its subsequent integration in PEMFCs. (b) Proton conduction pathways in PA-doped ABPBI/IL@SNR membranes. Reprinted with permission from ref. 155. Copyright (2019), The Royal Society of Chemistry.

properties. It was reported that the compatibility of PBI and [dema][TfO] is more than that of other polymers and [dema][TfO] is one of the high-potential ILs for wide-temperature-range PEMFC applications. Fig. 11c–f illustrate the proton conductivity of the ABPBI and ABPBI/IL@HNTs PEMs under different conditions. The proton conductivity of the composite PEMs was higher than that of ABPBI PEM over a wide range of temperatures and RH. By increasing the amount of IL@HNTs, the proton conductivity of the PEMs was improved, and then slightly reduced. This trend was simultaneously observed with the water uptake and PA doping level, indicating that proton carriers, namely, IL@HNTs, PA, and water played an important role in the proton transfer process. The proton conductivity varied from 13 to 71 mS cm^{-1} at 20–90 °C and different RH (20, 60, and 98%). The proton conductivity of 71 and 45 mS cm^{-1} was obtained at 90 °C with 98% RH and 180 °C with 0% RH, respectively. The ABPBI/5IL@HNT PEM exhibited outputs of 219 and 380 mW cm^{-2} at 80 °C and 160 °C with 0% RH (1.9- and 2.1-fold higher than that of PA-doped ABPBI PEM), respectively.

3.3.5 SEP-based (nano)materials

3.3.5.1 Membranes. IL-confined SNR (IL@SNR) ionogels were synthesized for use in PEMFCs at varying temperatures, as shown in Fig. 12a.[155] The natural sepiolite was hydrothermally treated under microwave irradiation to obtain 1D hierarchical porous SNRs. The as-prepared IL@SNRs were incorporated in ABPBI to synthesize ABPBI/IL@SNR membranes. The presence of H_2O in the nanochannels of IL@SNR afforded proton-conducting routes, as shown in Fig. 12b. The highest proton conductivity was observed for the membrane comprised of 5 wt% IL@SNRs in all conditions with a maximum value of 0.048 S cm^{-1} at 180 °C and 0% RH. ABPBI/5IL@SNR exhibited the optimum power density of 0.15 W cm^{-2} (at 80 °C) and 0.28 W cm^{-2} (at 180 °C), with 0% RH. Accordingly, increasing the operating temperature of the fuel cell led to an improvement in its performance, which was attributed to the high mass transfer and proton conductivity at higher working temperatures.

LDH obtained by the coprecipitation method and LDH/SEP nanostructured fillers were applied in the synthesis of SPEEK composite membranes *via* the solution casting method.[156] The fillers improved the water uptake and thermal stability of the SPEEK membrane. Moreover, the presence of SEP clay in the nanostructured filler helped in uniformly dispersing and connecting the filler to the SPEEK matrix. Among the composite membranes, that containing 6% LDH/SEP filler exhibited the best performance. LDH/SEP (6%)/SPEEK in PEMFC was reported to have an activation energy of 20.3 kJ mol^{-1}, water uptake of 20%, and proton conductivity of 93 mS cm^{-1} at 110 °C. PEI-filled SEPNR (PEI@SEPNR)-embedded ABPBI composites (ABPBI/PEI@SEPNR) were *in situ* prepared according to Fig. 13 for enhancing their proton conductivity and minimizing the PA doping. Subsequently, these PEMs were used in PEMFCs over a wide temperature range from room temperature to 200 °C.[157] These PEMs based on embedded PEI@SEPNR prevented the migration and toxicity of PEI oligomers, and also increased the alkalinity and water absorption. These properties led to high proton conductivity at low PA doping levels. The maximum output achieved for the PA-doped ABPBI/5PEI@SEPNR PEM cell was 0.16 and 0.27 W cm^{-2} at 80 °C and 180 °C, respectively, under anhydrous conditions. Also, its output was 2.2 and 1.5-fold greater than that of the PA-doped ABPBI membrane, respectively.

3.3.6 Kaolinite-based (nano)materials

3.3.6.1 Membranes. Silane-modified kaolinite clay (MK) and cross-linked PVA (XPVA) polymer were used to prepare XPVA/MK.[88] The PVA/MK membranes were fabricated *via* a solution

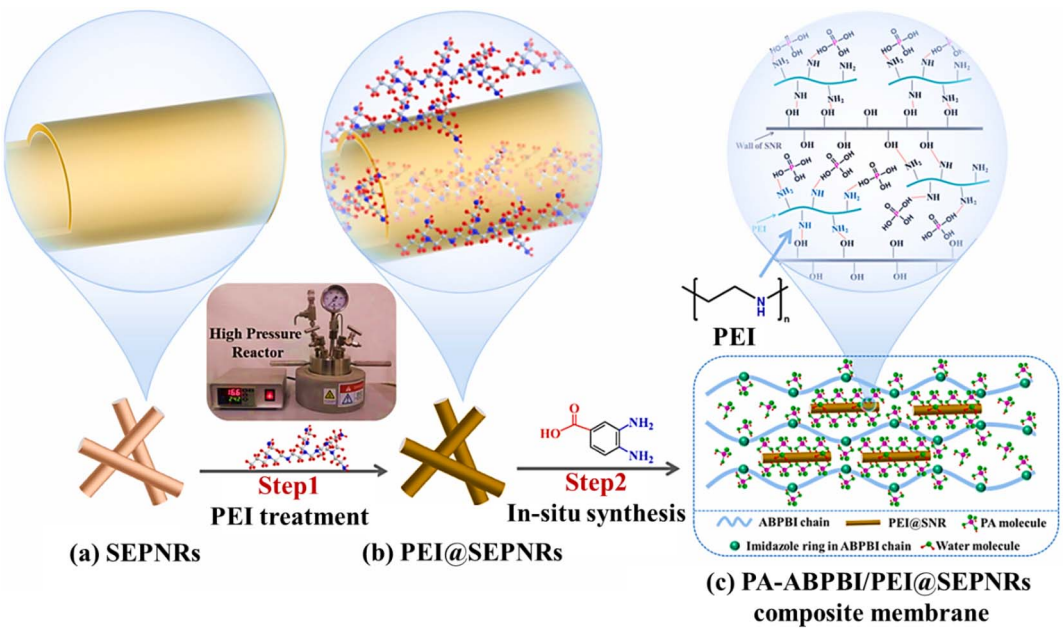

Fig. 13 Schematic illustration of the synthesis of PEI@SEPNR NPs and ABPBI/PEI@SEPNR membranes. Reprinted with permission from ref. 157. Copyright (2022), Elsevier.

casting method. Modified kaolinite NPs (0–20 wt%) were dispersed in distilled water under ultrasonication, and then added to a crosslinked PVA solution. Subsequently, the solution was stirred (3 h) at 50 °C and sonicated (30 min) to ensure the complete dispersion of the NPs. Finally, it was cast on Petri dishes and left at room temperature for 2 days. The phosphorylated PVA/MK was obtained *via* refluxing in PA. Initially, the water uptake decreased with the addition of MK in the range of 2–5 wt%, and then increased when the MK content was increased to 10–15 wt%. The proton conductivity was enhanced by increasing the filler content together with the temperature, resulting in the maximum value of 0.0611 S cm^{-1} at 70 °C with 10 wt% filler content. The ion exchange capacity increased to a maximum value of 1.01 meq. g^{-1} at 20 wt% of filler due to the

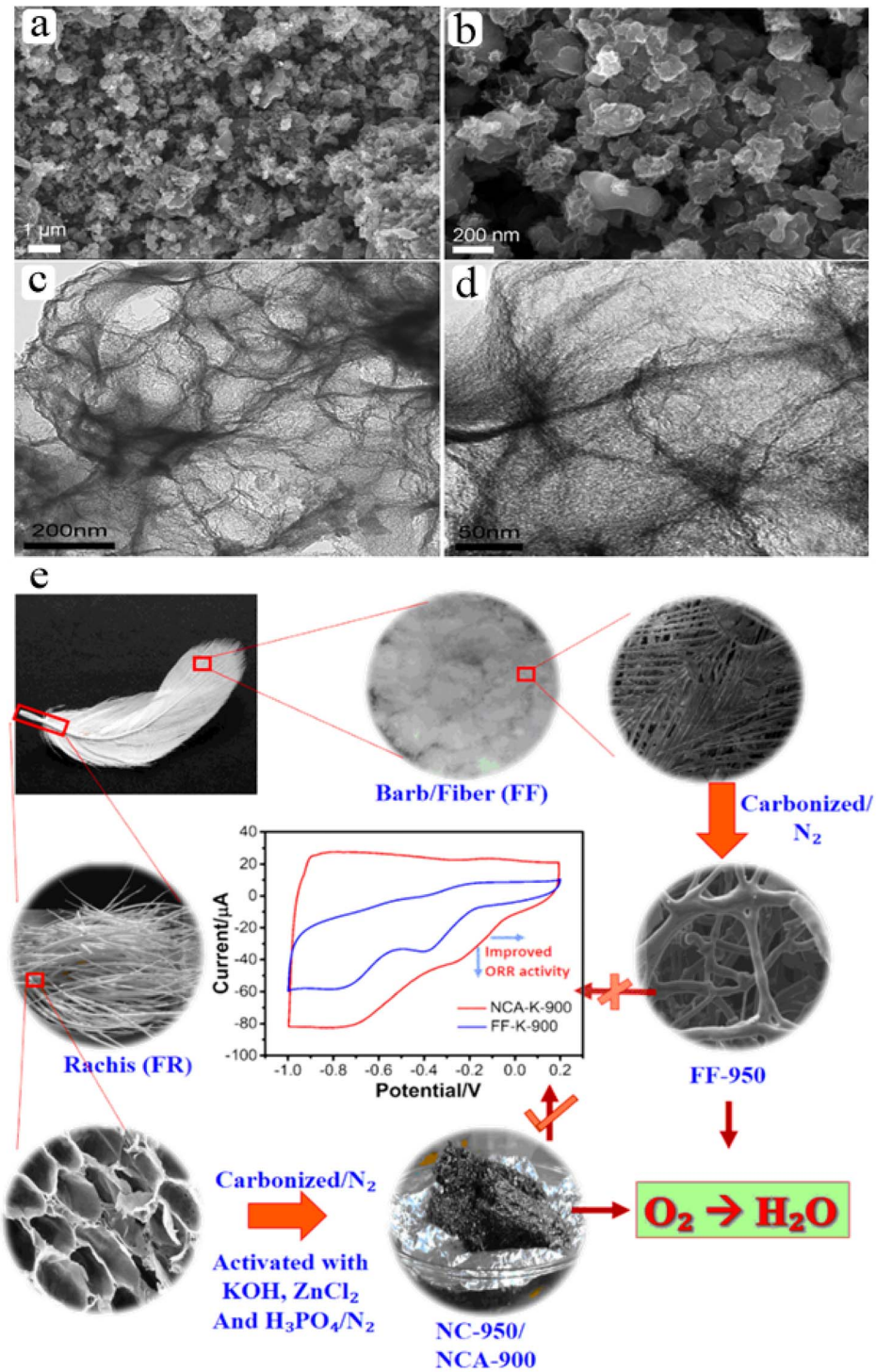

Fig. 14 SEM (a and b) and TEM (c and d) images of NSC-3.5. Reprinted with permission from ref. 159. Copyright (2016), Elsevier. (e) Schematic of the preparation and resulting ORR activity of electrocatalysts from FR and FF. Reprinted with permission from ref. 160. Copyright (2019), Elsevier.

formation of $-PO_3H$ groups in the composite membrane with the least methanol permeability of 2.87×10^{-6} cm^2 s^{-1}.

3.3.7 Biomass-based (nano)materials

3.3.7.1 Membranes. FA is well-known as an affordable inorganic filler material, which is obtained from the activities of coal power plants. It contains aluminum, iron, silicon, calcium, and potassium oxides. Recently, the thermal and mechanical stability of polymeric membranes was improved employing fly ash as an inorganic additive. In addition, it can help to increase the physicochemical properties of electrolyte membranes due to the presence of several metal oxides. Punniakotti and co-workers prepared membranes composed of crosslinked sulfonated PVA (SPVA) and FA as a low-cost inorganic filler *via* the solution casting method.[158] The resultant membrane comprised of 20 wt% of FA (SPVA/FA/20) achieved high water uptake of 88% with the highest ion exchange capacity of 2.98 meq. g^{-1} and the maximum proton conductivity of 0.016 S cm^{-1}. These values were reported to be 68%, 0.95 meq. g^{-1}, and 0.008 S cm^{-1} for pure SPVA, respectively. The results showed that the addition of FA led to considerable improvement in the polymer properties of SPVA for PEMFCs.

3.3.7.2 Catalysts. Nitrogen and sulfur co-doped bio-carbon flocs (NSC) were acquired by thermal decomposition of a zinc-based metal–organic coordination polymer (MOCP-Zn), which was fabricated *via* the hydrothermal reaction between zinc salt and chicken feather-derived polypeptides.[159] The polypeptides were synthesized using chicken feathers in three steps. Initially, the chicken feathers were washed using acetone solution and dried at 110 °C, and subsequently, they were placed in an autoclave with aqueous ammonia at 150 °C for 3 h. Consequently, the chicken feathers were degraded into polypeptides. Finally, the ammonia solution containing the polypeptides was dried at 110 °C and milled into a powder. The morphology of the NSC-3.5 catalyst (3.5 indicates the pH value of the powder precursor during its synthesis) is presented in the SEM and TEM images in Fig. 14. The NPs of the resultant bio-carbon are shown in Fig. 14a and b, while Fig. 14c and d display the curly porous graphene-like carbon flocs. The NSC catalyst demonstrated great potential for application in PEMFCs due to its high electrocatalytic activity for the ORR under alkaline and acid conditions. According to the LSV results, the NSC-3.5 catalyst was the best with a larger diffusion-limited current density than that of Pt/C and high ORR kinetic current density in the range of 5.89–8.11 mA cm^{-2} in the potential range of 0.3–0 V. The CV of NSC-3.5 indicated its supreme stability without a decline in current in acidic medium but Pt/C retained a lower current of 57.8%. Another report demonstrated chicken FR as a new precursor to synthesize ORR electrocatalysts for PEMFC application (Fig. 14e).[160] KOH-activated NCA-900 (NCA-K-900) presented the best electrochemical activity with regard to onset potential (−0.02 V *vs.* Ag/AgCl) and current of 57.6 μA in O_2-saturated 0.1 M KOH solution due to its extremely porous structure and highest surface area. It exhibited great current stability with a decrease of 4% after 15 h.

Orange peel was utilized as a precursor to prepare AC (OP-AC) *via* chemical activation using H_3PO_4 by Dhelipan and co-workers in 2017.[161] Fig. 15a schematically shows the preparation of OP-AC. A chemical reduction process was performed to

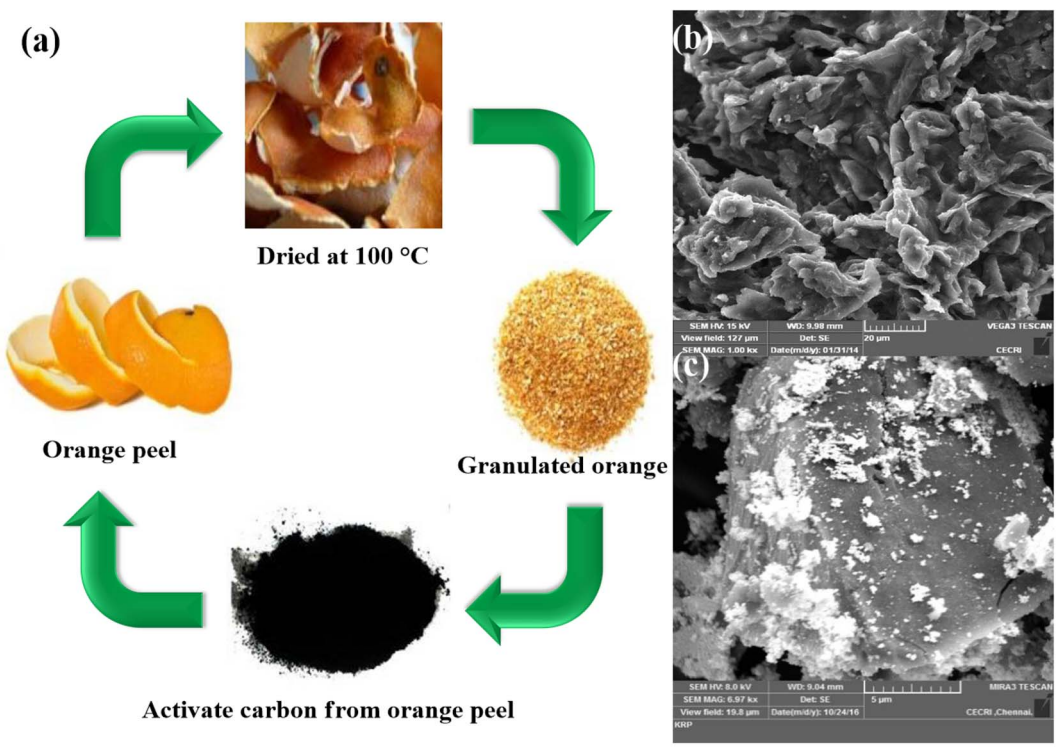

Fig. 15 (a) Fabrication of OP-AC and SEM micrographs of (b) OP-AC and (c) Pt/OP-AC. Reprinted with permission from ref. 161. Copyright (2017), Elsevier.

Table 1 Performance and properties of nature-based composite membranes in the field of PEMFCs

Membrane	Natural material	Proton conductivity	Water uptake	Maximum power density	Temperature	Ref.
Nafion/MMT	MMT	4.03 mS cm^{-1}	—	—	—	162
Poly(4,4′-diphenylether-5,5′-bibenzimidazole) (OPBI)/MMT	MMT	Higher than OPBI	—	—	30–160 °C	163
Nafion/modified Wyoming MMT (SWy-2)	MMT	—	50 wt%	—	20–130 °C	164
Sulfonated MMT/SPSU-BP/PTFE	Na^+–MMT	0.073 S cm^{-1}	Higher than SPSU-BP	—	90 °C	165
Nafion-sulfonated SEP	SEP	Close to Nafion	38 wt%	50% more than Nafion	100 °C	166
ABPBI/sulfonated SEP	SEP	0.075 S cm^{-1}	35.36%	0.23 W cm^{-2}	180 °C	167
MF-4SC-Pd/HNT	HNT	Higher than MF-4SC-Pt/HNT	—	—	—	168
SPEEK/SiO_2–MMT	Sodium Wyoming MMT	0.158 S cm^{-1}	23%	—	120 °C	85
Aquivion/SEP	SEP	Higher than Aquivion®	70%	—	80 °C	169
SPEEK-PhetaTfO-intercalated MMT (MMTPheta)	MMT	0.2 mS cm^{-1}	—	—	30–230 °C	170
PA-doped ABPBI–MMT/sulfonated PVA	MMT	0.157 S cm^{-1}	53%	1100 mW cm^{-2}	140 °C	171

deposit Pt on OP-AC. The change in the morphology of OP-AC and Pt/OP-AC can easily be perceived in Fig. 15b and c. The efficiency of the resultant Pt/OP-AC electrocatalyst in PEMFCs was investigated and the results indicated that Pt/OP-AC, with an electroactive surface area of 17.8 m^2 g^{-1}, had an acceptable performance as a catalyst support for the ORR. The power density of Pt/OP-AC as a cathode electrode in the fuel cell test was 19 mW cm^{-2} with O_2 and H_2 flow rates of 1000 mL min^{-1} at 60 °C.

Tables 1 and 2 summarize the works on nature-based composite membranes and catalysts in PEMFC applications, respectively.

3.4 Nature-inspired materials as membrane or catalysts for DMFCs

3.4.1 Aluminosilicate-based (nano)materials

3.4.1.1 Membranes. Tricoli and Nannetti employed the molecular sieving attributes of two natural zeolites (clinoptilolite and chabazite) to form ion-conducting membranes that performed selective hydrogen ion transportation over methanol molecules.[178] The ion-conducting membranes containing Nafion as a polymer matrix and clinoptilolite or chabazite as fillers with different contents were fabricated by dispersing fine zeolite crystals in a Nafion solution and vaporizing the solvents from the suspensions in a vacuum oven at 80 °C. The obtained membranes were converted into the H^+ or Na^+-form using H_2SO_4 solution (pH > 3) and 1 N Na_2SO_4 solution (pH 3.4), respectively. All the membranes had lower ion conductivity than the zeolite-free recast Nafion and the conductivity values of the Na^+-form membranes were higher than that of the H^+-form in the range of 22–60 °C. The results showed that the addition of zeolite fillers led to remarkable changes in conductivity, permeability, and selectivity compared with the Nafion membrane. The fillers decreased the selectivity of the Nafion membrane by about 5 times. Therefore, this is an effective method to form favorable composite materials for use in DMFCs. Nafion–clinoptilolite and Nafion–chabazite composite membranes were used to promote the performance of DMFCs at high temperatures.[179] The membranes were prepared with 3 and 6 vol% of zeolite and treated in H_2SO_4 solution (pH > 3) and tested in a DMFC operated in the temperature range of 90–140 °C. The maximum power density of the membranes with 3 and 6 vol% zeolite fillers was 350–370 mW cm^{-2} and 200–210 mW cm^{-2} under oxygen and air feeds at 140 °C, respectively. In comparison to the bare Nafion membrane, the composite membranes showed higher proton conductivity at elevated temperatures (close to 150 °C) due to the increased water retention ability by the hygroscopic filler.

HNTs consisting of sulfonate polyelectrolyte brushes (SHNTs) were created through distillation–precipitation polymerization, and then incorporated in the CS matrix.[180] The mechanical properties of the membrane with SHNTs were improved compared with CS and CS/HNTs, where the tensile strength and Young's modulus were 52.8 and 942.8 MPa when CS was filled with 9% SHNTs, respectively. The water uptake of CS, CS/HNT-9, and CS/SHNT-9 was found to be 58.1%, 49.7%, and 48.4%, respectively. It is worth noting that water uptake was reduced with an increase in the nanotube filler content. The proton conductivity of CS was ~0.0117 S cm^{-1}, whereas it was reduced with the addition of the nanotube fillers. However, CS/SHNTs displayed better ionic conductivity at 25 °C. In addition, the temperature-dependent conductivity measurement exhibited that the maximum conductivity of 0.0422 S cm^{-1} was achieved at 80 °C for CS/SHNT-15. The methanol permeability of the synthesized membrane was lower than that of the Nafion membrane. By adding SHNTs to the CS matrix, the methanol

Table 2 Performance of nature-based catalysts in the PEMFC applications

Composite	Natural material	Maximum power density/ current density of fuel cell	Performance	Ref.
Ru/HNTs	HNTs	—	Good ammonia conversion with 5.6 wt% Ru Complete decomposition of ammonia at >600 °C	172
Pt/PGS@nitrogen-doped graphitic layer	PGS	—	ECSA of 32.3 $m^2 g^{-1}$ Mass activity of 68.7 mA mg^{-1} Pt Better catalytic activity toward ORR compared with Pt/C Better stability compared with Pt/C	93
Pt/mesoporous carbon	Mushroom	—	ECSA of 62 $m^2 g^{-1}$ Onset potential of 0.91 V Tafel slope of 60 mV dec^{-1} Higher durability than Pt/C Specific activity of 0.0129 mA cm^{-2}	173
Nitrogen and cobalt dual-doped sponge-like carbon (CoNASS)	Soybean straw	—	High specific surface area of 1185 $m^2 g^{-1}$ Excellent ORR activity with a half-wave potential of 0.786 V, comparable with Pt/C Limiting diffusion current density of 5.8 mA cm^{-2}	174
Mesoporous activated NC heated at 900 °C	Chicken feather	—	More positive onset potential (−0.02 V) compared with heated samples at 500 and 700 °C Having higher ORR current density (1.7 mA cm^{-2}) compared with heated samples at 500 and 700 °C	175
Nitrogen-fluorine-doped carbon	Pomegranate peel	65 mW cm^{-2}/145 mA cm^{-2}	Mass activity of 86.6 mA mg^{-1} in alkaline media Mass activity of 2.3 mA mg^{-1} in acidic media Kinetic current density of 43.3 mA cm^{-2} in alkaline media Kinetic current density of 1.15 mA cm^{-2} in acidic media Superior electrocatalytic activity toward ORR in comparison with Pt/C Good stability in both alkaline and acidic media	176
Pt/C/Nafion/zeolite	Zeolite	0.5 A cm^{-2}	More stable performance in comparison to catalysts without zeolite Best cell performance at 60 °C	177

permeability of CS/SHNTs was reduced in comparison with the CS/HNTs membrane.

3.4.1.2 Catalysts. Novel graphene-based electrocatalysts, Fe^{3+} doped-natural zeolite (Fe^{3+}–clinoptilolite)/GO and MoS_2@NG were introduced by Beheshti Marnani and co-workers.[181] The electrocatalysts were synthesized by dispersing clinoptilolite in 40 mL of 0.5 M $FeCl_3 \cdot 6H_2O$ solution. Subsequently, HNO_3 solution was added and magnetically stirred at

room temperature for 24 h. Finally, it was dried at 100 °C for 24 h. The nanocomposite was made by mixing GO and Fe^{3+}–clinoptilolite under ultrasonic irradiation. The methanol oxidation of Fe^{3+}–clinoptilolite/GO in alkaline media at different scan rates demonstrated that the optimum anodic current of 61.24 μA was achieved at a scan rate of 0.06 V s^{-1}.

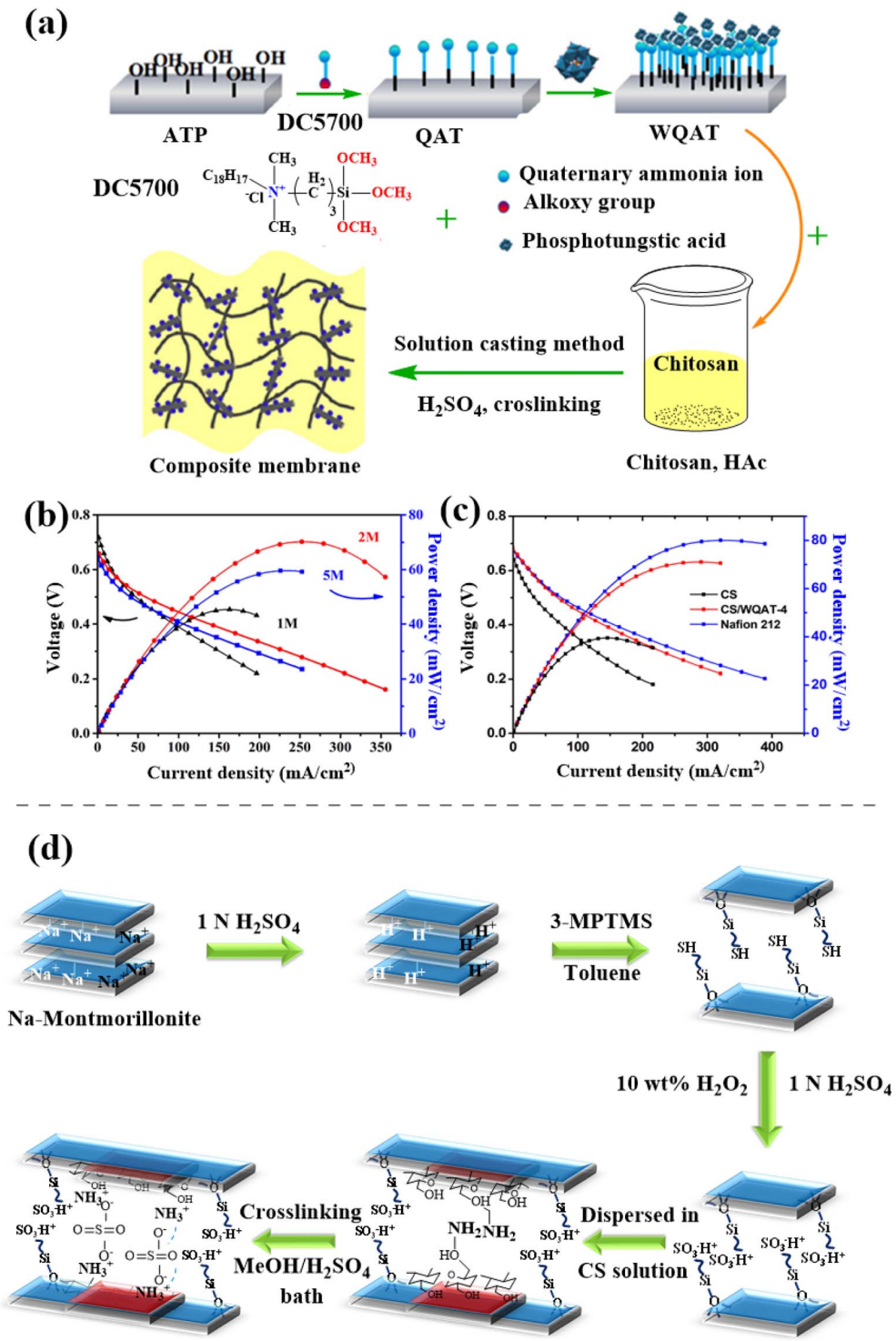

Fig. 16 Schematic of (a) fabrication process of WQAT and CS/WQAT-*x* composite membranes, (b) polarization and power density curves of DMFC tests of CS/WQAT-4 composite membrane in different methanol concentrations, and (c) different PEMs at 70 °C with 2 M methanol solution as the anode fuel. Reprinted with permission from ref. 182. Copyright (2020), MDPI. (d) Functionalization of CS-MMT and Na-MMT membrane by ionic cross-linking with sulfuric acid, showing CS chain with negatively charged sulfuric acid $-(SO_4)^{2-}$ and positively charged $-(NH_3)^+$ ionic interaction together with sulfonyl functionality of Na-MMT. Reprinted with permission from ref. 188. Copyright (2015), the American Chemical Society.

Additionally, MoS_2@NG with a nanosheet structure was employed as a catalyst toward the ORR, suggesting that the catalytic activity of MoS_2@NG was better than that of MoS_2@GO, which was probably due to the weak electron transfer kinetics of MoS_2@GO. Therefore, MoS_2@NG and Fe^{3+}–clinoptilolite/GO can be used as cost-efficient catalysts to design DMFCs.

3.4.2. PGS (ATP)-based (nano)materials

3.4.2.1 Membranes. Natural 1D ATP was loaded on PWA to synthesize a nanofiller (WQAT) for the CS polymer matrix and form PEMs (Fig. 16a) for DMFCs in 2020.[182] The obtained CS/WQAT membrane with 4 wt% WQAT (CS/WQAT-4) showed the higher utilization efficiency than the pristine CS with the proton conductivity of 35.3 mS cm^{-1} (31.8% higher than CS) at 80 °C (Fig. 16b). As depicted in Fig. 16c, a power density of 70.26 mW cm^{-2} (~1.7-times that of pristine CS) was obtained for the CS/WQAT-4 membrane in the presence of 2 M methanol as anode fuel at 70 °C. This membrane also exhibited the highest tensile strength of 58.65 MPa, maximum water uptake, and minimum methanol permeability.

3.4.3 MMT-based (nano)materials

3.4.3.1 Membranes. The synthesis of organic/inorganic composites was reported using SPEEK and OMMT for DMFC application in 2005.[183] Initially, OMMT was modified *via* the ion exchange reaction between alkylammonium cations and metal cations to obtain organophilic OMMT, and then the SPEEK/OMMT membranes were fabricated by the solution intercalation method. The resultant composite membranes displayed constant water uptake up to 80 °C. The incorporated OMMT layers in the polymer matrix hindered extreme swelling of the membranes. The high conductivity of 1.2×10^{-2} S cm^{-1} was reported for the membrane with 5 wt% OMMT at 90 °C, which is close to that of Nafion® 115. The activation energy of this membrane reached 32.08 kJ mol^{-1}. The methanol permeability of the membranes decreased due to the incorporation of nanosized OMMT, preventing the migration of methanol. Modification of MMT by Zonyl FSD and quaternized PFPE–NR_3 was performed to utilize it as a filler for the improvement of the properties of the Nafion® 117 membrane.[184] Also, two membranes were prepared with native sodium MMT (native MMT) and MMT modified by alkyl ammonium cations (MMT 25A). The membrane containing MMT–PFPE–NR_3 showed a decrease in methanol permeability of ~20%, while the permeability increased for the native MMT, MMT-Zonyl, and MMT 25A. Besides, the ionic conductivity of the MMT–PFPE–NR_3 membrane increased and the best conductivity was observed for the membrane with 2 wt% MMT–PFPE–NR_3. The native MMT and MMT–PFPE–NR_3 membranes were tested in a small fuel cell at room temperature, 60 and 80 °C. At room temperature, the fillers did not influence the performance of the fuel cells. Furthermore, the native MMT had a negative effect on the performance of the fuel cell at 60 and 80 °C. According to the results, the MMT–PFPE–NR_3 membrane significantly improved the performance of the cells at 60 and 80 °C due to the improvement in the conductivity/permeability ratio and water retention of Nafion at high temperatures. PBI/MMT nanocomposite membranes were synthesized *via* the organic modification of MMT and an organosoluble, fluorine-containing PBI.[185] The membranes were immersed in 11 M PA solution. The results revealed that the thermo-oxidative stability of the PBI membranes improved, while the CTE of the PBI membranes decreased by 30% with an increase in m-MMT content. In addition, the tensile modulus of the PBI/m-MMT membranes became better and the highest tensile modulus was obtained for the PBI/5 wt% m-MMT membrane (41% higher than pure PBI membrane). Utilizing m-MMT in membranes resulted in a decrease in methanol permeability, which was found to be ~81% for the PBI/5 wt% m-MMT membrane (6.2×10^{-9} cm^2 s^{-1}). Although, the proton conductivity of the nanocomposite membranes was lower than that of the acid-doped pure PBI (21–27%), it was negligible in comparison with the improvement in methanol permeability and mechanical properties of the nanocomposite membranes. Hence, PBI/m-MMT nanocomposite membranes can be employed as PEMs in DMFCs. A PVA/MMT/PSSA was fabricated *via* the solution casting method.[186] Initially, MMT clays and PSSA polymer were blended under ambient conditions and dried at 100 °C for 48 h. The m-MMT and PSSA polymer as two proton sources led to improved ionic conductivity. The methanol permeability and ionic conductivity of the prepared composite membranes were in the order of 10^{-7} cm^2 s^{-1} and 10^{-3} S cm^{-1}, at room temperature, respectively. The fuel cell performance was examined in different methanol concentrations of 1, 2, and 4 M at an operating temperature of 25 °C. The DMFC utilizing the PVA/20 wt% MMT/10 wt% PSSA composite membrane showed a power density of 20 mW cm^{-2} at 25 °C in 2 M methanol, which was 2.4-times that of the Nafion® 117 membrane. AMPS, DMDOC, and SA could also be used to modify MMT.[86] The m-MMTs were incorporated as fillers in the SPEEK matrix for application in PEMFCs. The DMDO-MMT membrane demonstrated higher conductivity at 80 °C than the other membranes. The hydrolytic stability of the AMPS-MMT and SA-MMT membranes increased. The water absorption and ion exchange values of the composite membranes were greater than that of the pristine SPEEK membranes. Lower proton conductivity was reported for the AMPS-MMT and SA-MMT membranes compared to the pure membrane. MMT was modified using BTA and employed to fabricate a nanocomposite based on Nafion® as a PEM for DMFCs.[187] The membranes based on unmodified MMT (Cloisite™ Na) and Cloisite™ 15A were prepared. The methanol permeability and proton conductivity of the membranes were reduced with an increase in the nanoclay content due to the increase in path length for proton transfer and diffusive routes against fuel molecules in the polymer matrix. In addition, the proton conductivity of the membrane increased by increasing the temperature from 25 to 90 °C. However, the intrinsic proton conductivity of the BTA groups present in the Nafion/BTA-MMT membrane enhanced the proton transfer compared to other membranes. According to the direct methanol single fuel cell tests, the Nafion/BTA-MMT membrane with 3 wt% BTA-MMT outperformed Nafion® 117 in 5 M methanol at 70 °C with a high power density of 144 mW cm^{-2}, which was over 3-fold that of Nafion® 117 (39 mW cm^{-2}). It is worth mentioning that

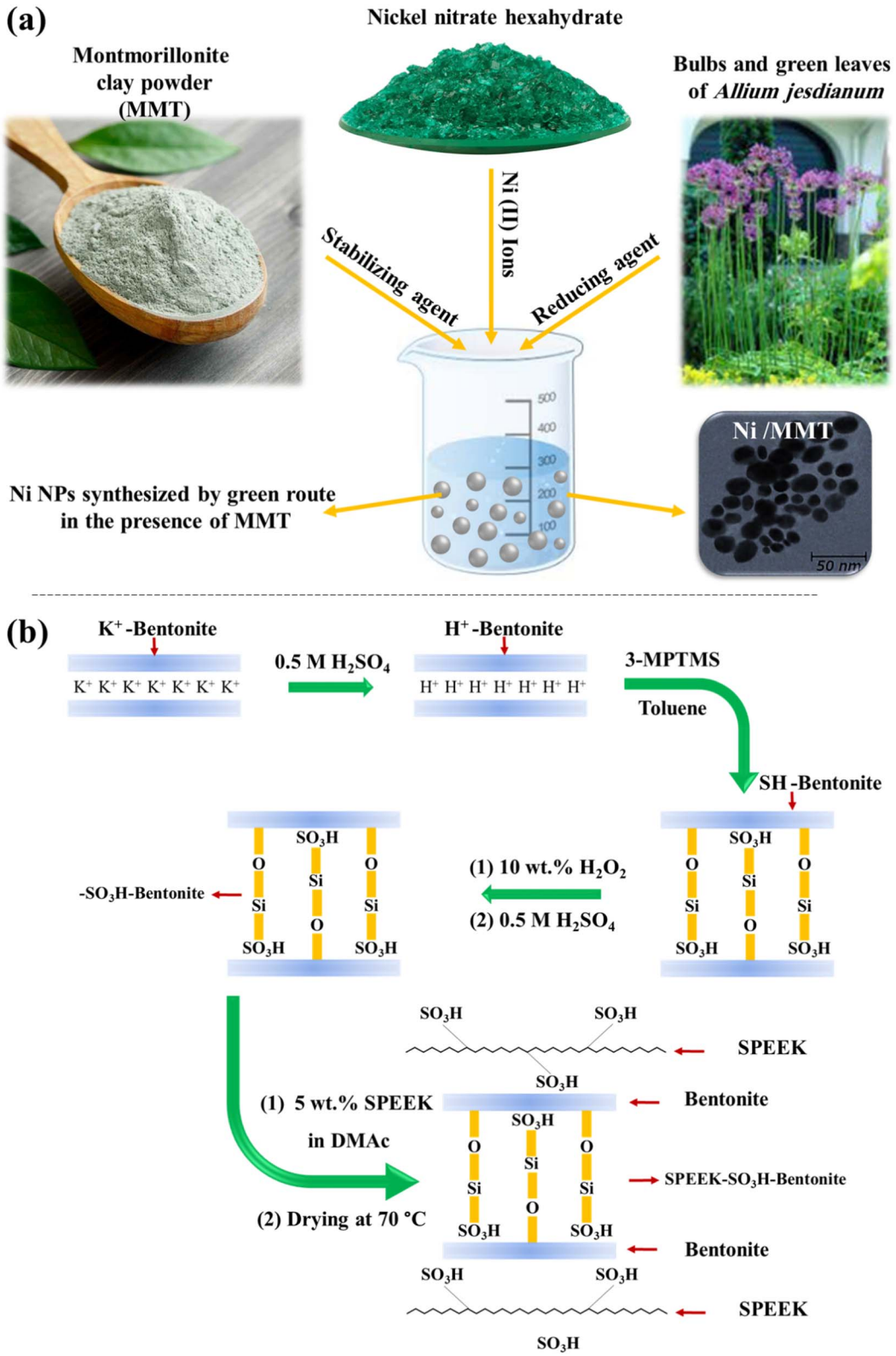

Fig. 17 (a) Schematic representation of Ni/MMT synthesis by a green method. Reprinted with permission from ref. 189. Copyright (2020), Elsevier. (b) Schematic representation of BEN functionalization through silane condensation and interaction of SPEEK–HSO_3–BEN composite. Reprinted with permission from ref. 87. Copyright (2014), Elsevier.

the fuel cell performance in 5 M was better than that in 1 M methanol. A strategy for the synthesis of an efficient proton-selective PEM for DMFCs was suggested *via* the combination of naturally abundant materials (a polysaccharide and clay) with green modification methods.[188] CS and sodium-MMT (Na-MMT) were functionalized to form sulfonated natural nanocomposite PEMs (CS-MMT), as shown in Fig. 16d. The membranes were fabricated with different weight percent of MMT and tested in different methanol concentrations at 60 °C. The synthesized membrane displayed high potential in terms of proton conductivity (4.92×10^{-2} S cm^{-1}) and power density (45 mW cm^{-2}) with a limiting current density of <100 mA cm^{-2}. Among them, CS-MMT 3% demonstrated the best performance. An MMT loading over 3% led to its aggregation and inhomogeneous distribution. Also, the membrane exhibited greater stability and better performance in higher methanol concentration feeds.

Another work suggested the preparation of Ni NPs/MMT using the water extract of a native Iranian plant (*Allium jesdianum*) in the presence of MMT as a support.[189] The synthesis of the Ni/MMT nanocomposite was performed using a green process with the *Allium jesdianum* water extract, as shown in Fig. 17a. The CV studies of the modified CPE were performed in NaOH solution and the highest electrochemical performance was reported for the Ni/MMT-CPE containing 30% of modifier in comparison with MMT-CPE and pure CPE. Afterward, the methanol oxidation was evaluated in alkaline and acidic media. Catalysis of methanol oxidation was observed at a potential of 0.6 V and 0.3 V in alkaline and acidic media, respectively. Besides, Ni/MMT-CPE displayed better catalytic activity toward methanol oxidation compared with the unmodified CPE and MMT-CPE, which was due to the formation of NiOOH species.

3.4.4 BOT-based (nano)materials

3.4.4.1 Membranes. The high surface area and hydrophobic property of BOT were utilized to fabricate a doped Nafion® membrane.[190] BOT was modified with dodecylamine *via* the sol–gel method to fabricate a Nafion®/SiO_2/m-BOT composite membrane, in which SiO_2 and m-BOT were employed to improve the water absorbance and methanol permeability and control the proton channel size. Compared to the Nafion® membrane, the composite membrane had lower methanol permeability (20.40%) and proton conductivity of 6.67×10^{-2}, which was 9.91×10^{-2} S cm^{-1} for Nafion®. The performance of the fuel cell at the operating temperature of 30 °C using the composite membrane was lower than that with the Nafion® membrane. The performance of the DMFC was enhanced using the composite membrane with a high power density of 135.17 mW cm^{-2} at 55 °C in 1.5 M methanol compared to that of 118.7 mW cm^{-2} for Nafion®. Moreover, the effect of methanol concentration on the fuel cell output power was evaluated. The peak power density of the Nafion® membrane was strongly reduced in high concentrations of methanol. However, the performance of the fuel cell consisting of the composite membrane was not reduced significantly. In another work, the synthesis of a composite membrane including functionalized potassium–BOT (K^+–BOT) and SPEEK was suggested.[87] During the functionalization process of BOT, H^+–BOT and HSO_3–BOT were produced (as shown in Fig. 17b), which were then used for the preparation of SPEEK–K^+–BOT, SPEEK–H^+–BOT, and SPEEK–HSO_3–BOT polymer electrolyte membranes in DMFCs, respectively. In comparison with the composite membranes containing H^+–BOT or K^+–BOT, the SPEEK–HSO_3–BOT composite membrane displayed the highest tensile strength (12.4 MPa) but the lowest water and water–methanol mixture sorption due to the presence of organo-sulfonic acid groups. The proton conductivity at 70 °C for the SPEEK–HSO_3–BOT composite membrane (121 mS cm^{-1}) was greater than that of other composite membranes and pristine SPEEK membrane (49 mS cm^{-1}). The SPEEK–HSO_3–BOT composite membrane had the lowest methanol permeability (1.93×10^{-7} cm^2 s^{-1}) among the synthesized membranes. The DMFC performance investigation indicated that modification of BOT by silane condensation provides an excellent fuel cell performance, where the peak power density for the DMFCs containing the SPEEK–HSO_3–BOT and pristine SPEEK membranes were reported to be 140 mW cm^{-2} (at 70 °C) and 71 mW cm^{-2}, respectively.

The preparation of nanocomposites using alpha-$Ni(OH)_2$ NPs and BOT clay *via* a vacuum drying process at room temperature (BNi-vac) or by freeze-drying (BNi-lyo) led to an appropriate catalyst for the electrode of DMFCs.[191] The methanol oxidation ability of the as-prepared nanocomposites was evaluated in different methanol concentrations. It was observed that the current density was enhanced with an increase in methanol concentration from 1 to 3 mol L^{-1}. The maximum current density of 37 mA cm^{-2} was obtained for the BNi-lyo catalyst, which was 2.6-times better than that of the BNi-vac catalyst. Hence, BNi-lyo can be employed as a catalyst for methanol oxidation in DMFCs. Furthermore, the BOT-intercalated HDTA-B surfactant in the SPEEK matrix with different weight ratios resulted in the formation of highly efficient SPEEK/HDTA-B nanocomposite membranes for DMFCs.[192] The highest proton conductivity (119 mS cm^{-1} at 70 °C) and tensile strength (25.8 MPa) were observed for the SPEEK/HDTA-B membrane. However, SPEEK/HDTA-B had the lowest methanol permeability of 1.64×10^{-7} cm^2 s^{-1} compared with that of SPEEK/BOT and pristine SPEEK. The fuel cell performance investigation revealed that the power density of the SPEEK/HDTA-B membrane with the weight ratio of 80 : 20 (153 mW cm^{-2}) was higher than that of the pristine SPEEK membrane (73 mW cm^{-2}) at 70 °C. The stability test was carried out for pristine SPEEK and the synthesized membranes at 70 °C for 50 h, indicating that SPEEK/HDTA-B has better stability and lower degradation. BOT could be applied to boost the electrolyte of DMFCs by preparing an SnO_2/sulfonated BOT (sBH)/SPEEK composite membrane *via* magnetic stirring.[193] The water uptake increased from 18.2% to 50.34% by the introduction of 3 wt% SnO_2/sBH into SPEEK, whereas it reached 25.05% and 45.01% with the incorporation of BH and sBH in SPEEK, respectively. The ionic conductivity of SPEEK was reported to be 54.34 mS cm^{-1}, which was reduced to 50.7 mS cm^{-1} with the integration of BH. However, it was enhanced in the presence of sBH and SnO_2/sBH in the SPEEK polymer, and the optimal ionic conductivity value (92.01 mS cm^{-1}) was obtained for the SPEEK/sBH/SnO_2 (3 wt%) membrane at 80 °C. The bond strength of the

hydroxyl groups was diminished due to the strong covalency between the Sn and O in SnO_2, increasing the dissociation of ions. The methanol permeability of SPEEK was limited to 1.28 $\times$ 10^{-7} cm^2 s^{-1} by the addition of SnO_2/sBH to SPEEK. The performance of the DMFCs with pristine SPEEK and SPEEK/sBH/SnO_2 (3 wt%) was examined at 80 °C in 2 M methanol. The maximum output of 118 mW cm^{-2} was reported for SPEEK/sBH/SnO_2 (3 wt%) at the current density of 570 mA cm^{-2} with better ionic conductivity due to the presence of –SO_3H moieties, the large surface area of BH and water molecules of SnO_2 as well as lower methanol permeability, providing the best fuel cell performance for SPEEK/sBH/SnO_2 (3 wt%).

3.4.5 Biomass-based (nano)materials

3.4.5.1 Membranes. Nafion/eggshell composite membranes were formed *via* the solvent-casting method, and then utilized in a DMFC as the electrolyte.[194] Although the tensile strength of the composite with 3 wt% eggshell powder filler (8.22 MPa) was lower than that of Nafion® 117 (31.29 MPa), its Young's modulus (246.942 MPa) was higher than that of Nafion® 117 (127.559 MPa). Also, its water uptake and proton conductivity were 87.27% and 0.2414 S cm^{-1}, respectively, which were higher than that of Nafion® 117. The hydrophilicity and increased water retention in the matrix provided good proton conductivity. Moreover, the hygroscopic nature of the carbonate particles in the synthesized membrane caused higher methanol permeability. Given that the eggshell created more channels for the diffusion of methanol in the composite, the methanol permeability of the Nafion®/eggshell (3 wt%) was 8.40 $\times$ 10^{-7} cm^2 s^{-1}, which was higher than that of Nafion® 117 (8.66 $\times$ 10^{-7} cm^2 s^{-1}). However, the Nafion® matrix had higher methanol permeability than that of Nafion®/eggshell (5 wt%). The passive DMFC single-cell performance test showed that the power density of the composite membrane with 3 wt% filler was 19.34 mW cm^{-2}.

Cost-effective RHA was reported as a filler for the synthesis of SPI composite membranes (SPI-RHA) for DMFC application.[195] The SPI-RHA membrane outperformed pure SPI in terms of its highest ion exchange capacity of 0.2829 mmol g^{-1}, proton conductivity as high as 0.2058 S cm^{-1}, high water uptake of 55.24%, methanol permeability of 0.069 $\times$ 10^{-6} cm^2 s^{-1} and maximum power density of 13.0 mW cm^{-2} (at room temperature using 2 M methanol).

3.4.5.2 Catalysts. A simple one-step method to synthesize a macroporous silver network was recommended using ESM as a template for DMFC application.[196] MOR was studied for a macroporous Ag network and traditional Ag mirror. The electrocatalytic performance of the catalysts was studied using CV tests in 2 M methanol + 0.25 M H_2SO_4 and melting [MIm][Tfo] at room temperature and 50–250 °C. The peak current density of methanol oxidation was *ca.* 0.25 V for the Ag network, which was 2.67-times that of the Ag mirror at room temperature. The Ag network presented an extremely high electrocatalytic performance, which was 3.27-times higher at 250 °C than that at 50 °C. Therefore, the as-prepared catalyst is suitable for application in high-temperature DMFCs. Similarly, eggshell was utilized as a template to fabricate a stable anode catalyst through *in situ* polymerization for the synthesis of network-structured PANi and PPy-supported Pt and Ag catalysts on a template.[197] The use of ESM networks as a support led to the formation of pliable catalysts, which curved easily. The electrocatalytic activity of the catalysts was studied by CV tests in 2 M methanol and 0.25 M H_2SO_4 aqueous solution at room temperature (25 °C) and melting [MIm][Tfo] as the electrolyte at 50–200 °C. The porous structures of PANi and PPy-supported Pt and Ag catalysts resulted in an enlarged surface area and distance for the electro-oxidation of methanol. They provided better electrocatalytic activities in comparison with the bare Pt and Ag electrodes. The current of methanol oxidation started at 0.54 V and attained the maximum current at 0.76 V. The maximum current values were reported to be 0.28 and 0.21 mA cm^{-2} for Pt/PANi and Pt/PPy, respectively. The electrocatalytic behavior of the catalysts at 200 °C was reported to be 3 times that at 50 °C, demonstrating their higher utilization efficiency in high-temperature PEMFCs. According to the results, the best catalyst for use in DMFCs is Pt/PANI due to its oxidation potential at 0.72 V (2 M methanol in 0.25 M H_2SO_4), which is close to the maximum MOR potential at 0.76 V, and its mechanical properties. ESM was also demonstrated as a template to synthesize macroporous Pd and CeO_2-containing Pd network catalysts.[198] The CeO_2-containing Pd network catalyst was synthesized *via* the precipitation method. The CeO_2-containing Pd catalyst possessed a flower-like morphology, which provided a large surface area for electrochemical methanol oxidation. The CV studies were performed in a mixture of methanol (2–50 vol%), 0.25 M H_2SO_4, and 0.3 M [MIm]·H_2SO_4 methanol solution. The results illustrated an increased electrocatalytic performance for methanol oxidation in acidic electrolytes. The unparalleled macroporous network structure of the catalysts resulted in great long-term stability. The Ce–CO bonds were preferentially created over Pd–CO bonds and the incorporation of CeO_2 in the Pd-based catalysts led to an increase in CO tolerance, indicating the excellent potential of this catalyst for methanol oxidation in DMFCs.

SS, another useful bio-waste, was employed for the simple synthesis of Fe- and N-containing porous carbon as a support for Pt NPs *via* the hydrothermal and pyrolysis methods for the MOR.[199] The as-prepared catalyst, denoted as Pt/SC, had a lower electrochemical active surface area than the Pt/C catalyst. However, the MOR mass activity of Pt/SC was reported to be 201 mA mg^{-1} in N_2-saturated 0.5 M H_2SO_4 and 0.5 M CH_3OH solution, which was higher than that of Pt/C (93 mA mg^{-1}). This high activity was attributed to the porous structure of the catalyst and the synergistic effect between carbon and Fe/N on the MOR. Moreover, a facile method was proposed to prepare Pt NPs from bio-waste such as sugarcane bagasse, pineapple peel, and banana peel *via* bio-reduction in a one-pot synthesis.[200] The methanol oxidation of the fabricated Pt NPs was tested by CV analysis in 0.5 M H_2SO_4 mixed with 1 M methanol. The maximum mass activity of 398.20 mA $mg_{Pt}{}^{-1}$ was obtained for Pt NPs–sugarcane, which was 2.52-times higher than that of commercial Pt black. The bio-synthesized Pt NPs from sugarcane bagasse had the highest ECSA (94.58 m^2 g^{-1}). Additionally, a fast MOR was observed for Pt NP–sugarcane due to its high negative onset potential compared with other biogenic Pt NPs

or commercial Pt NPs. In addition, the highest anodic current density of 87.68 mA cm^{-2} was observed for Pt NPs–sugarcane, which was probably due to the higher number of generated electrons. The uniform size and high ECSA of Pt NPs–sugarcane lead to a large number of electrochemically active sites. A bio-synthesis approach for the preparation of Pt NPs was introduced using sugarcane bagasse and Pt ion salt solution.[201] The electrochemical activity of the as-prepared NPs was compared with that of commercial Pt black. The bio-synthesized nano-spheroid Pt NPs displayed a greater ECSA of 94.58 $m^2\ g^{-1}$ and better current density of 400 mA $mg_{catalyst}^{-1}$, which were 3- to 4-times greater than that of commercial Pt. Hence, Pt NPs with outstanding electrochemical features are a good alternative to commercial Pt NPs.

Tables 3 and 4 summarize the works on nature-based composite membranes and nature-based catalysts for DMFC applications, respectively.

3.5 Nature-inspired materials as membranes or catalysts for DEFCs

3.5.1 Membranes. Membranes prepared using PVDF–HFP and MMT were applied in DEFCs.[230] Subsequently, the membranes were functionalized *via* γ-ray irradiation. The porosity of the grafted membranes decreased in the presence of MMT, while the thermal stability of the irradiated membranes (PVDF–MMT–PSSA) increased. The ion exchange capacity values relied on the grafting degree values and mineral particle concentration on the water uptake values. Moreover, the tortuous routes formed by the particles of MMT prevented the permeation of molecules, leading to less fuel cross-over. In the fuel cell test, the highest power densities of 93 and 60 mW cm^{-2} and current densities of 230.3 and 173.3 mA cm^{-2} were achieved for the PVDF–PSSA and PVDF–MMT8–PSSA (8 wt% MMT) membranes at 60 °C using 4 M ethanol, respectively. The composite membranes were synthesized with Nafion® and different types of MMT through the casting process for use in DEFCs.[231] Ca-MMT was used to prepare Mg^{2+}-MMT, K^+-MMT, Na^+-MMT, and H^+-MMT, which were later utilized to synthesize composite membranes denoted as CM-Ca, CM-Mg, CM-K, CM-Na, and CM-H, respectively. The proton conductivity of the composite membranes decreased by about 9% compared to the pure Nafion® membrane due to the blocking of the proton transition channels by MMT. Meanwhile, CM-Na exhibited the highest proton conductivity of 38.5 mS cm^{-1} among the composite membranes at 298 K and 50% RH. The water uptake of the composite membranes had no significant difference, which was approximately 24.30 wt% (~5 wt% more than that of CM). The ethanol permeability of the composite membranes was also reduced by 62–90% *versus* CM because MMT doping blocked the channels for the transport of ethanol. CM-H had the lowest ethanol permeability with a value of 0.69×10^{-6} $cm^2\ s^{-1}$.

3.5.2 Catalysts. An improvement in the catalytic activity of Pd NPs in CO_2 reduction, and also ethanol oxidation was reported.[232] The Pd NPs (5%) were directly incorporated in NiO/C

Table 3 Performance of nature-based composite membranes in the DMFC applications

Membrane	Natural material	Proton conductivity	Water uptake	Methanol permeability	Maximum power density	Temperature	Ref.
Mordenite-PVA	Zeolite	0.01–0.015 S cm^{-1}	—	25 times lower than PVA	—	—	202
PWA doped PVA/Na^+-MMT	Na^+-MMT	Lower 15% in than PVA	Reduced by 32% as PVA	Lower 88% in than PVA	—	RT	203
Nafion/POP/Na^+-MMT	Na^+-MMT	92 mS cm^{-1}	32.9 wt%	Lower 40% in than Nafion	13.3 mW cm^{-2}	313 K	204
Nafion/Na^+-MMT-POPD400-PS	Na^+-MMT	Higher than Nafion	—	1.2×10^6 $cm^2\ s^{-1}$	—	40 °C	205
Krytox-Na^+-MMT-Nafion	Na^+-MMT	48 mS cm^{-1}	31.6 wt%	1.2×10^{-6} $cm^2\ s^{-1}$	—	40–100 °C	206
Sulfonated MMT/SPEEK	Na^+-MMT	105 mS cm^{-1}	15 wt%	2.1×10^{-8} $cm^2\ s^{-1}$	21 mW cm^{-2}	60 °C	207
PVA/Na^+-MMT	Na^+-MMT	0.0368 S cm^{-1}	—	3.67×10^{-6} $cm^2\ s^{-1}$	6.77 mW cm^{-2}	RT	208
Nafion/AMPS-Na^+-MMT	Na^+-MMT	0.0817 S cm^{-1}	—	0.091×10^6 $cm^2\ s^{-1}$	87.96 mW cm^{-2}	70 °C	209
SPEEK/Ferrierite	Ferrierite zeolite	$8.224 \times 10^{-2} \pm 2.298 \times 10^{-4}$ S cm^{-1}	10%	3.51555×10^{-6} $cm^2\ s^{-1}$	—	30–70 °C	210
Nafion/Na^+-SWy-2	Na^+-SWy-2	Higher than Nafion	45 wt%	—	Higher than Nafion	90–110 °C	211
SPEEK/AMPS-Na^+-MMT	Na^+-MMT	Higher than SPEEK	Lower than SPEEK	Lower than SPEEK	188 mW cm^{-2}	70 °C	212
CS/GPTMS-MMT	MMT	4.66 mS cm^{-1}	Lower than CS	3.03×10^{-7} $cm^2\ s^{-1}$	—	30–730 °C	213
SEP-PPMS	SEP	0.144 S cm^{-1}	64%	2.69×10^{-8} $cm^2\ s^{-1}$	210 mW cm^{-2}	110 °C	92
CS/PNZ/rGO	Zeolite	6.777×10^{-6} S cm^{-1}	294.5%	31.5×10^{-5} $cm^2\ s^{-1}$	—	—	214

Table 4 Performance of nature-based catalysts for DMFC applications

Composite	Natural material	Maximum power density/ current density of fuel cell	Performance	Ref.
Pt/N-doped carbon-MMT (Pt/CN_x-MMT)	MMT	—	Onset potential of 0.13 V Oxidation of the current density of the catalyst was 2.3 times higher than Pt/C Higher specific methanol oxidation compared with Pt/C ECSA of 36.6 $m^2\ g_{Pt}^{-1}$	215
Pt/nitrogen-containing carbon	Soybeans	—	Lower onset potential (0.25 V) compared with Pt/Vulcan carbon XC-7 (0.35 V) Current density of Pt/CS was 1.5 times higher than Pt/Vulcan carbon XC-72 Better durability than Pt/Vulcan carbon XC-7 Lower Tafel slope (96.5 mV dec^{-1}) than Pt/Vulcan carbon XC-7 (103.3 mV dec^{-1})	216
Pt–SiC/GCN	Coconut shell	1585.3 A g^{-1} Pt	ECSAs of 147.1 $m^2\ g^{-1}$ Pt Higher methanol oxidation current density compared with Pt/C (257.4 A g^{-1} Pt) Higher stability than Pt/C	217
Pt–Ru/AC	Rice husks	9.1 mA cm^{-2}	Better methanol oxidation compared with Pt–Ru/CB	218
Pt/HGCN	Human hair	140.0 mA $cm^2\ mg_{Pt}^{-1}$	ECSA of 92.31 $m^2\ g^{-1}$ The current density of Pt/HGCN was 1.63 times higher than Pt/Vulcan carbon XC-72 Higher stability compared with Pt/Vulcan carbon XC-72	219
Fe-inserted pig bones derived N-doped carbon	Pig bone	—	High specific surface area of 562.6 $m^2\ g^{-1}$ Higher ORR activity than 10% Pt/C ORR onset potential of 0 V Better methanol tolerance than Pt/C High stability comparable to commercial Pt/C	220
Carbon–boron core–shell ($B_{0.5}$CNMs@$C_{1.0}$)	Red onion skins	—	ORR onset potential of 0.87 V ORR current density of 1.2 mA cm^{-2} Good CO poisoning compared with Pt/C High durability compared with Pt/C	221
Silicon nanosheets-GQDs	Fenugreek seed and rice husks	—	ORR onset potential of −0.33 V ORR current density of 2.61 ± 0.27 mA cm^{-2} Excellent tolerance to methanol and CO poisoning Tafel slope of 96 ± 2.2 mV dec^{-1} Higher stability compared with commercial Pt/C	222

Table 4 (*Contd.*)

Composite	Natural material	Maximum power density/ current density of fuel cell	Performance	Ref.
NC NPs	Spiral seaweeds	—	Onset potential of 0.01 V ORR current density less than Pt/C (only 0.20 mA cm^{-1}) High methanol tolerance for ORR compared with Pt/C Having more durability toward ORR compared with Pt/C	223
N, P, and Fe-doped hierarchically porous carbons	Tea-leaf	—	Higher ORR current density of 1.25 mA cm^{-2} compared with Pt/C (0.75 mA cm^{-2}) High catalytic stability than that of Pt/C Good tolerance against the methanol crossover Good tolerance to CO poisoning	224
AC	Waste-tea	72 ± 3 mW cm^{-2}/200 mA cm^{-2}	Temperature of 30–70 °C Good long-term stability	225
ZIF-67@N-doped carbon	Pomelo peels	—	Better ORR activity compared with carbon without N Higher kinetic current density of −4.97 mA cm^{-2} compared with Pt/C, ZIF-67, and N-doped carbon Lower Tafel slope of 40 mV dec^{-1} than that of N-doped carbon Great electron transfers toward ORR Excellent stability High tolerance to methanol crossover	226
N-doped HPC/rGO	Pomelo peel coupled with GO	—	Higher ORR current density of 5.413 mA cm^{-2} compared with N-RGO (3.71 mA cm^{-2}) and N-HPC (4.574 mA cm^{-2}) Better long-term stability compared with Pt/C Excellent methanol tolerance than that of Pt/C	227
Ni deposited on mixed ZnO/ CuO immobilized on amine-functionalized FA-coated conductive poly(Py-*co*-O-Anis) co-polymer composite	FA	103.24 mW m^{-2}	Excellent catalytic activity High surface area of 98.6 m^2 g^{-1} Superior long-term stability for methanol oxidation Temperature of 70 °C	228
Pt/zeolite Faujasite-C	FA	—	Lower surface area (102.60 m^2 g^{-1}) and ECSA (4.03 cm_{Pt}^2) for Faujastic-C compared to carbon Vulcan The peak potential of 49 mV, more desired than Pt/C in the methanol oxidation MOR current density of 11 mA cm^{-2}	229

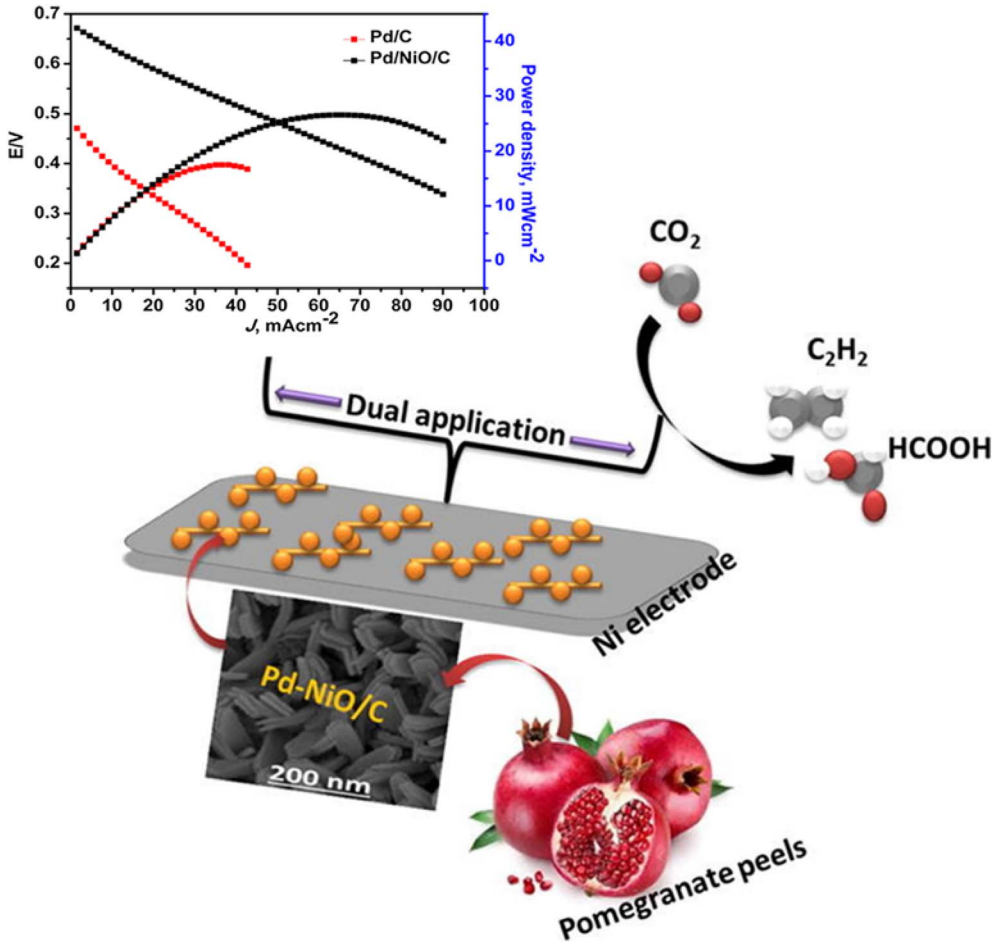

Fig. 18 Schematic representation of nanocomposite synthesis and its applications. Reprinted with permission from ref. 232. Copyright (2019), Elsevier.

via a green, straightforward, one-step method utilizing extracts of pomegranate peel as the reducing agent (Fig. 18). The Pd–NiO/C catalyst displayed higher catalytic activity in ethanol oxidation and higher tolerance to balance by intermediate oxidation species. The catalyst as an anode in a DEFC improved the cell performance and delivered a maximum power density as high as 26 mW cm^{-2} with a current density of 66 mA cm^{-2} at 25 °C using 1 M KOH + 1 M ethanol solution. Moreover, it showed an increase of 45% efficiency in HCOOH selectivity.

3.6 Nature-inspired materials as membrane or catalysts for MFCs

3.6.1 Biomass-based (nano)materials

3.6.1.1 Membranes. ESM with ion transportation ability is a natural hydrophilic and low-cost membrane, which can be employed as an organic separator in air-cathode MFCs.[233] The finite oxygen permeability and great mass transfer of ESM result in an increase in power generation. A single-chamber GU-fed (1 g L^{-1}) MFC including an ESM separator generated a maximum power density of 1441 ± 15 mW m^{-2} (at 3.47 ± 0.05 A m^{-2}), while 1415 ± 10 mW m^{-2} (at 3.46 ± 0.08 A m^{-2}) was reported for the MFC without ESM. The use of ESM in the MFC resulted in a decrease in the anode potential (13.62%), without influencing the cathode potential. Meanwhile, the CE values were reported to be 67.14–95.03% with ESM and 22.11–38.21% without it. The results of LSV tests illustrated that the current density for the ESM-cathode and bare cathode were 34.91 ± 0.25 A m^{-2} and 38.14 ± 0.32 A m^{-2}, respectively. The ESM-cathode had good output voltage stability with an insignificant decline after 800 h (6 cycles, 28 mL reactor). The slight decline in the current density of the ESM-cathode is due to the transfer resistance. In addition, the comparison of the MFCs based on an ESM (MFC_E) and 3 other types of MFCs with Nafion® membrane (MFC_N), polydimethylsiloxane membrane (MFC_P), and membrane-less device (MFC_M) showed that the former gave a better fuel cell output.[234] After one week of feeding, the polarization experiment indicated that the maximum internal resistances were exhibited by MFC_N and MFC_P, which were about 8.5-times that of MFC_E and MFC_M. Hence, the power densities of MFC_N and MFC_P were twice that of MFC_E and MFC_M, which was due to the diffusion of oxygen gas into the anode chamber of the MFC_E and MFC_M devices. However, increasing the electrode spacing from 4 to 8 mm in the cell containing MFC_E and MFC_M led to an enhancement in the output power, which was owing to the

reduction in oxygen cross-diffusion. The utilization of the ESM led to a reduction in the internal resistance and provided high sensitivity to the unstable organic carbon content in AW.

3.6.1.2 Catalysts. Porous carbon-based materials have been widely employed as an anode in MFCs. Direct carbonization of natural plants is an affordable and effective approach for the synthesis of carbon-based materials. The kenaf stem can be employed as a natural raw material to prepare 3D macroporous carbon (3D-KSC) *via* a facile carbonization method as the anode in MFCs.[235] A 3D structure can enhance the surface area of the macroporous electrode structure, improving substrate transfer and biofilm propagation. The carbonized kenaf stem possessed a cylindrical shape, retaining its macroporous structure well. The carbonized 3D-KSC at 1000 °C exhibited acceptable electrical conductivity with a resistance of 10 Ω and showed the highest electrocatalytic current density of 32.5 A m^{-2} with a length of 0.23 cm, which was thrice that of a graphite rod (11.2 A m^{-2}). The superior performance of 3D-KSC was due to its

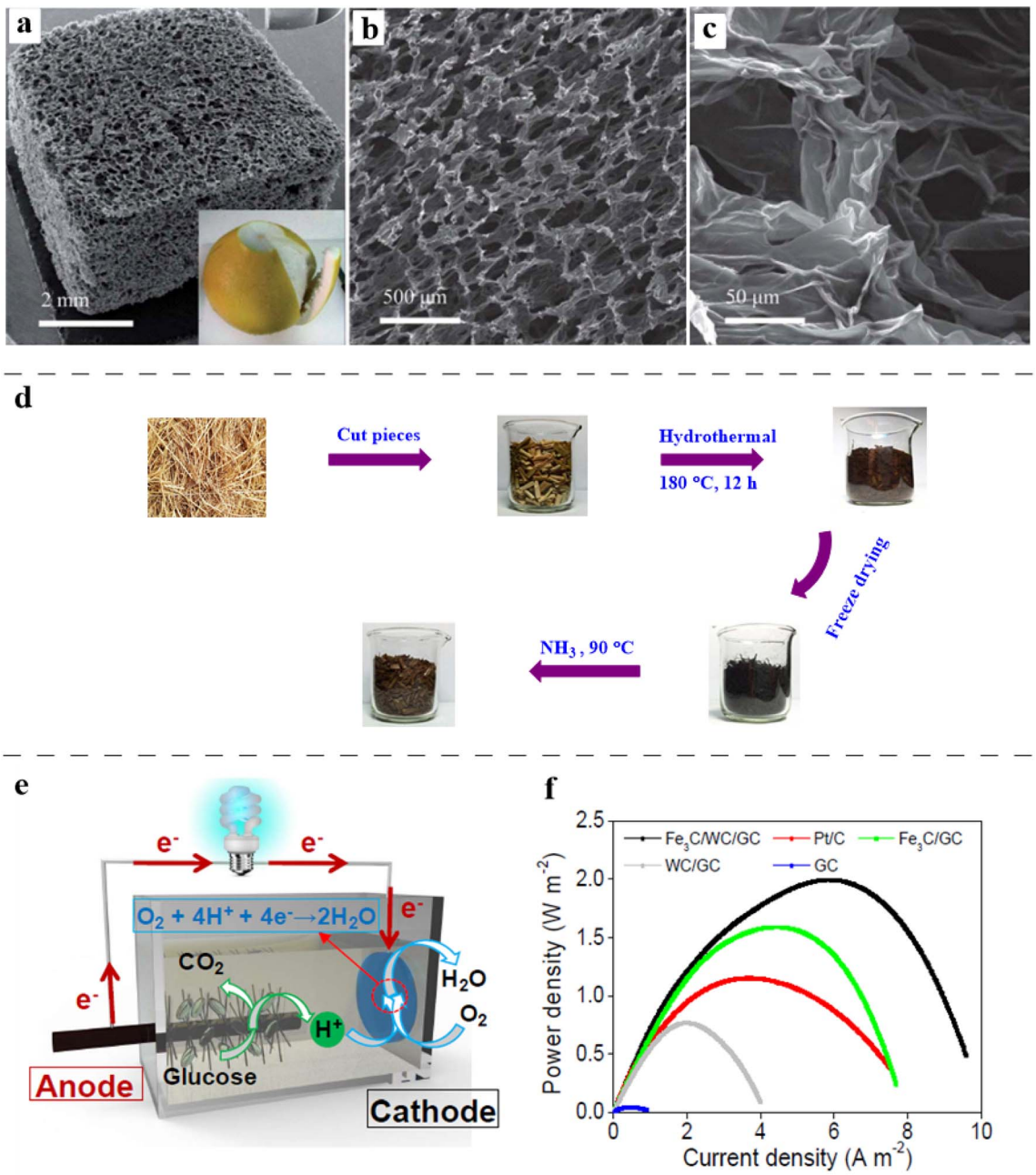

Fig. 19 (a–c) SEM images of RCF-PP at different magnifications, where the inset of A is a digital image of a peeled pomelo. Reprinted with permission from ref. 236. Copyright (2012), The Royal Society of Chemistry. (d) Production of NCs from rice straw. Reprinted with permission from ref. 238. Copyright (2015), The Royal Society of Chemistry. (e) Schematic single-chamber MFC reactor for testing the performances of electrocatalysts and (f) power density as a function of current density. Reprinted with permission from ref. 240. Copyright (2016), the American Chemical Society.

microchannel structure, which helped in the high growth of electroactive bacteria. The direct carbonization of the sponge-like pomelo peel (RCF-PP) is another way to fabricate reticulated carbon foam, which can be applied as an anode in MFCs.[236] The SEM images in Fig. 19a–c present the net-like macroporous structure of RCF-PP with micro-sized pores and wrinkled surface, which resulted in great wetting properties, bacterial compatibility, and a higher current density, 5-times that of commercial RVC foam and 2.5-times that of graphite felts with the same electrode size. The projected current density of over 4 mA cm^{-2} and volumetric current density of 18.7 mA cm^{-3} were reported for the RCF-PP electrode.

Biochar with high porosity and conductivity is a type of carbon-rich byproduct, which is a significant electrode material for MFCs. SS can be converted to carbon monoliths (SMs) using different amounts of coconut shell and a heat treatment process.[237] Among the anodes, SMs with 10 wt% coconut shell (SM-10) exhibited the highest power density of 1069 ± 15 mW m^{-2}, which was 2.2-times that of the SM anode without coconut shell. Additionally, the maximum power density of SM-10 was 2.6- and 1.4-times higher than the graphite plate and coconut shell-derived carbon plate anodes, respectively. The catalytic activity of the sample toward the ORR showed that the onset potential of the powdered SMs is −0.19 V *vs.* SCE, which was more negative than that of Pt/C (−0.09 V *vs.* SCE). The limiting current densities of the catalysts were enhanced by increasing the coconut shell content and the maximum value was achieved for PSM-10. The durability test at −0.35 V in 0.1 M KOH solution for 10 000 s showed that PSM-10 with slow attenuation and high current retention has better stability than Pt/C. In air-cathode single-chamber MFCs, the highest power density (969 ± 28 mW m^{-2}) was obtained for the MFC with the SM-10 anode and PSM-10 cathode, which was 2.4-times that of the MFC containing graphite and Pt (as anode and cathode, respectively). In addition, the output voltage of the aforementioned PSM cathode was greater than that of the Pt/C cathode after 35 days, indicating its excellent stability. For the synthesis of a cost-efficient ORR catalyst for MFCs, converting rice straw to NC *via* a simple three-step process (Fig. 19d) was reported to be beneficial.[238] The catalytic activity of the NC (H-NC) heated at 800, 900, and 1000 °C was compared. The onset potential of H-NC-900 was 0.22 V, which was lower than that of H-NC-800 and H-NC-1000. Besides, the balance of the nitrogen value, GC structure, and good specific surface area features of H-NC-900 provided catalytically active sites. A single-chamber MFC was utilized to study the ORR activity of the metal-free catalysts. Among them, the H-NC-900 air-cathode with a power density of 2300 mW m^{-2} exhibited the best MFC performance (operated at 35 °C). Meanwhile, the most stable voltage of 0.653 V was obtained for the H-NC-900 catalyst due to its fine N-doping and large surface area.

The carbonization procedures of three natural materials of king mushroom (CEKM), wild mushroom (CEWM), and corn stem (CECS) led to the fabrication of low-cost and novel carbon anodes for MFCs.[239] The highly porous 3D structure of the carbon electrodes with exceptional electron transfer rate made them suitable as the anode of MFCs and the formation of electrochemically active biofilms. Among the prepared electrodes, CECS represented the best functionality with an optimum electrocatalytic current density of 3.12 mA cm^{-2}, which was 8-times that of GE.

Carbon-derived biomass obtained *via* thermal pyrolysis can take part in the ORR *via* a two-electron path to form peroxide species and metallic catalysts can improve the ORR catalytic activity of these carbon materials (*i.e.*, four-electron). Hence, a porous Fe_3C/WC/GC nanocomposite was prepared *via* a one-step carbon-thermal reduction method using pomelo peel as the carbon source and was tested towards the ORR.[240] The catalyst was applied as an air-cathode in a single-chamber MFC, as shown in Fig. 19e. The Fe_3C/WC/GC nanocomposite was highly active, selective, and stable towards the four-electron ORR in a pH-neutral electrolyte, resulting in a high power density, which was 67.82% greater than that of the commercial Pt/C (Fig. 19f). Furthermore, the decline in its voltage was negligible during a long-term period of 2200 h MFC operation.

Chestnut shell, a fruit with large plantation areas globally, was carbonized into a carbon ball and employed as an anode in MFCs.[241] The carbon ball showed a hierarchically urchin-like structure at both the macroscopic and microscopic levels. The carbon ball connected to titanium wire was employed as an anode for MFCs (Fig. 20a–c) and exhibited power densities of 759 ± 38 mW m^{-2} and CE of 75% ± 12%. This considerable efficiency was attributed to the high surface area of CSE resulting from the thorns on its surface, which were comprised of dense cylindrical fibers with a wrinkled structure (Fig. 20d–f), increasing the adsorption of fine spherical particles and microorganisms.

FeO NPs have outstanding features such as super-paramagnetic behavior and biocompatibility; however, their chemical synthesis is toxic and expensive. Therefore, developing simple, low-cost, and eco-friendly approaches for the synthesis of iron oxide is attractive. The FeO NPs synthesized using the hydroalcoholic *Amaranthus dubius* leaf were used to coat the carbon anode in a two-chamber MFC.[242] According to the power density curves, the FeO-coated electrodes enhanced the fuel cell performance by 31%. The power density and current density of the cells with the coated electrodes were 140.5 mW m^{-2} and 265 mA m^{-2}, which were higher than that of the unmodified electrode (110.5 mW m^{-2} at 235 mA m^{-2}), respectively. The COD removal efficiency for the modified and unmodified electrodes was 68.5 and 63.1%, respectively. The waste treatment ability of the coated electrode was examined by CV analysis, indicating that the current density of the FeO electrode was higher than the bare electrode. This higher current density indicates that more redox mediators are involved in the electron transfer, which improves the MFC performance. Corncob is a widely available natural material, containing carbon, nitrogen, and oxygen elements. The high temperature (250 °C to 750 °C) pyrolysis of corncob can produce biochar with high conductivity and superior ORR catalytic performances in single-chamber air-cathode MFCs.[243] The ECSA of the biochar obtained at 650 °C (CC-650) was 655.89 m^2 g^{-1}, which was higher than that of the other catalysts. Hence, CC-650 had more active sites for the ORR. The CC-650 cathode

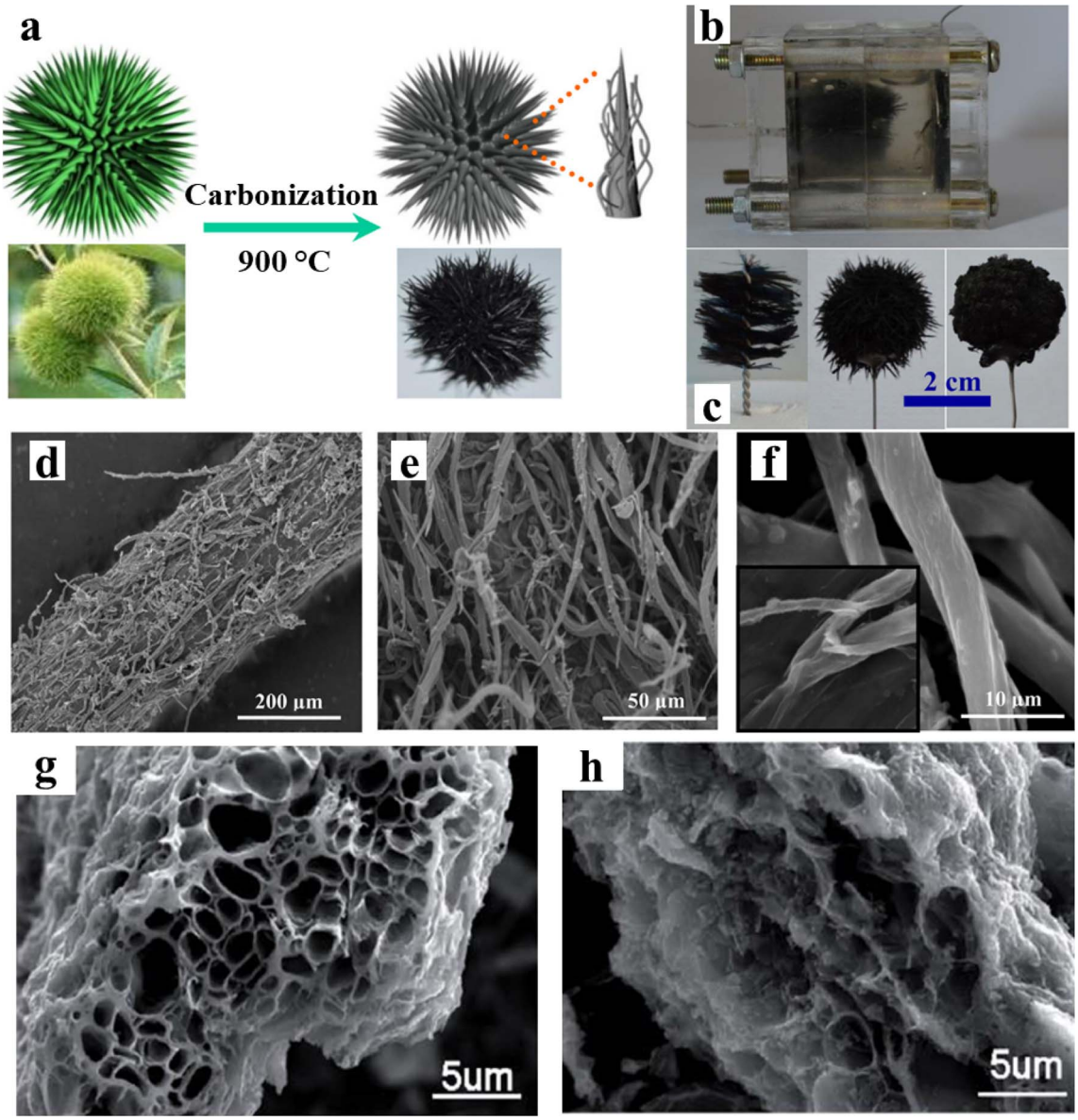

Fig. 20 Morphology characteristics of CSE. (a) Schematic illustration of the preparation of CSE, (b) photograph of the MFC equipped with CSE, (c) photographs of the brush, CSE, and thornless CSE, (d) SEM image of the thorns on CSE, (e) high-resolution SEM image of the thorns on CSE and (f) SEM image of the fibers grown on the surface of the thorns on CSE. Reprinted with permission from ref. 241. Copyright (2016), Elsevier. SEM images of (g) EPGC-800-2 and (h) EPGC-900-2. Reprinted with permission from ref. 245. Copyright (2021), The Royal Society of Chemistry.

possessed the highest diffusion coefficient, leading to high conductivity and abundant electron acceptors. The MFC tests revealed that the cell equipped with CC-650 exhibited the best performance with a power density of 458.85 mW m^{-3} compared to the other biochar electrodes. In addition, the aforementioned biochar showed the highest current density with an onset potential of −0.13 V. This relatively high electrochemical activity was attributed to its highest surface area and high content of graphitic and pyridinic nitrogen. Graphitic and pyridinic nitrogen accelerated the electron transfer *via* the four-electron route and increased the reaction rate of the ORR. SHS, as carbon and nitrogen sources, can also be utilized for the formation of mesopores N and P-co-doped carbon catalysts *via* straightforward PA pretreatment and carbonization.[244] The resultant catalyst, carbonized at 900 °C (PA-SHS 900) exhibited high ORR activity with a current density of 4.47 mA cm^{-2}, which was close to the current density of commercial 20% Pt/C (5.01 mA cm^{-2}). Besides, in a single-chamber MFC, PA-SHS 900 as the cathode showed the highest power density of 802 mW m^{-2}, approaching that of 20% Pt/C (892 mW m^{-2}) with better stability. HPC is an attractive modern carbon material for the ORR due to its high surface area and porosity. Potassium trioxalatoferrate(III) trihydrate ($K_3[Fe(C_2O_4)_3]\cdot 3H_2O$) was employed to obtain a eggplant-derived porous graphitic material with a high carbonization and graphitization degree.[245] As depicted in Fig. 20g and h, the activation process at a temperature of

800 °C provided greater porosity. The maximum current density for the ORR using EPGC-800-2 (activated at 800 °C with 2 wt% of $K_3[Fe(C_2O_4)_3]$/eggplant) was 0.25 mA cm^{-2}, which was close to that of Pt/C (0.27 mA cm^{-2}). Besides, the onset potential of EPGC-800-2 (0.766 V) was close to that of Pt/C (0.740 V), which was also more positive than that of the other samples. In fact, the large surface area, porous structure, high conductivity, and high graphitization degree of EPGC-800-2 resulted in its excellent ORR activity. The MFC performance tests of the cathode catalysts exhibited that the maximum power density of EPGC-800-2 (667 mW m^{-2}) was higher than that of Pt/C (621 mW m^{-2}). Meanwhile, the output voltage of the MFC with the EPGC-800-2 cathode was stable at approximately 380 mV during 240 h of operation, showing good stability.

Yaqoob *et al.* prepared an anode by utilizing lignin-based GO (L-GO) derived from oil palm biowaste through the soda pulping process for a double-chamber MFC. To enhance the electron transportation rate, L-GO was combined with ZnO.[246] The L-GO/ZnO anode achieved a power density as high as 1350 × 10^{-3} mW m^{-2} at 142.98 mA m^{-2}, while the L-GO anode had a power density of 20 × 10^{-3} mW m^{-2} at 17.54 mA m^{-2}. The Pd^{2+} removal efficiency of L-GO/ZnO from wastewater was higher than that of the L-GO anode. It was reported that the exoelectrogen bacteria formed filamentous structures, which led to the transfer of electrons. Another mechanism reported the transfer of electrons from the bacteria to the anode, as schematically shown in Fig. 21.

Zha *et al.* utilized mangosteen peel as a natural carbon and nitrogen source to prepare porous N-doped GC, which was activated using KOH and graphitized using Co^{2+}.[247] The MPC catalyst activated at 800 °C (MPC-800) had an adequate porous architecture with a high specific surface area of 1168 m^2 g^{-1} and a high degree of graphitization with high graphitic nitrogen content. The highest output power of the MFC with MPC-800 was 240 mW m^{-2} at 1 A m^{-2}, which was higher than that of Pt/C (220 mW m^{-2} at 0.90 A m^{-2}). Furthermore, MPC-800 presented the maximum CE of 7.37% ± 0.25%, which was higher than that of Pt/C (7.08% ± 0.20%). Embedding magnesium cobaltite ($MgCo_2O_4$) in N-doped carbon ($MgCo_2O_4$/NC-700) resulted in a superior electrochemical performance in MFC compared with Pt/C.[248] To synthesize this practical electrocatalyst, hydrothermal and pyrolysis methods were employed, in which corncob and urea were used as affordable carbon and nitrogen precursors, respectively. $MgCo_2O_4$/NC-700 had higher catalytic activity toward the ORR with a more positive onset potential of 0.478 V compared with that of Co/NC-700 and Mg/NC-700. The presence of Mg increased the number of active sites by reducing the crystallite size, thus improving the ECSA of the composite. Besides, the composition of Co ions with N-doped carbon matrix improved the surface features, catalytic surface area, and electrical conductivity. Therefore, the synergistic effect of Mg and Co ions compared to the monometallic oxide carbon catalysts led to the excellent electrochemical activity of $MgCo_2O_4$. This catalyst gave the maximum power density of 873.81 ± 37.15 mW m^{-2}, which was 1.59-times better than that of Pt/C. In addition, the acquired COD removal efficiency was 82.92% for the $MgCo_2O_4$/NC-700-modified MFC. Employing rice husk-derived silicon NPs (RH-Si) to modify the anode led to a remarkable output power in a two-chamber MFC.[249] The spherical-shaped silicon NPs were synthesized through the pyrolysis of rice husk, followed by a magnesiothermic reduction process, and then coated on carbon cloth by spray pyrolysis. The modified anode demonstrated a high surface area (18.37 m^2 g^{-1}), increasing the chemical reaction rate due to the increase in the number of active sites. These sites not only act as reaction sites but also provide sites for increased bacterial attachment and electron transport. The comparison of two H-shaped MFCs, including an RH-Si anode and bare carbon cloth anode, showed that the modified anode led to a power density of 190.5 ± 3 mW m^{-2}, which was 7.6-times that of the MFC with the unmodified anode. The good electron transfer between the bacteria and anode and increased number of active

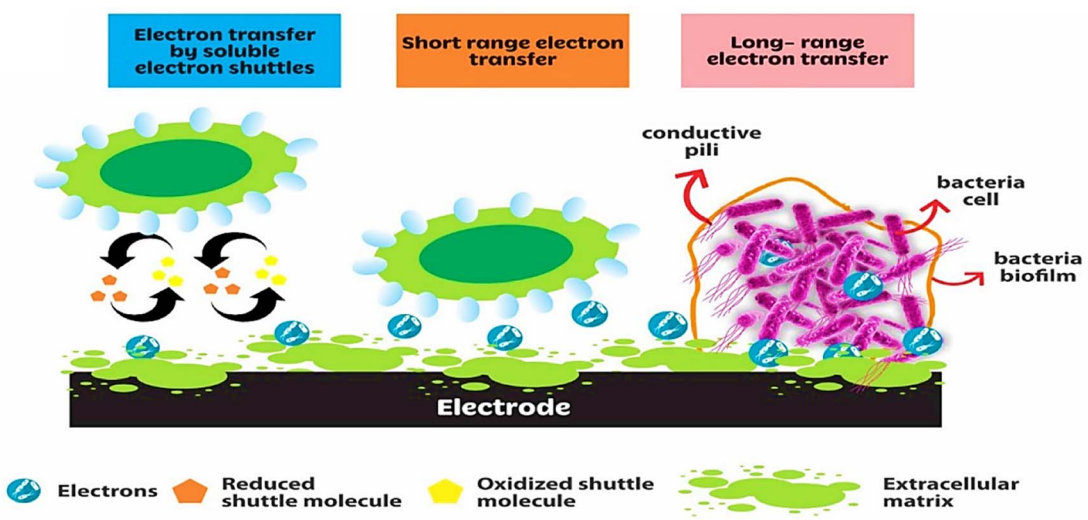

Fig. 21 Different mechanisms of electron transfer from bacteria cell to the electrode. Reprinted with permission from ref. 246. Copyright (2021), Elsevier.

sites for bacterial growth enhanced the power density of the MFC with the modified anode.

3.6.2 BOT-based (nano)materials

3.6.2.1 Catalysts. SMFCs have attracted increasing attention for organic-contaminated soil remediation and energy conversion; however, they have a limited output. In this case, the use of suitable electrode materials can improve the performance of SMFCs. A modified graphitic felt anode with BOT-Fe (GFB) and Fe_3O_4 NPs (GFF) enhanced the electrical features of an air-cathode SMFC operated in a water bath at a temperature

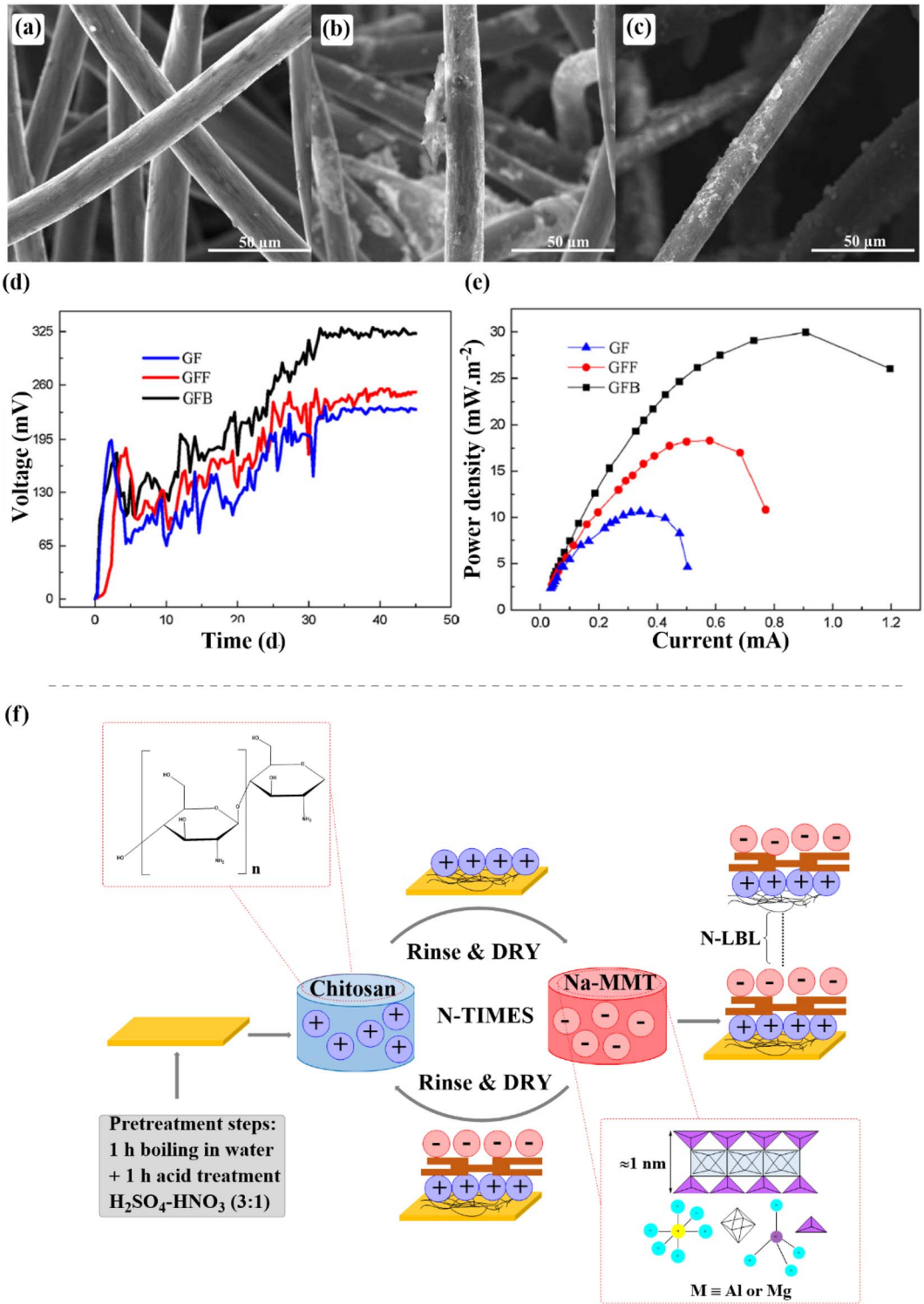

Fig. 22 SEM images of three anode materials (a) GF, (b) GFF, and (c) GFB. Electric performances of soil MFCs with different anode materials (d) voltage outputs and (e) power density curves. Reprinted with permission from ref. 250. Copyright (2019), Elsevier. (f) Layer-by-layer (LBL) assembly steps. Reprinted with permission from ref. 251. Copyright (2018), Elsevier.

of 30 °C.[250] According to the SEM images in Fig. 22a–c, GF has a 3D macroporous structure with a large specific surface area and graphite fibers (20 μm diameter), while the modified GF possesses a rougher surface. As shown in Fig. 22d, the stabilized voltage of GFF and GFB was enhanced by 8.26 and 40.87%, respectively, suggesting the better electrical features of the SMFCs. The maximum power density of 29.98, 18.28, and 10.60 mW m^{-2} was achieved for the GFB, GFF, and GF anodes, respectively (Fig. 22e).

3.6.3 MMT-based (nano)materials

3.6.3.1 Membranes. The composition of layered silicate minerals with polymers provides a "brick-and-mortar'' structure with excellent thermal, mechanical and barrier properties. A layer-by-layer assembled CS/MMT composite film on an unglazed wall ceramic was employed as a separator in a two-chamber MFC by Yousefi *et al.* (Fig. 22f).[251] The temperature of the MFC was controlled using a temperature control box (35 ± 5 °C). The wastewater treatment performance of MFCs with separators including different amounts of composite was determined based on COD and BOD removal. The removals efficiencies of COD and BOD were up to 80% for MFCs. The best MFC performance was observed for the MFC containing seven bi-layers of nanocomposite, where the highest power density (119.58 ± 19.16 mW m^{-2}) and current density (869.44 ± 27.49 mA m^{-2}) were observed, which were twice that of the blank-ceramic. The CE of the blank-ceramic was 27.58% ± 4.19%, which was enhanced to 43.64% ± 0.44% with the addition of seven bi-layers of composite. In addition, the proton conductivity of the separator with seven bi-layers of the composite increased by 125% compared to the blank-ceramic. In another report, CS/MMT nanocomposites were loaded on the ceramic surface through the self-assembly route.[252] The ceramic membranes were employed as separators for the anode and cathode chambers in the MFC. The produced current of the MFC with the self-assembled CS/MMT (MFC-CMMT) separator increased by 95.8%. The highest CE of 86.97% ± 13.2% was observed for MFC-CMMT with 1 wt% CS and 2 wt% MMT (MFC-CMMT-1/2). The polarization tests indicated that the maximum power density of 229.12 ± 18.5 mW m^{-2} and current density of 1422.22 ± 41.2 mA m^{-2} were obtained for MFC-CMMT-1/2, which were higher than that of the MFC with the blank-ceramic (447.11 ± 21.37 mA m^{-2} and 63.82 ± 10.42 mW m^{-2}), respectively. The proton conductivity of MFC-CMMT-1/2 was 222.73 ± 22.7 μS cm^{-1}, which was that maximum among the separators.

3.6.4 Aluminosilicate-based (nano)materials

3.6.4.1 Membranes. A PEM prepared by blending natural clay with coconut shell-derived AC (ACCS) can replace the costly Nafion® 117 membrane in MFCs.[253] Natural clay with hygroscopic oxides improved the hydration property of the membrane, while the high surface area of ACCS helped to retain bound water and proton hopping. Alternatively, the presence of natural clay led to great mechanical stability in the PEM. The proton diffusion coefficient of the ACCS/clay membrane was reported to be 36×10^{-6} cm^2 s^{-1}, which was higher than that of the Nafion® 117 membrane (4.64×10^{-6} cm^2 s^{-1}). The maximum power density of 3.7 W m^{-3} was reported for MFC-ACCS/clay with 779 mA m^{-2} at an external load of 170 Ω, which was twice that of the Nafion® 117 membrane as a separator in an MFC under ambient temperature of 26 °C ± 2 °C (1.9 W m^{-3} at 556 mA m^{-2}) and a similar external load resistance. The average COD removal efficiency of MFC-ACCS/clay was 81.05% ± 0.08% while that of MFC-Nafion® was 72.14% ± 0.15%.

3.6.4.2 Catalysts. The application of a modified carbon cloth anode with MnO_2 and HNTs in an air-cathode single-chamber MFC resulted in a significant performance.[89] The electrochemical behavior of MFC was tested in the presence of different anodes, *i.e.*, unmodified anode, HNT, MnO_2, 25 wt% MnO_2/HNT, 50 wt% MnO_2/HNT and 75 wt% MnO_2/HNT. In batch-fed mode (at 33 °C), the best performance was observed for the MFC with 75 wt% MnO_2/HNT anode and the highest values of maximum voltage and power density observed were 663 mV and 767.3 mW cm^{-2}, respectively. Given that chemical energy is released by the biodegradation of organic materials in MFCs, the performance of the anode for the biodegradation of organic compounds was determined. The highest CE of 7.65% and COD removal of 93.1% were obtained for 75 wt% MnO_2/HNT. According to the above-mentioned results, the 75 wt% MnO_2/HNT anode displayed excellent catalytic activity, which was ascribed to the good dispersion of MnO_2 on the HNT surface, leading to a high surface area and facile electron transfer. Besides, the hydrophilic surface of 75 wt% MnO_2/HNT caused facile bacterial loading, improving the power and output voltage. Table 5 reveals a summary of the works on nature-based materials in the MFCs applications.

3.7 Nature-inspired materials as membrane or catalysts for AFCs

3.7.1 Membranes. A quaternized ostrich ESM (q-OESM) was prepared by adding methyl iodide, and subsequently sulfonated using sodium allyl sulfate, followed by (s-OESM) *in situ* polymerization.[276] Modification of OESM was done for both the proton and anion exchange membranes in an AFC. The tensile stress of q-OESM, s-OESM, and OESM was 1.4, 2.08, and 2.4 MPa, respectively. The better mechanical properties of OESM compared with q-OESM were due to the presence of sulfonate groups. The modified OESM membrane demonstrated higher proton conductivity than OESM. q-OESM revealed appropriate anion conductivity of 40 mS cm^{-1}, and s-OESM showed suitable proton conductivity of 47.9 mS cm^{-1}. The water uptake of the membranes was reported to be 274% and 286% at 25 °C and 80 °C, respectively. The methanol crossover was evaluated using the voltammetric technique. Low methanol oxidation and current density (0.18 mA cm^{-2}) were obtained for q-OESM at 25 °C, resulting in less methanol crossover than s-OESM.

3.7.2 Catalysts. A green and simple method was utilized to prepare beneficial ORR catalysts by *in situ* anchoring Fe_2N NPs on N-doped carbon derived from pomelo peel.[277] The as-prepared catalyst (Fe–N-PPC), comprised of Fe-based NPs loaded on N-doped pomelo peel-derived carbon, demonstrated more positive onset and half-wave potentials (14 and 26 mV,

Table 5 Performance of nature-based materials in MFCs

Composite	Natural material	Component of MFC	Type of MFC	CE (%)	Maximum power (density) output	Ref.
Modified zeolite with bacterium consortium	Zeolite	Anode	Two-chamber	—	0.68 W m^{-2}	254
Ceramic	MMT and kaolinite	Separator	Two-chamber	—	7.5 W m^{-3}	255
Loofah sponge carbon–carbon coated TiO_2 (LSC-TiO_2@C)	Egg white	Anode	Single-chamber	46	2.59 ± 0.12 W m^{-2}	256
Activated livestock SS carbon (LSC-A)	SS	Cathode	Single-chamber	—	1273 ± 3 mW m^{-2}	257
Coconut shell biochar	Coconut shell	Anode and cathode	Two-chamber	0.1	61.469 mW m^{-2}	258
Rice husk charcoal	Rice husk	Anode and cathode	Two-chamber	—	6.9 ± 3.1 W m^{-3}	259
Coconut shell	Coconut shell	Membrane	Two-chamber	16.53	3.2 W m^{-3}	260
SS mixed with FA (SSFA)	SS and FA	Anode	Two-chamber	—	3.2 W m^{-2}	261
Activated microporous–mesoporous carbon	Chestnut shell	Anode	Single-chamber	—	850 mW m^{-2}	262
SS-derived carbon (SSC)	SS	Anode	Two-chamber	—	2228 mW m^{-2}	263
Sulfur/nitrogen-doped partially graphitized carbon–Si	Pomelo peels	Cathode	Single-chamber	21.59	1161.34 mW m^{-2}	264
Pyrolysed almond shells	Almond shells	Anode	Two-chamber	85	—	265
Biochar	Olive mill waste	Cathode	Single-chamber	9.9 ± 1.5	271 ± 34 mW m^{-2}	266
Ceramic membrane including soil/RHA	RHA	Membrane	Two-chamber	2.04 ± 0.025	80.15 mW m^{-2}	267
MgO-modified biochar	Maize straw	Anode	Single-chamber	6.01 ± 0.25	4.45 ± 0.21 W m^{-3}	268
3D N-doped carbon foam	Corncob	Anode	Two-chamber	—	4990 mW m^{-2}	269
Clayware	MMT	Membrane	Two-chamber	10.2	83.5 mW m^{-2}	84
SC	Municipal sludge	Anode	Single-chamber	—	615.2 mW m^{-2}	270
Biochar-copper (CS–$Cu_{0.4}$)	Coconut shell	Anode	Two-chamber	13.5	47.04 ± 0.5 mW m^{-2}	271
PPY/SSC	SS	Cathode	Two-chamber	—	760.7 mW m^{-2}	272
Lignin-based-GO-ZnO (L-GO-ZnO)	Oil palm	Anode	Two-chamber	—	2.55 mW m^{-2}	273
Ceramic membrane	Clay, BOT, FA	Membrane	Three-chamber	—	24.56 mW m^{-2}	274
Hybrid ceramic membrane	BOT, FA, clay	Membrane	Two-chamber	—	22.38 mW m^{-2}	275

respectively), and better performance than Pt/C with respect to methanol tolerance and electrochemical stability in alkaline medium. This is attributed to the large surface area (1103.9 m^2 g^{-1}) of the pomelo peel-derived N-doped carbon and its synergistic effect with Fe_2N. Consequently, the Fe–N-PPC catalysts exhibited great efficiency for application in AFCs. N,P-doped porous carbon cathode catalysts were produced *via* the one-step activation of coconut shells using PA/urea (P/N source), and then pyrolyzed at 1000 °C.[278] The activation process increased the porosity and mesoporous volume of the material, while the doping process improved its electrocatalytic activity towards the ORR in O_2-saturated 0.1 M KOH. According to the CV results, enhanced ORR activity for AC-F-U-P (AC after functionalization, urea impregnation, and pyrolysis) was observed. In addition, a positive shift from −0.17 V (AC-P, AC after pyrolysis at 1000 °C) to −0.02 V (AC-F-U-P) was observed in the onset potential of the catalysts with that of the AC-F-U-P close to commercial Pt–C. The best ORR activity of AC-F-U-P was attributed to its high surface area, mesoporous structure, and high N content. Moreover, the prepared catalysts had superior long-term stability and tolerance towards methanol oxidation compared to a commercial catalyst (20 wt% Pt supported on CB). In another work, nitrogen and oxygen dual-doped carbon (NODC) derived from poplar catkins was synthesized as a catalyst for AFCs.[279] The NODCs were prepared *via* pyrolysis at different heating temperatures, and among them, NODC-800 (pyrolyzed at 800 °C), with the highest surface area of 1462.5 m^2 g^{-1}, exhibited excellent ORR behavior compared to Pt/C in alkaline conditions. In the presence of N_2 or CO, NODC-800 was resistant to CO, while the Pt/C presented a sharp decay in ORR current. NODC-800 had also good resistance to the methanol crossover effect and exhibited significant selectivity for the ORR.

3.8 Nature-inspired materials as membranes or catalysts for SOFCs

3.8.1. Membranes. Sharma and Singh utilized a WSA-derived silicate glass-ceramic and studied its interconnection with Crofer 22 APU for SOFC application.[280] The WSA glass-ceramic displayed insulating properties and great thermal stability at 300–900 °C with a thermal expansion coefficient of about 10 × 10^{-6} $°C^{-1}$, which is in the desired range for SOFC application. A smooth and nonporous interface with good adhesion between glass-ceramic and Crofer 22 APU was formed, which displayed no separation during five thermal cycles.

3.8.2. Catalysts. The synthesis of highly crystalline perovskite $Sm_{0.5}Sr_{0.5}CoO_3$ (SSC) ceramics was proposed using an ESM template.[281] The as-prepared ceramics were used in the form of ceramic clusters to construct cathodes for SOFCs at the high operating temperatures of 500 and 600 °C. The cathode features of SSC clusters were compared with the as-prepared ceramic cathode through the conventional combustion method. Compared to the cell with SSC-C (SSC NPs), the maximum power density of the cells with the SSC clusters was enhanced (372.9–538.8 mW cm^{-2}) by 44.5% at 600 °C. A 29.8% increase also appeared for the maximum power density at 500 °C (201.2–261.4 mW cm^{-2}). This suitable performance of the fuel cells

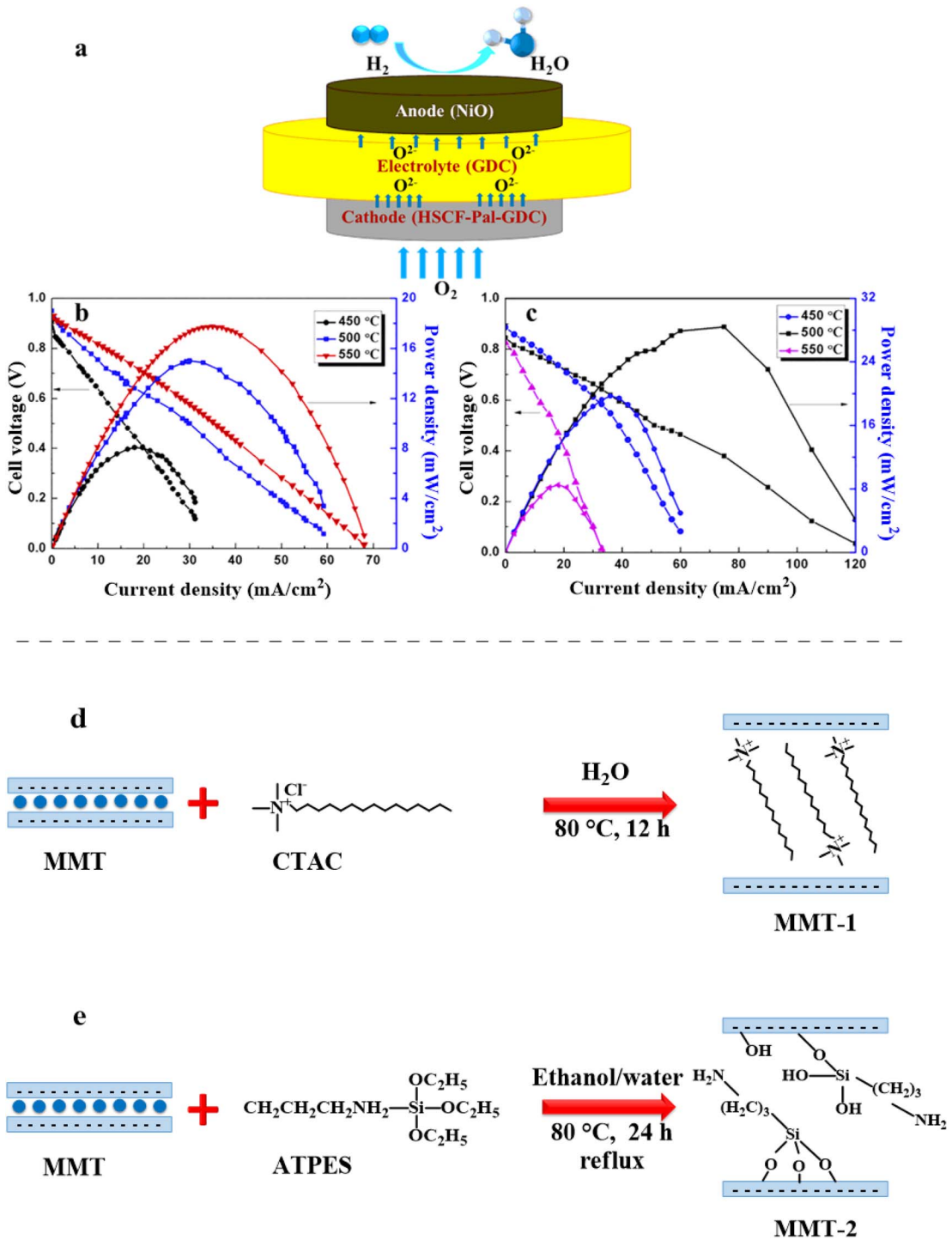

Fig. 23 (a) Schematic illustration of the cell with GDC electrolyte and *IV–IP* curves of a single cell with (b) HSCF cathodes and (c) HSCF-Pal as cathodes in 99% H_2 at different temperatures. Reprinted with permission from ref. 283. Copyright (2018), Elsevier. (d and e) Schematic representation of modification processes of MMT. Reprinted with permission from ref. 292. Copyright (2015), Elsevier.

with SSC clusters was ascribed to their large cathode active area and low electrode polarization. In another report, the performance of an SOFC with a 3D interwoven fibrous $Sm_{0.5}Sr_{0.5}CoO_3$ (SSC)/$Ce_{0.8}Sm_{0.2}O_{1.9}$ (SDC) cathode was compared with a cell containing an SSC cluster/SDC cathode.[282] To prepare the interconnected fibrous SSC/SDC cathode, an ESM-templated SSC sheet was sintered on an Ni/SDC anode-supported SDC electrolyte surface, and then a layer of SDC was coated on the SSC fibers. According to the current–power curves, the maximum power densities of the fibrous SSC/SDC cathode were 843.7 and 489.8 mW cm^{-2} at 600 °C and 500 °C, which were 56.6% and 46.1% higher than that of the SSC cluster/SDC cathode, respectively. These great performances of the SSC/SDC cathode were attributed to its low electrode polarization resistances and cell ohmic resistances.

Zhu *et al.* reported the synthesis of a novel composite containing porous PGS and $Ho_{0.9}Sr_{0.1}Cr_{0.5}Fe_{0.5}O_{3-\delta}$ (HSCF) perovskite as a cathode for SOFCs.[283] The blending of PGS with HSCF enhanced the surface area from 0.18 m^2 g^{-1} to 4.23 m^2 g^{-1} and improved the performance of a single solid oxide fuel cell in which NiO and GDC ($Ce_{0.8}Gd_{0.2}O_{1.9}$) were used as the anode and electrolyte, respectively (Fig. 23a). The functionality of the single cell increased with the addition of PGS, particularly at the current density of 50 mA cm^{-2}. The maximum power densities of the single-cell, fueled by 99% H_2/N_2 were reported to be 14.32 mW cm^{-2} without Pal and 28.43 mW cm^{-2} with PGS at 500 °C (Fig. 23b and c), respectively. The functionality of the fuel cell drastically decreased at higher temperatures owing to the reduction in porosity and charge transfer blocking.

AC derived from palm oil EFB with a high surface area as a pore-former could be utilized to modify nickel oxide-NiO-yttrium-doped barium cerate zirconate (NiO-BCZY64 (BCZY64 = $BaCe_{0.54}Zr_{0.36}Y_{0.1}O_{2.95}$)) as an anode for SOFCs.[284] The modified composite (NiO-m-BCZY64) with gradient anode functional layer (G-AFL) was superior in terms of the maximum power density (166.0 nW cm^{-2} at 800 °C) and the total resistance (21.12 Ω cm^2 at 800 °C) to the unmodified composite, which exhibited a power density of 65.0 nW cm^{-2} and total resistance of 145.64 Ω cm^2. The highest conductivity was reported to be 6.86×10^{-3} S cm^{-1} at 800 °C.

3.9 Other fuel cells

ZAFCs are considered ideal metal–air fuel cell systems, which are different from zinc–air batteries by fuel resupply. Generally, ZAFCs consist of an alkaline electrolyte, an interchangeable reservoir of Zn at the anode, a polymeric separator, and an air cathode, which commonly contains a low-cost metal catalyst. The major benefits of ZAFCs *vs.* PEMFCs are their inexpensive design (namely possessing non-precious catalysts, low-cost Zn restoring apparatus, and inexpensive membranes, without bipolar plates and hydrogen sensors), safe fuel storage, and low maintenance costs. These merits make the commercialization of ZAFCs more practical than PEMFCs.[285] Their fuel cell reactions are as follows:

$$Zn + 2OH^- \rightarrow ZnO + H_2O + 2e^- \text{ (anode reaction)} \quad (18)$$

$$\tfrac{1}{2}O_2 + H_2O + 2e^- \rightarrow 2OH^- \text{ (cathode reaction)} \quad (19)$$

$$Zn + \tfrac{1}{2}O_2 \rightarrow ZnO \text{ (overall reaction)} \quad (20)$$

In 2008, an MEA with four layers was prepared using MMT clay, CB, $KMnO_4$, and hydrophobic PTFE for improving the air-electrode of a ZAFC.[286] MMT was employed to disperse CB, while the MnO_2 catalyst was used to increase the functionality of the air-electrode. The ZAFC with CB/clay/MnO_2/PTFE air-electrode exhibited an excellent performance in the presence of KOH electrolyte in the Zn anode and displayed a power density and current density of 6 mW cm^{-2} and 10 mA cm^{-2} (with no electrolyte permeation), respectively. The addition of MMT improved its performance due to the reduction of CB agglomeration.

DFAFCs operate similar to all PEM-based fuel cells, with formic acid (HCOOH) as the inlet fuel. The reactions in DFAFCs are described as follows:

$$HCOOH \rightarrow CO_2 + 2H^+ + 2e^- \text{ (anode reaction)} \quad (21)$$

$$\tfrac{1}{2}O_2 + 2H^+ + 2e^- \rightarrow H_2O \text{ (cathode reaction)} \quad (22)$$

$$HCOOH + \tfrac{1}{2}O_2 \rightarrow CO_2 + H_2O \text{ (overall cell reaction)} \quad (23)$$

The main drawback of formic acid fuel is its remarkably lower energy density compared to pure methanol. However, this can be rectified using a high concentration of formic acid. Therefore, for many technologies, mostly small-scale power systems, DFAFC are more beneficial than DMFCs.[287,288] For instance, a synthesized nitrogen-based composite, with MMT support and NC was employed in a DFAFC.[289] MMT–N_xC was fabricated *via* the carbonization of MMT, covered with PANi, and then heating of MMT-PANi. The Pd/MMT–N_xC catalysts displayed a uniform dispersion of Pd NPs and showed high catalytic activity for formic acid oxidation compared to traditional Pd/C catalysts. The Pd/MMT–N_xC catalyst exhibited the oxidation current density of 763.5 mA mg_{Pd}^{-1}, performing better than the Pd/C and Pd/MMT catalysts with high stability after 3000 s because of its high specific ECSA and greater electrical conductivity.

AEMFCs include AEMs, which are a new alternative type of fuel cell to replace traditional AFCs with liquid electrolytes and work based on a similar principle to PEMFCs. However, in AEMFCs, the OH^- ions move across the electrolyte from the cathode to the anode and react with hydrogen at the anode to generate water and release electrons. The anode and cathode reactions in AEMFCs are the same as AFCs (eqn (12)–(14)). However, AEM systems present remarkable superiority compared to liquid electrolyte systems with respect to their better CO_2 tolerance and decreased gas crossover.[290] N-doped hierarchically mesoporous carbon-based electrocatalysts, metal-free gram flour-derived mesoporous carbon (GFMC), and soybean-derived mesoporous carbon (SBMC) showed significant catalytic activity toward the ORR in alkaline solution due to their high conductivity and porosity, suggesting they are suitable electrocatalysts for application in AEMFCs.[291] These

electrocatalysts were synthesized by the Ludox solution pyrolysis process with no *in situ* or complex post-synthesis processing. The SBMC sample had a lower surface area and conductivity than GFMC. The onset potential for GFMC was close to that of commercial 20% Pt/C, while its ORR current density was lower than that of Pt/C. Thus, efforts toward optimization are required to increase the functionality of the electrocatalysts. As-fabricated quaternized PSF (QPSF)/functionalized MMT nanocomposite (Fig. 23d and e) membranes could be introduced as effective membranes for AEMFCs through the solution casting method.[292] The water uptake of nanocomposite membranes was less than that of the alkaline QPSF (QPSF-OH) membrane due to the interactions between MMT and the QPSF chain. The nanocomposite membrane comprised of 5% of MMT-1 (MMT with long hydrophobic alkyl group) had the least water uptake (reduced to 101.6%) and the highest ionic conductivity (4.73×10^{-2} S cm^{-1}) at 95 °C, indicating the superior potential of this nanocomposite membrane for use in AEMFCs.

Affordable carbonaceous materials are known as suitable catalysts for the ORR. Two different metal-free carbonaceous catalysts were synthesized using GU and Fu as carbon precursors *via* a template-assisted synthesis method. These catalysts exhibited significant methanol tolerance and high retention in diffusion limiting current density compared with the Pt/C catalyst. The GU catalyst had thin carbon layers with an irregular flaky morphology with no repetition of halloysite structure.[293] In contrast, FU possessed a rod-like morphology with each rod linked together and had a higher surface area (824 m^2 g^{-1}) than GU. The as-prepared carbonaceous catalysts were applied as cathodes in a single-cell H_2/O_2 AEMFC, where the rod-like N-doped carbonaceous material (FU) displayed the maximum power density of 703 mW cm^{-2} at 60 °C with 83% RH, while that of the Pt/C cathode was 1106 mW cm^{-2}.

DCFCs are devices that can directly generate electricity from solid carbon fuels or the oxidation of solid carbon-based matter to electrical energy in one-step conversion at a much higher potential efficiency than the reforming process. However, DCFCs are less commercialized than gas-fuelled SOFCs. Hydrocarbon fuels such as coal, graphite, and biomass are inexpensive, available, and abundant. DCFCs operate at lower temperatures than the combustion or gasification temperatures of fuels, although they are still high, generally between 600–900 °C depending on the cell design and electrolyte type.[294] The following reactions occur in a DCFC:

$$C + 2O^{2-} \rightarrow CO_2 + 4e^- \text{ (anode reaction)} \quad (24)$$

$$O_2 + 4e^- \rightarrow 2O^{2-} \text{ (cathode reaction)} \quad (25)$$

$$C + O_2 \rightarrow CO_2 \text{ (overall cell reaction)} \quad (26)$$

For instance, kaolin was used as an additive mineral in ternary carbonate eutectic ($(Li,Na,K)_2CO_3$) electrolytes to improve the functionality of DCFCs with a half-cell configuration, eradicating mass transfer restrictions.[295] The melting point of the eutectic electrolyte was reduced by adding 5 wt% kaolin, while it increased with an increase in the kaolin content from 10 to 15 wt% due to the dissolution of kaolin in the electrolyte. Furthermore, the melting point was not enhanced with the addition of 20 wt% kaolin due to the saturation limit of kaolin in the electrolyte melt. The dissolution of kaolin in the electrolyte led to a reduction in its activation energy for melting compared to the pure eutectic electrolyte. The addition of kaolin led to a decline in CO_2 dissolution in the melt and enhanced the electrochemical activity. The rate of graphite electrolyte electro-oxidation also increased with addition of kaolin. In this case, kaolin acted as a catalyst and delivered an advanced mechanistic route for the electro-oxidation of graphite. A current density of 17.68 mA cm^{-2} was reported for the pure electrolyte; meanwhile, the electrolyte containing 15 wt% kaolin had a maximum current density of 162 mA cm^{-2} at 600 °C.

4. Summary and discussion

Fuel cells, as electrochemical cells, can convert the chemical energy of fuels into electricity through redox reactions. However, fuel cells require advanced cost-effective, abundant, and efficient materials to overcome their challenges for wide utilization in energy applications and in becoming commercial devices. In this case, nature-inspired materials are rapidly developing for clean energy storage and conversion applications but are still in their infancy. These materials with significant porosity and surface area can be effectively applied in fuel cells, leading to a reduction in the cost for the manufacture of fuel cells. In this review, we summarized the advancements in the electrochemical properties of nature-based energy materials in fuel cells. Mineral clays and aluminosilicates are widely applied as two main natural materials to fabricate membranes with high ionic conductivity and thermal resistance. In addition, low-cost ceramic membranes, a great alternative to polymeric membranes, are prepared from clays and zeolites, which showed a comparable performance to polymeric membranes in fuel cells. Thermal modification of organic wastes and biomass has been reported as an approach to produce carbon-based materials with high surface area and porous structure, providing outstanding electrochemical activity even at high temperatures. Among the different types of fuel cells, clays and aluminosilicates are widely applied to manufacture membranes compared to electrocatalysts. Although, they do not have high electrical conductivity, their addition to polymers such as Nafion® and SPEEK can enhance the conductivity of polymeric membranes. However, HNT, PGS, and zeolites can be used to synthesize electrocatalysts due to their unique structures. It has been found that the utilization of m-MMT for the preparation of membranes or catalysts can improve the fuel cell performance. Although biomass is widely employed to drive different carbon-based materials such as AC and graphene, which were introduced as great substrates to stabilize metal or metal oxide NPs, it is worth mentioning that the loading of metal catalysts such as Pt, Ru, and Fe on carbon-derived biomass leads to better activity than the commercial Pt/C because the porous structures of the synthesized carbon can enable the good dispersion of metallic catalysts. According to our investigation, there are few

Table 6 Comparing the performance of natural-inspired materials for PEMFCs

Membrane/catalyst	Natural material	Measurement conditions	Results	Ref.
Nafion/analcime	Analcime	Temperature of 80 °C with 99.9% RH	Maximum proton conductivity of 0.4373 S cm^{-1} High water uptake compared with Nafion	142
SPEEK/analcime	Analcime	Temperature of 90 °C with 100% RH	Maximum proton conductivity of 0.4016 S cm^{-1} Low water uptake compared with SPEEK	143
Sulfonated MMT/SPSU-BP/PTFE	MMT	Temperature of 90 °C	Proton conductivity of 0.073 S cm^{-1} High water uptake compared with SPSU-BP	165
Pt/PGS@nitrogen-doped graphitic layer	PGS	N_2-saturated 0.5 mol L^{-1} H_2SO_4 electrolyte	ECSA of 32.3 m^2 g^{-1} Mass activity of 68.7 mA mg^{-1} Pt Better catalytic activity toward ORR compared with Pt/C	93
PBI-doped PA	MMT	Temperature of 160 °C with 20% RH	Maximum proton conductivity of 436 mS cm^{-1} Better mechanical properties compared with commercial Celtec®-P membrane	147
Nafion-sulfonated SEP	SEP	Temperature of 25 °C with 100% RH for conductivity measurement Fuel cell operating temperature of 100 °C with 50% RH	Significant conductivity (close to Nafion®) Water uptake of 38 wt% More output power compared with Nafion®	166
Nitrogen and sulfur co-doped bio-carbon flocs	Chicken feather	O_2-saturated 0.1 M KOH solution or 1 M $HClO_4$	ORR kinetic current density of 5.89–8.11 mA cm^{-2} Better performance compared with Pt/C	159
Pt/AC	Orange peel	Fuel cell operating temperature of 60 °C with 100% RH	Electroactive surface area of 17.8 m^2 g^{-1} Power density of 19 mW cm^{-2}	161
IL confined in SNRs/ABPBI	SEP	Temperature of 180 °C with 0% RH for proton conductivity measurement Fuel cell operating temperature of 180 °C with 0% RH	Maximum proton conductivity of 0.048 S cm^{-1} Optimal power density of 0.28 W cm^{-2}	155
Pt/mesoporous carbon	Mushroom	N_2-saturated 0.1 M $HClO_4$ electrolyte solution	ECSA of 62 m^2 g^{-1} Onset potential of 0.91 V Tafel slope of 60 mV dec^{-1} Higher durability than Pt/C Specific activity of 0.0129 mA cm^{-2}	173
Nitrogen and cobalt dual-doped sponge-like carbon (CoNASS)	Soybean straw	O_2-saturated and Ar-saturated 0.1 M KOH solution	Current density of 5.8 mA cm^{-2} Excellent ORR activity with a half-wave potential of 0.786 V, better than Pt/C	174
ABPBI/sulfonated SEP	SEP	Temperature of 90 °C with 98% RH for proton conductivity measurement Fuel cell operating temperature of 180 °C with 0% RH	Proton conductivity of 0.075 S cm^{-1} Water uptake of 35.36% Power density of 0.23 W cm^{-2}	167
CeO_2@HNT-NH_2	HNT	Temperature of 90 °C with 95% RH	Maximum proton conductivity of 160 mS cm^{-1}	152
SPEEK/smectite	Smectite	Temperature of 140 °C with 100% RH	Maximum proton conductivity of 2 × 10^{-2} S cm^{-1} High water uptake compared with SPEEK	144
SPEEK/LDH/SEP	SEP	Temperature of 110 °C with 100% RH	Proton conductivity of 93 mS cm^{-1} Water uptake of 20%	156
Nitrogen-fluorine-doped carbon	Pomegranate peel	Fuel cell operating temperature of 70 °C with ambient pressure	Maximum power density of 65 mW cm^{-2} Current density of 145 mA cm^{-2} Superior electrocatalytic activity toward ORR in comparison with Pt/C	176

Table 6 (*Contd.*)

Membrane/catalyst	Natural material	Measurement conditions	Results	Ref.
Pt/C/Nafion/zeolite	Zeolite	Fuel cell operating temperature of 60 °C with low-humidity conditions	Current density of 0.5 A cm^{-2}	177
PA-doped ABPBI-MMT/PVAl	MMT	Temperature of 140 °C with 100% RH	Proton conductivity of 0.157 S cm^{-1} Water uptake of 40% Power density of 1100 mW cm^{-2}	171
0.5GO@mMMT/Nafion	MMT	Temperature of 80 °C with 98% RH	Proton conductivity of 36.4 mS cm^{-1} Power density of 546 mW cm^{-2}	149
ABPBI/5IL@HNTs	HNTs	Temperature of 160 °C with 0% RH	Proton conductivity of 45 mS cm^{-1} Power density of 380 mW cm^{-2}	154

reports based on the use of these materials in the manufacture of membranes. The operating parameters have a remarkable influence on the performance of fuel cells. According to the literature, the operating temperature is an important parameter that strongly affects the performance of fuel cells. It was found that the performance of a fuel cell was enhanced with an increase in its operating temperature, possibly due to the high mass transfer and conductivity of the membrane at high temperatures. The fuel concentration is another important parameter, where a better performance has been observed at higher concentrations of fuel. Therefore, nature-inspired materials can be used as abundant and affordable materials for designing membranes with high conductivity and porosity, and the synthesis of electrocatalysts with high activity and unique structures for fuel cells. It is worth mentioning that composites based on nature-inspired materials can be used in fuel cells at high operating temperatures such as SOFCs. The comparison of the performances of these materials did not indicate any special results because the measurement conditions varied, as summarized in Table 6, for PEMFCs. In addition, the application of these materials brings challenges, which will be discussed in the next section. However, these materials are derived from nature and will return to nature when discarded.

5. Conclusion and future perspective

In this review, we discussed the utilization of nature-inspired materials as low-cost and abundant materials in fuel cell manufacturing. Nature-based materials are ideal candidates for the production of fuel cell systems in the future due to their high raw material availability, environmental safety, large surface area, small-sized particles, porous structure, superior biocompatibility and biodegradability, high electrochemical activity, and low cost. The cost-effectiveness and approachability of raw natural materials are significantly beneficial in terms of the economic aspects of preparing nanocatalysts and nanocomposite membranes, and thereby their commercialization. Furthermore, they can be modified *via* suitable methods to increase their chemical and physical properties. They have high efficiency to stabilize NPs, and consequently prepare sustainable catalytic structures to improve the electrodes of fuel cells. They can also be incorporated in the polymer as a filler for the improvement of combustibility, mechanical and chemical properties, hydrophilicity, and ionic conductivity of polymeric nanocomposites. However, the application of natural materials may have some challenges, which require further study.

Lignocellulosic biomass is the most abundant and accessible biomass resource, currently underused. Lignocellulosic biomass includes a broad range of biomass types, namely, forest residues, wood, agricultural residues, energy crops, and industry wastes (forestry, and agri-food). This proposed strategy increases the desire to harvest biomass that should be permanently procured from forests, agricultural wastes, and other sources. The major part of the unutilized residues of agriculture and forests is necessary for soil safety, and when eliminated, alternative mineral resources and organic compounds are required. Agricultural residues are burned to clean the land, making it suitable for replantation, resulting in pollution problems. Although this is generally forbidden, it is still performed in many areas. Some residues can form large layers on the surface of the land. In addition, methane gas can be produced under anaerobic conditions, which is a hazardous greenhouse gas contributing to climate change, for example, accumulated sugarcane waste. Thus, the harvesting of agricultural residues can be beneficial to the environment because it prevents the release of methane gas from the trash layers, which leads to public health and pest problems. Also, agricultural residues can be utilized for several local applications, namely, animal nourishment and bedding. However, the supply is often more than the local claim for these aims. Moreover, most of the industrial residues are not utilized properly and are wasted, for example, EFB from palm oil mills. Therefore, biomass can be applied for use in green technologies, but currently is not efficiently used and cannot be employed as an alternative to fossil fuels. The cost of the biomass is the lowest where it is generated. However, the collection and transportation of biomass increase its cost more than expected. Also, when the production of biomass is performed in a special season, such as corn stover or straw, the price of local storage will also increase; particularly for the bulky and wet biomass. In addition, the storage of biomass is challenging because it is prone to degradation. It is worth mentioning that in an area with high biomass availability, this is not guaranteed over a long period because the

crop production may change over time, increasing its cost for suppliers. In addition, floods, drought, and other unpredictable natural disasters may interrupt the supply. There is also the probability of quality changes owing to seasonal changes and the cultivation and harvest of products. Besides, nature-inspired (nano)materials contain some impurities. Iron-based compounds are the major impurities for clays and zeolites, which can affect their electrochemical performance. Easy access to high-quality clays and zeolite, and also finding reasonably priced and effective routes for the purification of clays and zeolite should be extensively studied. Moreover, the production of protonic ceramic membranes from different biowastes and natural aluminosilicates for the fuel cells can be employed as a significant alternative to polymeric membranes. Biomass materials also need high energy conversion. In addition, biomass burning releases toxic emissions such as soot, particulate matter, carbon monoxide, methane, and volatile organic compounds, which have acute respiratory effects on humans.

The water uptake, thermal stability, mechanical resistance, and proton conductivity of PEMs are increased by controlling the loading of nanoclays and zeolites, homogeneous dispersion, and long chain functional groups, boosting the performance of fuel cells at high temperature and low RH. Therefore, their properties make polymer/natural aluminosilicate composite membranes promising compounds for utilization in fuel cells. However, research and experimental assays should be performed to achieve a better understanding of the effect of the size of clay NPs on the features of PEMs and fuel cell performances. The chemical stability of PEMs is also important for future studies.

According to the literature, these natural materials are more used for improving the membrane performance. Hence, their performance as catalysts or catalyst supports can be investigated in future research. Some biomass can be used as the main carbon-based material source and different morphologies of carbon-based materials can be acquired. However, more investigations should be performed on the effect of these carbon materials on the performance of fuel cells, given that they can be efficiently used as catalyst supports due to their good porosity and high surface area. However, the application of affordable approaches for biomass conversion to carbon materials must be investigated. Direct usage of carbon and nitrogen sources such as SHS instead of chitin and CS due to their high abundance and environmentally friendly nature can be further examined for the synthesis of membranes and catalysts.

Pt is known as the most useful catalyst in fuel cells due to its high electrocatalytic activity; however, its production and use are not affordable. In this case, different metallic electrocatalysts such as Pd, Au, and Ag are good candidates to replace Pt. In addition, metal oxides such as Fe_3O_4, TiO_2, and WO_x can improve the output of fuel cells due to their high chemical and electrochemical stability, abundant hydroxyl groups on their surfaces, and low cost. Therefore, applying composites of these affordable catalysts with natural materials can be tested in fuel cells.

Although the fuel cell system is known as an efficient energy producer, there are still many challenges associated with its commercialization. The cost of making a fuel cell is one of the major problems. Thus, the utilization of affordable materials can be beneficial in the reduction of costs. The lifetime and durability of fuel cells are other key issues, which need extensive research. The reduction of the size and weight of the fuel cell system is necessary for transportation applications. The management of the water and incoming gas is important, where a low water content results in membrane drying, while a high water content results in membrane blocking. In addition, the temperature and pressure of the fuel cells must be controlled. Fuel cells exhibit a low voltage, and thus power electronic interfaces are employed for voltage reinforcement. The slower dynamics and higher current ripple are other important limitations of the fuel cells, requiring further investigations. Therefore, future attempts should be focused on overcoming the challenges associated with the commercialization of nature-based composites and using them in fuel cell systems on an industrial scale.

By overcoming these restrictions, nature-inspired-(nano) materials can deliver great benefits to the next generation of fuel cells.

Abbreviations

1D	One-dimensional
3D	Three-dimensional
ABPBI	Poly(2,5-benzimidazole)
AC	Activated carbon
AEM	Anionic exchange membrane
AFCs	Alkaline fuel cells
AMPS	2-Acrylamido-2-methyl-1-propanesulfonic acid
ATP	Attapulgite
BOD	Biochemical oxygen demand
BOT	Bentonite
BTA	Amino benzotriazole
CB	Carbon black
CE	Coulombic efficiency
CPE	Carbon paste electrode
CNTs	Carbon nanotubes
COD	Chemical oxygen demand
CS	Chitosan
CSE	Chesnut shell electrode
CTE	Coefficients of the thermal expansion
CV	Cyclic voltammetry
CVD	Chemical vapor deposition
DEFCs	Direct ethanol fuel cells
DFAFCs	Direct formic acid fuel cells
DMDOC	Dimethyl dioctadecyl ammonium chloride
DMFCs	Direct methanol fuel cells
DW	Deionized water
ECSA	Electrochemical surface area
EFBs	Empty fruit bunches
EFCs	Enzymatic fuel cells
ESM	Eggshell membrane
FA	Fly ash

FR	Feather rachis
FU	Furfural
GC	Graphitic carbon
GCN	Graphitic carbon nanosheets
GO	Graphene oxide
GPTMS	3-Glicidoxy propyltrimethoxysilane
GQDs	Graphene quantum dots
GU	Glucose
HDTA	Hexadecyl trimethylammonium chloride
HFP	Hexafluoro propylene
HGCN	Graphene-like carbon nanosheets
HNTs	Halloysite nanotubes
HOR	Hydrogen oxidation reaction
HPC	Hierarchical porous carbon
IEC	Ion-exchange capacity
IL	Ionic liquid
Krytox	Carboxylic acid-terminated perfluoropolyether
LDH	Layered double hydroxide
LSV	Linear sweep voltammetry
MCFCs	Molten carbonate fuel cells
MFCs	Microbial fuel cells
MEA	Membrane electrode assembly
MMT	Montmorillonite
mMMT	Microbial montmorillonite
m-MMT	Modified montmorillonite
MOR	Methanol oxidation reaction
MoS_2	Molybdenum disulfide
MPC	Mangosteen peel carbon
NC	Nitrogen-doped carbon
NF	Nanofiber
NG	Nitrogen doped-graphene
NPs	Nanoparticles
OCV	Open circuit voltage
OMMT	Organic montmorillonite
QATP	Organic-modified attapulgite
ORR	Oxygen reduction reaction
PA	Phosphoric acid
PAFCs	Phosphoric acid fuel cells
PANi	Polyaniline
PBI	Polybenzimidazole
PEI	Polyethyleneimine
PEM	Polymer electrolyte membrane
PEMFCs	Proton exchange membrane fuel cells
PFPE–NR_3	Ammonium perfluoropolyether
PGS	Palygorskite
PhetaTfO	Phenylethylammonium trifluoromethanesulfonate
POP	Poly(oxyalkylene)amines
POPD400	Poly(propylene oxide)
PPy	Polypyrrole
PS	1,3-Propane sultone
PSSA	Poly(styrene sulfonic acid)
PSF	Polysulfone
PTFE	Polytetrafluoroethylene
PVA	Polyvinyl alcohol
PVDF	Polyvinylidene fluoride
PWA	Phosphotungstic acid
RH	Relative humidity
RHA	Rice husk ash
RVC	Reticulated vitreous carbon
SA	Sulfanilic acid
SC	Sludge carbon
SCE	Saturated calomel electrode
SEP	Sepiolite
SEPNR	Sepiolite nanorod
SHS	Shrimp shells
SMFCs	Soil microbial fuel cells
SNR	Silicon nanorods
SOFCs	Solid oxide fuel cells
SPEEK	Sulfonated poly(ether ether ketone)
SPI	Sulfonated polyimide
SPSU-BP	Sulfonated poly(biphenyl ether sulfone)
SS	Sewage sludge
URFC	Unitized regenerative fuel cell
WC	Tungsten carbide
WSA	Wheat straw ash

Conflicts of interest

The authors declare no competing financial interest.

Acknowledgements

We gratefully acknowledge from the Iranian Nano Council, Bu-Ali Sina University and the University of Qom for the support of this work. MBG acknowledged the DST-SERB (CRG/2021/001738) core research grant.

References

1 S. Kamarudin, W. Daud, A. M. Som, A. Mohammad, S. Takriff and M. Masdar, *J. Chem. Eng.*, 2004, **103**, 99.
2 B. Jaleh, M. Nasrollahzadeh, M. Eslamipanah, A. Nasri, E. Shabanlou, N. R. Manwar, R. Zboril, P. Fornasiero and M. B. Gawande, *Carbon*, 2022, **198**, 301.
3 R. Kaur, A. Marwaha, V. A. Chhabra, K.-H. Kim and S. Tripathi, *Renewable Sustainable Energy Rev.*, 2020, **119**, 109551.
4 X. Ren, Q. Lv, L. Liu, B. Liu, Y. Wang, A. Liu and G. Wu, *Sustainable Energy Fuels*, 2020, **4**, 15.
5 N. Seselj, C. Engelbrekt and J. Zhang, *Sci. Bull.*, 2015, **60**, 864.
6 A. Dicks and D. A. J. Rand, *Fuel Cell Systems Explained*, Wiley Online Library, 2018.
7 K. Scott, E. H. Yu, M. M. Ghangrekar, B. Erable and N. M. Duțeanu, Biological and microbial fuel cells, in *Comprehensive Renewable Energy*, Elsevier, United States, 2012, vol. 4.
8 Y. Wang and W. H. Zhong, *ChemElectroChem*, 2015, **2**, 22.
9 L. Yue, Y. Xie, Y. Zheng, W. He, S. Guo, Y. Sun, T. Zhang and S. Liu, *Compos. Sci. Technol.*, 2017, **145**, 122.
10 R. Borup, J. Meyers, B. Pivovar, Y. S. Kim, R. Mukundan, N. Garland, D. Myers, M. Wilson, F. Garzon and D. Wood, *Chem. Rev.*, 2007, **107**, 3904.
11 M. H. Esfe and M. Afrand, *J. Therm. Anal. Calorim.*, 2020, **140**, 1633.

12 C. Zhang, X. Shen, Y. Pan and Z. Peng, *Front. Energy*, 2017, **11**, 268.
13 A. Nasri, B. Jaleh, S. Khazalpour, M. Nasrollahzadeh and M. Shokouhimehr, *Int. J. Biol. Macromol.*, 2020, **164**, 3012.
14 B. F. Mohazzab, A. Akhundi, K. Rahimi, B. Jaleh and A. Z. Moshfegh, *ACS Appl. Energy Mater.*, 2022, **5**(10), 12283–12296.
15 G. Ashrafi, M. Nasrollahzadeh, B. Jaleh, M. Sajjadi and H. Ghafuri, *Adv. Colloid Interface Sci.*, 2022, 102599.
16 C. Xu, M. Nasrollahzadeh, M. Sajjadi, M. Maham, R. Luque and A. R. Puente-Santiago, *Renewable Sustainable Energy Rev.*, 2019, **112**, 195.
17 M. Shahadat, M. Z. Khan, P. F. Rupani, A. Embrandiri, S. Sultana, S. Z. Ahammad, S. W. Ali and T. Sreekrishnan, *Adv. Colloid Interface Sci.*, 2017, **249**, 2.
18 J. Peng and Q. Cheng, *Adv. Mater.*, 2017, **29**, 1702959.
19 Y. Lan, Y. Liu, J. Li, D. Chen, G. He and I. P. Parkin, *Adv. Sci.*, 2021, 2004036.
20 J.-H. Wee, *Renewable Sustainable Energy Rev.*, 2007, **11**, 1720.
21 J.-H. Wee and K.-Y. Lee, *J. Power Sources*, 2006, **157**, 128.
22 K. Sopian and W. R. W. Daud, *Renewable Energy*, 2006, **31**, 719.
23 H. Beydaghi, M. Javanbakht and E. Kowsari, *Ind. Eng. Chem. Res.*, 2014, **53**, 16621.
24 N. A. H. Rosli, K. S. Loh, W. Y. Wong, R. M. Yunus, T. K. Lee, A. Ahmad and S. T. Chong, *Int. J. Mol. Sci.*, 2020, **21**, 632.
25 O. Simya, P. Radhakrishnan, A. Ashok, K. Kavitha and R. Althaf, *Handbook of Nanomaterials for Industrial Applications*; Elsevier BV: Amsterdam, The Netherlands, 2018.
26 V. Vishnyakov, *Vacuum*, 2006, **80**, 1053.
27 A. Z. Weber, S. Balasubramanian and P. K. Das, *Advances in Chemical Engineering*, Elsevier, 2012, ch. 2.
28 J. Wang, C.-X. Zhao, J.-N. Liu, D. Ren, B.-Q. Li, J.-Q. Huang and Q. Zhang, *Nano Mater. Sci.*, 2021, **3**, 313.
29 T. Shen, X. Huang, S. Xi, W. Li, S. Sun and Y. Hou, *J. Energy Chem.*, 2022, **68**, 184.
30 X. Huang, T. Shen, T. Zhang, H. Qiu, X. Gu, Z. Ali and Y. Hou, *Adv. Energy Mater.*, 2020, **10**, 1900375.
31 S. K. Kamarudin, F. Achmad and W. R. W. Daud, *Int. J. Hydrogen Energy*, 2009, **34**, 6902.
32 H. F. Fard, M. Khodaverdi, F. Pourfayaz and M. H. Ahmadi, *Int. J. Hydrogen Energy*, 2020, **45**, 25307.
33 E. Berretti, M. Longhi, P. Atanassov, D. Sebastián, C. L. Vecchio, V. Baglio, A. Serov, A. Marchionni, F. Vizza and C. Santoro, *Curr. Opin. Electrochem.*, 2021, **29**, 100756.
34 A. Odeh, P. Osifo and H. Noemagus, *Energy Sources, Part A*, 2013, **35**, 152.
35 Z. Xia, X. Zhang, H. Sun, S. Wang and G. Sun, *Nano Energy*, 2019, **65**, 104048.
36 M. Akhairi and S. Kamarudin, *Int. J. Hydrogen Energy*, 2016, **41**, 4214.
37 L. Wang, A. Lavacchi, M. Bevilacqua, M. Bellini, P. Fornasiero, J. Filippi, M. Innocenti, A. Marchionni, H. A. Miller and F. Vizza, *ChemCatChem*, 2015, **7**, 2214.
38 L. Wang, M. Bevilacqua, J. Filippi, P. Fornasiero, M. Innocenti, A. Lavacchi, A. Marchionni, H. Miller and F. Vizza, *Appl. Catal. B*, 2015, **165**, 185.
39 F. Vigier, C. Coutanceau, A. Perrard, E. Belgsir and C. Lamy, *J. Appl. Electrochem.*, 2004, **34**, 439.
40 S. Badwal, S. Giddey, A. Kulkarni, J. Goel and S. Basu, *Appl. Energy*, 2015, **145**, 80.
41 M. C. Potter, *Proc. R. Soc. London, Ser. B*, 1911, **84**, 260.
42 B. Cohen, *J. Bacteriol.*, 1931, **21**, 18.
43 R. Kumar, L. Singh, A. Zularisam and F. I. Hai, *Int. J. Energy Res.*, 2018, **42**, 369.
44 S. Aziz, A. R. Memon, S. F. Shah, S. A. Soomro and A. Parkash, *Sci. Int.*, 2013, **25**, 49.
45 S. Pandit, K. Chandrasekhar, R. Kakarla, A. Kadier and V. Jeevitha, *Microbial Applications*, Springer, 2017, vol. 1, p. 165.
46 M. Rahimnejad, A. Adhami, S. Darvari, A. Zirepour and S.-E. Oh, *Alexandria Eng. J.*, 2015, **54**, 745.
47 B. E. Logan, *ChemSusChem*, 2012, **5**, 988.
48 B. E. Logan, B. Hamelers, R. Rozendal, U. Schröder, J. Keller, S. Freguia, P. Aelterman, W. Verstraete and K. Rabaey, *Environ. Sci. Technol.*, 2006, **40**, 5181.
49 G. McLean, T. Niet, S. Prince-Richard and N. Djilali, *Int. J. Hydrogen Energy*, 2002, **27**, 507.
50 J. A. Matelli and E. Bazzo, *J. Power Sources*, 2005, **142**, 160.
51 H. H. Lim, E. Sulistya, M. Y. Wong, B. Salamatinia and B. A. Horri, *Sol-gel Based Nanoceramic Materials: Preparation, Properties and Applications*, Springer, 2017, p. 157.
52 T. Seitarides, C. Athanasiou and A. Zabaniotou, *Renewable Sustainable Energy Rev.*, 2008, **12**, 1251.
53 R. M. Ormerod, *Chem. Soc. Rev.*, 2003, **32**, 17–28.
54 L. de Haart and R. Peters, *Fuel Cells-Solid Oxide Fuel Cells | Internal and External Reformation*, Elsevier, 2009.
55 S. Haider, A. Kausar and B. Muhammad, *Polym.-Plast. Technol. Eng.*, 2017, **56**, 917.
56 M. Furtmair, J. Timm and R. Marschall, *Microporous Mesoporous Mater.*, 2020, 110745.
57 A. A. Shahmansouri, H. A. Bengar and H. AzariJafari, *Constr. Build. Mater.*, 2021, **268**, 121136.
58 S. C. Aboudi Mana, M. M. Hanafiah and A. J. K. Chowdhury, *Geol. Ecol. Landsc.*, 2017, **1**, 155.
59 W. G. Fahrenholtz, *Ceramic and Glass Materials*, Springer, 2008, p. 111.
60 I. Khan, A. H. Bhat, D. K. Sharma, M. A. Usmani and F. Khan, Nanomaterials for Healthcare, *Energy Environ.*, 2019, 199.
61 M. K. Uddin, *J. Chem. Eng.*, 2017, **308**, 438.
62 R. E. Grim, *Science*, 1962, **135**, 890.
63 F. Uddin, *Metall. Mater. Trans. A*, 2008, **39**, 2804.
64 I. Daou, G. L. Lecomte-Nana, N. Tessier-Doyen, C. Peyratout, M. F. Gonon and R. Guinebretiere, *Minerals*, 2020, **10**, 480.
65 C. C. Harvey and H. H. Murray, *Appl. Clay Sci.*, 1997, **11**, 285.
66 S. M.-G. Yek, T. Baran, M. Nasrollahzadeh, R. Bakhshali-Dehkordi, N. Y. Baran and M. Shokouhimehr, *Optik*, 2021, **238**, 166672.

67 B. Biswas, L. N. Warr, E. F. Hilder, N. Goswami, M. M. Rahman, J. G. Churchman, K. Vasilev, G. Pan and R. Naidu, *Chem. Soc. Rev.*, 2019, **48**, 3740.

68 M. Eslamipanah, B. Jaleh, B. F. Mohazzab, S. Khazalpour, M. Nasrollahzadeh and M. Shokouhimehr, *Int. J. Hydrogen Energy*, 2020, **45**, 33771.

69 B. Jaleh, S. S. Mousavi, M. Sajjadi, M. Eslamipanah, M. Jafari Maryaki, Y. Orooji and R. S. Varma, *Chemosphere*, 2023, **315**, 137668.

70 D. Hillel and J. L. Hatfield, *Encyclopedia of Soils in the Environment*, Elsevier Amsterdam, 2005.

71 J. Cui, Z. Zhang and F. Han, *Appl. Clay Sci.*, 2020, **190**, 105543.

72 G. Yuan, H. Zhang, M. Wang, X. Chen, H. Guo and X. Chen, *J. Appl. Polym. Sci.*, 2021, **138**, 49799.

73 S. Chen, X. Yan, W. Liu, R. Qiao, S. Chen, H. Luo and D. Zhang, *J. Chem. Eng.*, 2020, **401**, 126095.

74 L. A. Utracki, B. Broughton, N. González-Rojano, L. H. de Carvalho and C. A. Achete, *Polym. Eng. Sci.*, 2011, **51**, 559.

75 E. R. Dyartanti, A. Purwanto, I. N. Widiasa and H. Susanto, *Membranes*, 2018, **8**, 36.

76 J. Feng, X. Ao, Z. Lei, J. Wang, Y. Deng and C. Wang, *Electrochim. Acta*, 2020, **340**, 135995.

77 Y. Liu, Y. Jiang, F. Li, B. Xue and X. Cao, *J. Electrochem. Soc.*, 2019, **166**, A1082.

78 A. Steudel, F. Friedrich, P. Boháč, W. Lieske, W. Baille, D. König, R. Schuhmann and K. Emmerich, *Appl. Clay Sci.*, 2020, **188**, 105501.

79 S. Ummartyotin, N. Bunnak and H. Manuspiya, *Renewable Sustainable Energy Rev.*, 2016, **61**, 466.

80 Y. Zhu and D. Chen, *Ceram. Int.*, 2017, **43**, 9465.

81 W. Dong, J. Ding, W. Wang, L. Zong, J. Xu and A. Wang, *J. Cleaner Prod.*, 2020, **256**, 120383.

82 P. Muñoz, M. Mendívil, V. Letelier and M. Morales, *Constr. Build. Mater.*, 2019, **224**, 639.

83 D. Plackett, A. Siu, Q. Li, C. Pan, J. O. Jensen, S. F. Nielsen, A. A. Permyakova and N. J. Bjerrum, *J. Membr. Sci.*, 2011, **383**, 78.

84 I. Das, S. Das, S. Sharma and M. Ghangrekar, *Int. J. Hydrogen Energy*, 2020, **45**, 16787.

85 K. Charradi, Z. Ahmed, P. Aranda and R. Chtourou, *Appl. Clay Sci.*, 2019, **174**, 77.

86 H. Doğan, T. Y. Inan, M. Koral and M. Kaya, *Appl. Clay Sci.*, 2011, **52**, 285.

87 S. Sasikala, S. Meenakshi, S. Bhat and A. Sahu, *Electrochim. Acta*, 2014, **135**, 232.

88 F. Altaf, R. Gill, R. Batool, M. Drexler, F. Alamgir, G. Abbas and K. Jacob, *Eur. Polym. J.*, 2019, **110**, 155.

89 Y. Chen, L. Chen, P. Li, Y. Xu, M. Fan, S. Zhu and S. Shen, *Energy*, 2016, **109**, 620.

90 Ş. M. Eskitoros-Togay, Y. E. Bulbul, Z. K. Cınar, A. Sahin and N. Dilsiz, *Int. J. Hydrogen Energy*, 2023, **48**, 280.

91 C. Beauger, G. Lainé, A. Burr, A. Taguet, B. Otazaghine and A. Rigacci, *J. Membr. Sci.*, 2013, **430**, 167.

92 F. Altaf, S. Ahmed, D. Dastan, R. Batool, Z. Rehman, Z. Shi, M. Hameed, P. Bocchetta and K. Jacob, *Mater. Today Chem.*, 2022, **24**, 100843.

93 R. Wang, J. Jia, H. Li, X. Li, H. Wang, Y. Chang, J. Kang and Z. Lei, *Electrochim. Acta*, 2011, **56**, 4526.

94 H. Wang, R. Luo, S. Liao, J. Key, S. Ji and R. Wang, *J. Solid State Electrochem.*, 2013, **17**, 2009–2015.

95 K. Peng, J. Ye, L. Zuo, Y. Wang, H. Wang, M. Niu, L. Su, L. Zhuang and X. Li, *Appl. Clay Sci.*, 2023, **233**, 106798.

96 N. Fadaee Takmil, B. Jaleh, B. Feizi Mohazzab, S. Khazalpour, A. Rostami-Vartooni, T. Hong Chuong Nguyen, X. Cuong Nguyen and R. S. Varma, *Inorg. Chem. Commun.*, 2021, **133**, 108891.

97 E. Koudelková, PhD thesis, University of Pardubice, 2017.

98 C. Colella and F. A. Mumpton, *Natural Zeolites for the Third Millennium*, A. De Frede, 2000.

99 V. J. Inglezakis and A. A. Zorpas, *Handbook of Natural Zeolites*, Bentham Science Publishers, 2012.

100 N. Nikolopoulos, R. G. Geitenbeek, G. T. Whiting and B. M. Weckhuysen, *J. Catal.*, 2021, **396**, 136.

101 J. Kanai, J. A. Martens and P. A. Jacobs, *J. Catal.*, 1992, **133**, 527.

102 S. E. Lehman and S. C. Larsen, *Environ. Sci.: Nano*, 2014, **1**, 200.

103 A. Farkaš, M. Rožić and Ž. Barbarić-Mikočević, *J. Hazard. Mater.*, 2005, **117**, 25.

104 M. Moshoeshoe, M. S. Nadiye-Tabbiruka and V. Obuseng, *Am. J. Mater. Sci.*, 2017, **7**, 196.

105 T. Armbruster and M. E. Gunter, *Rev. Mineral. Geochem.*, 2001, **45**, 1.

106 P. J. Reeve and H. J. Fallowfield, *J. Environ. Manage.*, 2018, **205**, 253.

107 S. Wang and Y. Peng, *Chem. Eng. J.*, 2010, **156**, 11.

108 F. A. Mumpton, *Proc. Natl. Acad. Sci. U. S. A.*, 1999, **96**, 3463.

109 P. Guo, N. Yan, L. Wang and X. Zou, *Cryst. Growth Des.*, 2017, **17**, 6821.

110 S. Hashimoto, *J. Photochem. Photobiol.*, 2003, **4**, 19.

111 M. G. Valdes, A. Perez-Cordoves and M. Díaz-García, *TrAC, Trends Anal. Chem.*, 2006, **25**, 24.

112 M. Sakizci, *Anadolu Üniversitesi Bilim Ve Teknoloji Dergisi A-Uygulamalı Bilimler ve Mühendislik*, 2016, vol. 17, p. 724.

113 Y. Kalvachev, T. Todorova and C. Popov, *Catalysts*, 2021, **11**, 308.

114 Y. Lu, N. Zhu, F. Yin, T. Yang, P. Wu, Z. Dang, M. Liu and X. Wei, *Biosens. Bioelectron.*, 2017, **98**, 350.

115 Y. Zan, Z. Zhang, H. Liu, M. Dou and F. Wang, *J. Mater. Chem.*, 2017, **5**, 24329.

116 D. Wu, Y. Shi, H. Jing, X. Wang, X. Song, D. Si, S. Liang and C. Hao, *Int. J. Hydrogen Energy*, 2018, **43**, 19492.

117 C. Xu, M. Nasrollahzadeh, M. Selva, Z. Issaabadi and R. Luque, *Chem. Soc. Rev.*, 2019, **48**, 4791.

118 J. Jjagwe, P. W. Olupot, E. Menya and H. M. Kalibbala, *J. Bioresour. Bioprod.*, 2021, **6**, 292.

119 Y. Orooji, N. Han, Z. Nezafat, N. Shafiei, Z. Shen, M. Nasrollahzadeh, H. Karimi-Maleh, R. Luque, A. Bokhari and J. J. Klemeš, *J. Cleaner Prod.*, 2022, 131220.

120 K. Bracmort, and R. W. Gorte, *Biomass: Comparison of Definitions in Legislation*, Congressional Research Service, 2009.

121 L. T. Vo and P. Navard, *Constr. Build. Mater.*, 2016, **121**, 161.

122 L. Z. Linan, A. C. M. Cidreira, C. Q. da Rocha, F. F. de Menezes, G. J. de Moraes Rocha and A. E. M. Paiva, *J. Bioresour. Bioprod.*, 2021, **6**, 323.
123 H. Essabir, M. Bensalah, D. Rodrigue, R. Bouhfid and A. Qaiss, *Mech. Mater.*, 2016, **93**, 134.
124 B. D. Mattos, A. L. Misso, P. H. de Cademartori, E. A. de Lima, W. L. Magalhães and D. A. Gatto, *Constr. Build. Mater.*, 2014, **61**, 60.
125 L. Zhang and Y. Hu, *Mater. Des.*, 2014, **55**, 19.
126 H. Xu, H. Zhang, Y. Ouyang, L. Liu and Y. Wang, *Electrochim. Acta*, 2016, **214**, 119.
127 P. Chen, L.-K. Wang, G. Wang, M.-R. Gao, J. Ge, W.-J. Yuan, Y.-H. Shen, A.-J. Xie and S.-H. Yu, *Energy Environ. Sci.*, 2014, **7**, 4095.
128 C. Guo, W. Liao, Z. Li, L. Sun and C. Chen, *Nanoscale*, 2015, **7**, 15990.
129 H. Zhang, Q. Sun, Q. He, Y. Zhang, X. He, T. Gan and H. Ji, *Nano Res.*, 2022, **15**, 5995.
130 Z. Zhu and Z. Xu, *Renewable Sustainable Energy Rev.*, 2020, **134**, 110308.
131 B.-H. Cheng, R. J. Zeng and H. Jiang, *Bioresour. Technol.*, 2017, **246**, 224.
132 J. P. Paraknowitsch and A. Thomas, *Energy Environ. Sci.*, 2013, **6**, 2839.
133 D. S. Doke, J. H. Advani, D. R. Naikwadi, M. B. Gawande, P. Walke, S. B. Umbarkar and A. V. Biradar, *ACS Sustainable Chem. Eng.*, 2019, **7**, 3018.
134 W. Kiciński and S. Dyjak, *Carbon*, 2020, **168**, 748.
135 S. M. Tan and M. Pumera, *ACS Nano*, 2019, **13**, 2681.
136 V. Mazánek, J. Luxa, S. Matějková, J. Kučera, D. Sedmidubský, M. Pumera and Z. k. Sofer, *ACS Nano*, 2019, **13**, 1574.
137 M. K. Hrnčič, G. Kravanja and Ž. Knez, *Energy*, 2016, **116**, 1312.
138 W.-J. Liu, H. Jiang and H.-Q. Yu, *Chem. Rev.*, 2015, **115**, 12251.
139 Z. Zhang, Z. Zhu, B. Shen and L. Liu, *Energy*, 2019, **171**, 581.
140 J. Lee, K. Lee, D. Sohn, Y. M. Kim and K. Y. Park, *Energy*, 2018, **153**, 913.
141 H. S. Kambo and A. Dutta, *Renewable Sustainable Energy Rev.*, 2015, **45**, 359.
142 P. Kongkachuichay and S. Pimprom, *Chem. Eng. Res. Des.*, 2010, **88**, 496.
143 N. Intaraprasit and P. Kongkachuichay, *J. Taiwan Inst. Chem. Eng.*, 2011, **42**, 190.
144 Z. Ahmed, K. Charradi, Q. A. Alsulami, S. M. Keshk and R. Chtourou, *J. Appl. Polym. Sci.*, 2021, **138**, 49634.
145 F. Xu, S. Mu and M. Pan, *J. Membr. Sci.*, 2011, **377**, 134.
146 F. Hu, F. Zhong, S. Wen, G. Zheng, C. Gong, C. Qin and H. Liu, *Polym. Compos.*, 2020, **41**, 2254.
147 F. Ublekov, H. Penchev, V. Georgiev, I. Radev and V. Sinigersky, *Mater. Lett.*, 2014, **135**, 5.
148 C. Simari, G. Potsi, A. Policicchio, I. Perrotta and I. Nicotera, *J. Phys. Chem. C*, 2016, **120**, 2574.
149 Z. Meng, Y. Zou, N. Li, B. Wang, X. Fu, R. Zhang, S. Hu, X. Bao, X. Li, F. Zhao and Q. Liu, *ACS Appl. Energy Mater.*, 2023, **6**, 1771.
150 Y.-H. Pai and C.-W. Tseng, *J. Power Sources*, 2012, **202**, 28.
151 H. Zhang, C. Ma, J. Wang, X. Wang, H. Bai and J. Liu, *Int. J. Hydrogen Energy*, 2014, **39**, 974.
152 A. Akrout, A. Delrue, M. Zatoń, F. Duquet, F. Spanu, M. Taillades-Jacquin, S. Cavaliere, D. Jones and J. Rozière, *Membranes*, 2020, **10**, 208.
153 X. Sun, T. Zhang, X. Liu, H. Ren, Q. Zhang, Y. Feng and H. Ding, *Int. J. Hydrogen Energy*, 2020, **45**, 30673.
154 Q. Liu, C. Xiong, H. Shi, L. Liu, X. Wang, X. Fu, R. Zhang, S. Hu, X. Bao, X. Li, F. Zhao and C. Xu, *J. Membr. Sci.*, 2023, **668**, 121192.
155 X. Zhang, X. Fu, S. Yang, Y. Zhang, R. Zhang, S. Hu, X. Bao, F. Zhao, X. Li and Q. Liu, *J. Mater. Chem. A*, 2019, **7**, 15288.
156 K. Charradi, Z. Ahmed, N. Thmaini, P. Aranda, Y. O. Al-Ghamdi, P. Ocon, S. M. Keshk and R. Chtourou, *J. Appl. Polym. Sci.*, 2021, **138**, 50364.
157 Q. Liu, X. Wang, X. Zhang, Z. Ling, W. Wu, X. Fu, R. Zhang, S. Hu, X. Li, F. Zhao and X. Bao, *J. Cleaner Prod.*, 2022, **359**, 131977.
158 G. Punniakotti, G. Sivasubramanian, S. A. Gurusamy Thangavelu and P. Deivanayagam, *Polym.-Plast. Technol. Mater.*, 2021, **60**, 571.
159 Y. Fang, H. Wang, H. Yu and F. Peng, *Electrochim. Acta*, 2016, **213**, 273.
160 A. Tyagi, A. Yadav, P. Sinha, S. Singh, P. Paik and K. K. Kar, *Appl. Surf. Sci.*, 2019, **495**, 143603.
161 M. Dhelipan, A. Arunchander, A. K. Sahu and D. Kalpana, *J. Saudi Chem. Soc.*, 2017, **21**, 487.
162 C. Felice, S. Ye and D. Qu, *Ind. Eng. Chem. Res.*, 2010, **49**, 1514.
163 S. Ghosh, A. Sannigrahi, S. Maity and T. Jana, *J. Phys. Chem. C*, 2011, **115**, 11474.
164 I. Nicotera, A. Enotiadis, K. Angjeli, L. Coppola, G. A. Ranieri and D. Gournis, *J. Phys. Chem. B*, 2011, **115**, 9087.
165 D. Xing, G. He, Z. Hou, P. Ming and S. Song, *Int. J. Hydrogen Energy*, 2011, **36**, 2177.
166 C. Beauger, G. Lainé, A. Burr, A. Taguet and B. Otazaghine, *J. Membr. Sci.*, 2015, **495**, 392.
167 X. Zhang, Q. Liu, L. Xia, D. Huang, X. Fu, R. Zhang, S. Hu, F. Zhao, X. Li and X. Bao, *J. Membr. Sci.*, 2019, **574**, 282.
168 D. A. Petrova, A. N. Filippov, N. A. Kononenko, S. A. Shkirskaya, M. O. Timchenko, E. V. Ivanov, V. A. Vinokurov and Y. M. Lvov, *J. Membr. Sci.*, 2019, **582**, 172.
169 S. H. Woo, A. Taguet, B. Otazaghine, A. Mosdale, A. Rigacci and C. Beauger, *Electrochim. Acta*, 2019, **319**, 933.
170 J. J. Rubio Arias, S. d. S. Bento, M. d. F. Vieira Marques and A. d. S. Gomes, *J. Appl. Polym. Sci.*, 2021, **138**, 49871.
171 F. Altaf, R. Batool, R. Gill, Z. U. Rehman, H. Majeed, A. Ahmad, M. Shafiq, D. Dastan, G. Abbas and K. Jacob, *Renewable Energy*, 2021, **164**, 709.
172 L. Wang, J. Chen, L. Ge, Z. Zhu and V. Rudolph, *Energy Fuels*, 2011, **25**, 3408.
173 P. Dhanasekaran, A. Shukla, K. N. Krishnan, I. Rongrin, S. V. Selvaganesh, D. Kalpana and S. D. Bhat, *Sustainable Energy Fuels*, 2019, **3**, 1012.

174 G. Lu, Z. Li, W. Fan, M. Wang, S. Yang, J. Li, Z. Chang, H. Sun, S. Liang and Z. Liu, *RSC Adv.*, 2019, **9**, 4843.
175 A. Tyagi, S. Banerjee, S. Singh and K. K. Kar, *Int. J. Hydrogen Energy*, 2020, **45**, 16930.
176 S. Akula, P. Varathan, R. S. Menon and A. K. Sahu, *Sustainable Energy Fuels*, 2021, **5**, 886.
177 A. Kumar, H.-C. Su, Y.-S. Chen and A. Arpornwichanop, *Int. J. Hydrogen Energy*, 2021, **46**, 15878.
178 V. Tricoli and F. Nannetti, *Electrochim. Acta*, 2003, **48**, 2625.
179 V. Baglio, A. Di Blasi, A. S. Aricò, V. Antonucci, P. L. Antonucci, F. Nannetti and V. Tricoli, *Electrochim. Acta*, 2005, **50**, 5181.
180 H. Bai, H. Zhang, Y. He, J. Liu, B. Zhang and J. Wang, *J. Membr. Sci.*, 2014, **454**, 220.
181 A. K. Beheshti Marnani, M. B. Askari and A. Hatefi-Mehrjardi, *Int. J. Hydrogen Energy*, 2017, **42**, 16741.
182 W.-C. Tsen, *Nanomaterials*, 2020, **10**, 1641.
183 Z. Gaowen and Z. Zhentao, *J. Membr. Sci.*, 2005, **261**, 107.
184 J.-M. Thomassin, C. Pagnoulle, D. Bizzari, G. Caldarella, A. Germain and R. Jérôme, *Solid State Ionics*, 2006, **177**, 1137.
185 S.-W. Chuang, S. L.-C. Hsu and C.-L. Hsu, *J. Power Sources*, 2007, **168**, 172.
186 C.-C. Yang, *Int. J. Hydrogen Energy*, 2011, **36**, 4419.
187 M. M. Hasani-Sadrabadi, S. R. Ghaffarian and P. Renaud, *RSC Adv.*, 2013, **3**, 19357.
188 S. K. Nataraj, C.-H. Wang, H.-C. Huang, H.-Y. Du, L.-C. Chen and K.-H. Chen, *ACS Sustainable Chem. Eng.*, 2015, **3**, 302.
189 M. H. Sheikh-Mohseni, S. Sedaghat, P. Derakhshi and A. Safekordi, *Chin. J. Chem. Eng.*, 2020, **28**, 2555.
190 Y. Wang, G. Han, Z. Tian, M. Wang, J. Li and X. Wang, *RSC Adv.*, 2014, **4**, 47129.
191 C. V. Nunes Jr, M. Danczuk, A. A. Bortoti, J. M. Gonçalves, K. Araki and F. J. Anaissi, *J. Power Sources*, 2015, **297**, 408.
192 S. Sasikala, G. Rambabu, A. Shukla, N. Nagaraju and S. D. Bhat, *J. Electrochem. Soc.*, 2018, **165**, F1358.
193 M. Ranjani, A. G. Al-Sehemi, M. Pannipara, M. A. Aziz, S.-M. Phang, F.-L. Ng and G. G. Kumar, *Solid State Ionics*, 2020, **353**, 115318.
194 N. S. A. Hamid, S. K. Kamarudin and N. A. Karim, *Int. J. Energy Res.*, 2021, **45**, 2245.
195 P. Y. You, S. K. Kamarudin and M. S. Masdar, *Int. J. Hydrogen Energy*, 2019, **44**, 1857.
196 Q. Tang, Z. Tang, J. Wu, J. Lin and M. Huang, *RSC Adv.*, 2011, **1**, 1453.
197 Q. Tang, J. Wu, Z. Tang, Y. Li, J. Lin and M. Huang, *J. Mater. Chem.*, 2011, **21**, 13354.
198 Q. Tang, Z. Mao, S. Ma and K. Huang, *RSC Adv.*, 2012, **2**, 11465.
199 K. Peng, N. Bhuvanendran, S. Ravichandran, Z. Xu, W. Zhang, Q. Ma, Q. Xu, L. Khotseng and H. Su, *Int. J. Hydrogen Energy*, 2020, **45**, 9795.
200 N. A. I. M. Ishak, S. K. Kamarudin, S. N. Timmiati, N. A. Karim and S. Basri, *J. Adv. Res.*, 2021, **28**, 63.
201 N. A. I. Md Ishak, S. K. Kamarudin, S. N. Timmiati, N. Karim and S. Basri, *Int. J. Energy Res.*, 2021, **45**, 7380.
202 B. Libby, W. H. Smyrl and E. Cussler, *AIChE J.*, 2003, **49**, 991.
203 J.-M. Thomassin, C. Pagnoulle, G. Caldarella, A. Germain and R. Jérôme, *J. Membr. Sci.*, 2006, **270**, 50.
204 Y.-F. Lin, C.-Y. Yen, C.-C. M. Ma, S.-H. Liao, C.-H. Hung and Y.-H. Hsiao, *J. Power Sources*, 2007, **165**, 692.
205 Y.-F. Lin, C.-Y. Yen, C.-H. Hung, Y.-H. Hsiao and C.-C. M. Ma, *J. Power Sources*, 2007, **168**, 162.
206 R. Gosalawit, S. Chirachanchai, S. Shishatskiy and S. P. Nunes, *Solid State Ionics*, 2007, **178**, 1627.
207 R. Gosalawit, S. Chirachanchai, S. Shishatskiy and S. P. Nunes, *J. Membr. Sci.*, 2008, **323**, 337.
208 C.-C. Yang, Y.-J. Lee and J. M. Yang, *J. Power Sources*, 2009, **188**, 30.
209 M. M. Hasani-Sadrabadi, E. Dashtimoghadam, F. S. Majedi, K. Kabiri, M. Solati-Hashjin and H. Moaddel, *J. Membr. Sci.*, 2010, **365**, 286.
210 J. Auimviriyavat, S. Changkhamchom and A. Sirivat, *Ind. Eng. Chem. Res.*, 2011, **50**, 12527.
211 I. Nicotera, K. Angjeli, L. Coppola, A. S. Aricò and V. Baglio, *Membranes*, 2012, **2**, 325.
212 M. F. Samberan, M. M. Hasani-Sadrabadi, S. R. Ghaffarian and A. Alimadadi, *Int. J. Hydrogen Energy*, 2013, **38**, 14076.
213 M. Purwanto, L. Atmaja, M. A. Mohamed, M. T. Salleh, J. Jaafar, A. F. Ismail, M. Santoso and N. Widiastuti, *RSC Adv.*, 2016, **6**, 2314.
214 Y. A. Sihombing, Susilawat, S. U. Rahayu and M. D. Situmeang, *Mater. Sci. Energy Technol.*, 2023, **6**, 252.
215 R. Wang, T. Zhou, X. Qiu, H. Wang, Q. Wang, H. Feng, V. Linkov and S. Ji, *Int. J. Hydrogen Energy*, 2013, **38**, 10381.
216 T. Zhou, H. Wang, S. Ji, V. Linkov and R. Wang, *J. Power Sources*, 2014, **248**, 427.
217 L. Wang, L. Zhao, P. Yu, C. Tian, F. Sun, H. Feng, W. Zhou, J. Wang and H. Fu, *J. Mater. Chem. A*, 2015, **3**, 24139.
218 D.-H. Jeon, T.-J. Lim and S.-J. Park, *J. Ind. Eng. Chem.*, 2015, **31**, 244.
219 G. Sun, L. Zhou, J. Li, J. Tang and Y. Wang, *RSC Adv.*, 2015, **5**, 71980.
220 R. Wang, K. Wang, Z. Wang, H. Song, H. Wang and S. Ji, *J. Power Sources*, 2015, **297**, 295.
221 A. P. Periasamy, R. Ravindranath, P. Roy, W.-P. Wu, H.-T. Chang, P. Veerakumar and S.-B. Liu, *J. Mater. Chem. A*, 2016, **4**, 12987.
222 P. Roy, R. Ravindranath, A. P. Periasamy, C.-W. Lien, C.-T. Liang and H.-T. Chang, *RSC Adv.*, 2016, **6**, 108941.
223 F. Liu, L. Liu, X. Li, J. Zeng, L. Du and S. Liao, *RSC Adv.*, 2016, **6**, 27535.
224 Z. Guo, Z. Xiao, G. Ren, G. Xiao, Y. Zhu, L. Dai and L. Jiang, *Nano Res.*, 2016, **9**, 1244.
225 P. Balakrishnan, I. I. G. Inal, E. Cooksey, A. Banford, Z. Aktas and S. M. Holmes, *Electrochim. Acta*, 2017, **251**, 51.
226 H. Wang, F.-X. Yin, B.-H. Chen, X.-B. He, P.-L. Lv, C.-Y. Ye and D.-J. Liu, *Appl. Catal. B*, 2017, **205**, 55.
227 D. Kong, W. Yuan, C. Li, J. Song, A. Xie and Y. Shen, *Appl. Surf. Sci.*, 2017, **393**, 144.
228 D. Saranya and V. Selvaraj, *Int. J. Hydrogen Energy*, 2018, **43**, 13450.

229 B. Ruiz-Camacho, A. Medina-Ramírez, M. V. Aguilera and J. I. Minchaca-Mojica, *Int. J. Hydrogen Energy*, 2019, **44**, 12365.
230 G. G. Kumar, *J. Mater. Chem.*, 2011, **21**, 17382.
231 X.-W. Wu, N. Wu, C.-Q. Shi, Z.-Y. Zheng, H.-B. Qi and Y.-F. Wang, *Appl. Surf. Sci.*, 2016, **388**, 239.
232 X. Fuku, M. Modibedi, N. Matinise, P. Mokoena, N. Xaba and M. Mathe, *J. Colloid Interface Sci.*, 2019, **545**, 138.
233 M. Ma, S. You, J. Qu and N. Ren, *RSC Adv.*, 2016, **6**, 66147.
234 J. Chouler, I. Bentley, F. Vaz, A. O'Fee, P. J. Cameron and M. Di Lorenzo, *Electrochim. Acta*, 2017, **231**, 319.
235 S. Chen, G. He, X. Hu, M. Xie, S. Wang, D. Zeng, H. Hou and U. Schröder, *ChemSusChem*, 2012, **5**, 1059.
236 S. Chen, Q. Liu, G. He, Y. Zhou, M. Hanif, X. Peng, S. Wang and H. Hou, *J. Mater. Chem.*, 2012, **22**, 18609.
237 Y. Yuan, T. Liu, P. Fu, J. Tang and S. Zhou, *J. Mater. Chem. A*, 2015, **3**, 8475.
238 L. Liu, Q. Xiong, C. Li, Y. Feng and S. Chen, *RSC Adv.*, 2015, **5**, 89771.
239 R. Karthikeyan, B. Wang, J. Xuan, J. W. C. Wong, P. K. H. Lee and M. K. H. Leung, *Electrochim. Acta*, 2015, **157**, 314.
240 M. Ma, S. You, W. Wang, G. Liu, D. Qi, X. Chen, J. Qu and N. Ren, *ACS Appl. Mater. Interfaces*, 2016, **8**, 32307.
241 S. Chen, J. Tang, X. Jing, Y. Liu, Y. Yuan and S. Zhou, *Electrochim. Acta*, 2016, **212**, 883.
242 M. Harshiny, N. Samsudeen, R. J. Kameswara and M. Matheswaran, *Int. J. Hydrogen Energy*, 2017, **42**, 26488.
243 M. Li, H. Zhang, T. Xiao, S. Wang, B. Zhang, D. Chen, M. Su and J. Tang, *Electrochim. Acta*, 2018, **283**, 780.
244 F.-Y. Zheng, R. Li, S. Ge, W.-R. Xu and Y. Zhang, *J. Power Sources*, 2020, **446**, 227356.
245 Z. Zha, Z. Zhang, P. Xiang, H. Zhu, B. Zhou, Z. Sun and S. Zhou, *RSC Adv.*, 2021, **11**, 1077.
246 A. A. Yaqoob, M. N. M. Ibrahim, A. S. Yaakop, K. Umar and A. Ahmad, *Chem. Eng. J.*, 2021, **417**, 128052.
247 Z. Zha, Z. Zhang, P. Xiang, H. Zhu, X. Shi and S. Chen, *Sci. Total Environ.*, 2021, **764**, 142918.
248 S. K. Dhillon and P. P. Kundu, *ACS Appl. Mater. Interfaces*, 2022, **14**, 47633.
249 V. Jaswal and Y. K. Nandabalan, *J. Environ. Manage.*, 2023, **328**, 116912.
250 B. Yu, Y. Li and L. Feng, *J. Hazard. Mater.*, 2019, **377**, 70.
251 V. Yousefi, D. Mohebbi-Kalhori and A. Samimi, *Electrochim. Acta*, 2018, **283**, 234.
252 V. Yousefi, D. Mohebbi-Kalhori and A. Samimi, *Int. J. Hydrogen Energy*, 2020, **45**, 4804.
253 B. Neethu, G. D. Bhowmick and M. M. Ghangrekar, *Biochem. Eng. J.*, 2019, **148**, 170.
254 A. Angelov, S. Bratkova and A. Loukanov, *Energy Convers. Manage.*, 2013, **67**, 283.
255 A. N. Ghadge and M. M. Ghangrekar, *Electrochim. Acta*, 2015, **166**, 320.
256 J. Tang, Y. Yuan, T. Liu and S. Zhou, *J. Power Sources*, 2015, **274**, 170.
257 L. Deng, H. Yuan, X. Cai, Y. Ruan, S. Zhou, Y. Chen and Y. Yuan, *Int. J. Hydrogen Energy*, 2016, **41**, 22328.
258 C. S. Ayyappan, V. M. Bhalambaal and S. Kumar, *Bioresour. Technol.*, 2018, **251**, 165.
259 G. E. Oyiwona, J. C. Ogbonna, C. U. Anyanwu and S. Okabe, *Bioresour. Bioprocess.*, 2018, **5**, 1.
260 B. Neethu, G. D. Bhowmick and M. M. Ghangrekar, *Biochem. Eng. J.*, 2018, **133**, 205.
261 Y. Jia, H. Feng, D. Shen, Y. Zhou, T. Chen, M. Wang, W. Chen, Z. Ge, L. Huang and S. Zheng, *J. Hazard. Mater.*, 2018, **354**, 27.
262 Q. Chen, W. Pu, H. Hou, J. Hu, B. Liu, J. Li, K. Cheng, L. Huang, X. Yuan, C. Yang and J. Yang, *Bioresour. Technol.*, 2018, **249**, 567.
263 H. Feng, Y. Jia, D. Shen, Y. Zhou, T. Chen, W. Chen, Z. Ge, S. Zheng and M. Wang, *Sci. Total Environ.*, 2018, **635**, 45.
264 Y. Ma, S. You, B. Jing, Z. Xing, H. Chen, Y. Dai, C. Zhang, N. Ren and J. Zou, *Int. J. Hydrogen Energy*, 2019, **44**, 16624.
265 C. Arenas, A. Sotres, R. M. Alonso, J. González-Arias, A. Morán and X. Gómez, *Biomass Conv. Bioref.*, 2020, **12**, 313.
266 T. P. Sciarria, M. A. C. de Oliveira, B. Mecheri, A. D'Epifanio, J. L. Goldfarb and F. Adani, *J. Power Sources*, 2020, **462**, 228183.
267 A. Raychaudhuri and M. Behera, *Electrochim. Acta*, 2020, **363**, 137261.
268 J. Dong, Y. Wu, C. Wang, H. Lu and Y. Li, *Bioprocess Biosyst. Eng.*, 2020, **43**, 2165.
269 Y. Wang, C. He, W. Li, W. Zong, Z. Li, L. Yuan, G. Wang and Y. Mu, *Chem. Eng. J.*, 2020, **399**, 125848.
270 M. Li, Y.-W. Li, X.-L. Yu, J.-J. Guo, L. Xiang, B.-L. Liu, H.-M. Zhao, M.-Y. Xu, N.-X. Feng, P.-F. Yu, Q. Y. Cai and C. H. Mo, *Sci. Total Environ.*, 2020, **726**, 138573.
271 K. Senthilkumar and M. Naveenkumar, *Biomass Conv. Bioref.*, 2021, 1, DOI: **10.1007/s13399-021-01505-x**.
272 M. Li, J. Zhou, Y.-G. Bi, S.-Q. Zhou and C.-H. Mo, *Sep. Purif. Technol.*, 2021, **256**, 117805.
273 A. A. Yaqoob, A. Serrà, M. N. M. Ibrahim and A. S. Yaakop, *Arabian J. Chem.*, 2021, **14**, 103121.
274 P. J. Sarma and K. Mohanty, *Bioelectrochemistry*, 2022, **144**, 107996.
275 P. J. Sarma and K. Mohanty, *Mater. Chem. Phys.*, 2023, **296**, 127337.
276 M. R. Molavian, A. Abdolmaleki, H. Gharibi, K. Firouz Tadavani and M. Zhiani, *Energy Fuels*, 2017, **31**, 2017.
277 Y. Wang, M. Zhu, G. Wang, B. Dai, F. Yu, Z. Tian and X. Guo, *Nanomaterials*, 2017, **7**, 404.
278 M. Borghei, N. Laocharoen, E. Kibena-Põldsepp, L.-S. Johansson, J. Campbell, E. Kauppinen, K. Tammeveski and O. J. Rojas, *Appl. Catal. B*, 2017, **204**, 394.
279 S. Gao, X. Li, L. Li and X. Wei, *Nano Energy*, 2017, **33**, 334.
280 G. Sharma and K. Singh, *Ceram. Int.*, 2019, **45**, 20501.
281 D. Dong, Y. Wu, X. Zhang, J. Yao, Y. Huang, D. Li, C.-Z. Li and H. Wang, *J. Mater. Chem.*, 2011, **21**, 1028.
282 D. Dong, J. Yao, Y. Wu, X. Zhang, G. Xu, C.-Z. Li and H. Wang, *Electrochem. Commun.*, 2011, **13**, 1038.
283 X. Zhu, L. Zhai, L. Zhang, J. Zhang, X. Liu and J. Song, *Appl. Clay Sci.*, 2018, **166**, 200.

284 L. A. Malik, N. A. Mahmud, N. S. M. Affandi, N. W. Mazlan, N. H. A. Zakaria, N. I. Abd Malek, O. H. Hassan, A. M. M. Jani and N. Osman, *Int. J. Hydrogen Energy*, 2021, **46**, 5963.
285 V. Neburchilov, H. Wang, J. J. Martin and W. Qu, *J. Power Sources*, 2010, **195**, 1271.
286 W.-K. Chao, C.-M. Lee, S.-Y. Shieu, C.-C. Chou and F.-S. Shieu, *J. Power Sources*, 2008, **177**, 637.
287 X. Yu and P. G. Pickup, *J. Power Sources*, 2008, **182**, 124.
288 L. Q. Wang, M. Bellini, J. Filippi, M. Folliero, A. Lavacchi, M. Innocenti, A. Marchionni, H. A. Miller and F. Vizza, *Appl. Energy*, 2016, **175**, 479.
289 Q. Tian, W. Chen, L. Zhang, F. Zhang and Y. Wu, *Ionics*, 2015, **21**, 1693.
290 T. B. Ferriday and P. H. Middleton, *Int. J. Hydrogen Energy*, 2021, **46**, 18489.
291 R. Gokhale, S. M. Unni, D. Puthusseri, S. Kurungot and S. Ogale, *Phys. Chem. Chem. Phys.*, 2014, **16**, 4251.
292 X. Liao, L. Ren, D. Chen, X. Liu and H. Zhang, *J. Power Sources*, 2015, **286**, 258.
293 Y. Lu, L. Wang, K. Preuß, M. Qiao, M.-M. Titirici, J. Varcoe and Q. Cai, *J. Power Sources*, 2017, **372**, 82.
294 A. C. Rady, S. Giddey, S. P. S. Badwal, B. P. Ladewig and S. Bhattacharya, *Energy Fuels*, 2012, **26**, 1471.
295 S. Moradmand, J. A. Allen and S. W. Donne, *Fuel*, 2021, **291**, 120215.